Declaration

I know that plagiarism is wrong. Plagiarism is to use another's work and pretend that it is one's own. I have used the convention for the citation and referencing. Each significant contribution to, and quotation in, this report from works of other people has been attributed, and has been cited and referenced.

This report is my own work. I have not allowed, and will not allow anyone to copy my work with the intention of passing it off as his or her own work.

Signature ……

Ian Rossiter
Date: May 2008

Abstract

This thesis presents the results of an investigation into the effects of several geometric parameters on the performance of perforated plates as a blast wave mitigation technique. Results of experimental and numerical simulations are reported.

The main objective of this investigation was to determine the effects of the perforated plate hole size on the blast wave mitigation capability of the plate.

The blast wave was created by detonating plastic explosives. The blast wave travelled unhindered down the length of a cylindrical tube where it came into contact with the perforated plate. The performance of each perforated plate was judged by analysing the response of a mild steel target plate situated 25mm behind the perforated plate. One series of tests was performed without the presence of a perforated plate allowing the blast wave to interact unhindered with the target plate. This gave a point of reference with which to compare the response of the target plates with perforated plates in front of the target plate. The perforated plate hole sizes ranged from 21mm to 92mm.

Large plastic deformation typical of Mode I failure was observed in most cases for both the target plates and perforated plates. The target plate profile resembled a uniform global dome, whilst the perforated plates deformed about a plastic hinge at the boundary. The results of the experiments showed that decreasing the perforated plate hole size decreased the target plate mid-point deflection.

A numerical analysis was carried out using ANSYS AUTODYN to model the dynamic loading and response of both the perforated plate and target plate. The impulse imparted to the pendulum, target plate and perforated plate deflections and final deformation profiles were compared to the experimental results. The computational predictions showed good correlation with the measured experimental results. The simulations also gave further insight into the interaction between the blast wave and the plates, indicating an increase in the impulse distribution to the boundary of the target plate with a decrease

in hole size. Only the smallest hole size (namely 21mm) reduced the mid-point deflection of the target plates without reducing the impulse threshold. The AUTODYN estimates of the impulse imparted to the pendulum, target plate mid-point deflection and perforated plate average deflection compare well with the experimental work.

Table of Contents

List of Tables

List of Figures

Notation

A_o	Area over which the impulse is imparted
BR	Blockage ratio of the perforated plate
C	Stress wave velocity
C_{ES}	Elastic stress wave velocity
C_{PS}	Plastic stress wave velocity
C_p	Specific heat of air at constant pressure
C_v	Specific heat of air at constant volume
D	Material parameter ($844s^{-1}$)
E	Young's modulus
E_p	Slope of the tangent line to the graph of stress versus strain in the plastic region at the relative strain value
E_o	Specific internal energy of air
I	Impulse imparted to the test plates
I_o	Specific impulse
I_t	Impulse at which the target plate tears
K	Bulk modulus
L	Filter length
L_a	Perforated plate arm length
N	Number of perforations
P	Pressure
P_o	Atmospheric pressure
P_e	Pressure of original inert explosive
P_p	Pressure of explosive products
PP	Perforated plate
R	Radius of circular plate
R_i	Radius of the central perforation
R_g	Gas constant
R_o	Radius of loaded area
R_w	Percentage of the incident stress wave that is reflected

S, SOD	Stand-off distance
TP	Target plate
T	Temperature
T_e	Temperature of original inert explosive
T_p	Temperature of explosive products
T_w	Percentage of the incident stress wave that is transmitted
V	Volume
V_D	Detonation velocity
V_S	Streaming velocity of explosive products
Z	Impedance
d_o	Perforated plate hole diameter
d_{fp}	Filter particle diameter
h_{ME}	Height at which maximum effective mass of explosive occurs
q	Material parameter (2.207)
t	Plate thickness
m	Charge mass
Δ	Filter air gap length
σ_d	Dynamic yield stress
σ_o	Static yield stress
ρ	Material density
ρ_e	Density of original inert explosive
ρ_p	Density of explosive products
ρ_{fp}	Filter particle density
γ	Ratio of specific heats
δ	Vertical plate deflection
δ_o	Maximum plate deflection
δ_P	Average deflection of the perforated plate
δ_T	Mid-point deflection of the target plate

Acknowledgments

The author would like to thank Dr GS Langdon and Prof GN Nurick for supervising this investigation along with many hours sacrificed for both experimental testing and discussion.

Many thanks to Dr S Chung Kim Yuen for his help with the experimental testing, along with Mr TJ Cloete, Dr MD Theobald, Dr D Bonorchis and Mr RA Govender for their time given to the discussion and analysis of the results. Final thanks to Mr VH Balden for his extensive help with the numerical modelling.

1. Introduction

Dynamic and impulsive loading, such as that created by an explosion or sudden impact, and the subsequent damage imposed by such events, is of great concern. According to the Washington Post [1], the number of terrorist attacks worldwide increased nearly fourfold in 2005 to 11,111 resulting in over 14,600 civilian deaths. These figures only serve to highlight the importance of ongoing research into blast and impact mitigation techniques.

The formation of a blast wave, which follows the detonation of an explosive, often as a result of a terrorist attack or landmine incident, is one of the main damage mechanisms of an explosion. Various techniques have been developed as a means of protecting against the destructive effect of blast waves. These techniques include mitigation devices designed to absorb, disrupt and ultimately reduce the effect of the blast wave before it reaches its intended target. Such techniques are broadly classified as either active or passive systems. Passive systems are embedded within the structural design. Unlike active systems they do not require a trigger mechanism.

The main focus of research has been on the development of passive systems. The main reason for this is that impulsive loading events occur in a matter of microseconds and active systems would need to detect a blast within this time frame. No information was found in the literature on active systems with the ability to detect detonation and deploy the mitigation system with the required speed.

Passive mitigation systems include:

- Impedance mismatching, designed to reflect the blast wave
- Protective sacrificial cladding, designed to transform the impulse by reducing the peak pressure of the blast wave and extending the load duration.
- Geometrical arrangements, such as the v-shaped hulls, designed to deflect the blast wave. This design feature is common to armoured personnel carriers such as the Buffel.
- Granular filters and perforated plates, designed to disrupt the blast wave.

This thesis reports on the results of an experimental and numerical investigation into the effects of several geometric parameters on the performance of perforated plates as a blast wave mitigation technique. The investigation into the response of thin plates subjected to blast loading conditions has been widely documented over the years as reported on by Nurick and Martin [2, 3] and Zhu and Lu [4], and is well understood. It is for this reason that thin mild steel target plates were used to judge the performance of the perforated plates at mitigating the destructive effect of blast waves.

The principle objectives of this report are to:

- Investigate the effects of the perforated plate hole-size and thickness on the mitigation capabilities of the perforated plate.
- Perform a numerical analysis to model the dynamic loading and response of both the perforated plate and target plate.
- Compare the numerical and experimental results.
- Draw conclusions and recommendations based on the findings.

The report begins by presenting and discussing the results of a literature review which documents past theoretical and experimental work by various authors. The experimental procedure and test arrangement are briefly described in Chapter 3, followed by initial observations and experimental results in Chapter 4. A detailed analysis of the results is presented in Chapter 5. Chapter 6 provides details of the numerical model, focusing on the various material models used as well as a detailed mesh refinement. The final working model is presented with a justification of the modelling decisions. The results of the numerical simulations are presented and compared to the experimental results in Chapter 7. A discussion is presented in Chapter 8, in which the simulations are used to give further insight into the interaction between the blast wave and the perforated plates. Conclusions are drawn and recommendations are made in Chapters 9 and 10 based on the findings.

2. Literature Review

2.1 Explosions

An explosion is defined by Baker [5] as a process in which a pressure wave of finite amplitude is generated by a rapid release of energy. Kinney [6] explains that the source of the energy is of less importance, but that the release must be sudden, occurring so rapidly that a local accumulation of energy occurs at the site of the explosion. This energy is then dissipated in various ways such as an explosive blast wave. The magnitude of the explosion is defined by the amount of energy released by the explosive and may be expressed in energy units i.e. joules (J). For example, TNT generates blast energy of about 4690 J/gram [6].

2.2 Explosives

An explosive is any substance that undergoes a rapid chemical reaction during which large quantities of gaseous products and heat evolve. Explosive substances can be gaseous, liquid or solid. Explosives are further divided into two principle types, namely low explosives and high explosives according to the nature of their reaction with regards to burn velocity. Low explosives burn relatively slowly; with burn velocities of the order of a few mm/s and hence the evolved gases disperse without building up large pressures. Low explosives are commonly used as propellants in guns and rockets.

High explosives have burn velocities in the region of 1500 to 7500m/s. High explosives may be further divided into initiating and secondary explosives. Initiating explosives are highly sensitive and easily detonated by heat, an example of which is lead azide (PbN_6), a white powder, which releases approximately 1600J/gram when it decomposes. Initiating explosives are generally used to initiate detonation of large quantities of less sensitive secondary explosives [7].

Secondary explosives have higher energy content in comparison to initiating explosives and are more stable, making detonation achievable only through a sudden or intense shock. Examples of secondary explosives are PE4 and TNT.

2.3 Detonation

Detonation, as explained by Rinehart and Pearson [7], is the process in which an explosive decomposes, resulting in the evolution of gaseous products and heat. This decomposition proceeds through the explosive at a rate of several thousand metres per second, leaving behind gases at high temperature and pressure.

Ideal detonation can be viewed as a discontinuity moving through the explosive at a constant detonation velocity (V_D). The detonation wave proceeds outward from the point of detonation, as idealised in Figure 1, in a stable manner progressing through the explosive at a constant rate making the detonation front spherical.

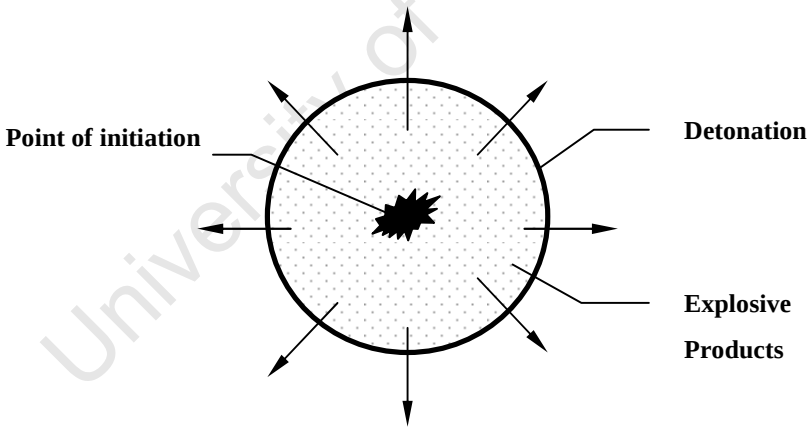

Figure 1: Detonation front arising from a point explosion [7]

The concept of a detonation front in idealised detonation, is shown schematically in Figure 2. To the right of a detonation front is the original inert explosive defined by density (ρ_e), Pressure (P_e) and temperature (T_e). On the left of the detonation front the explosive has completely reacted, filling the volume with gases at high temperature (T_p) and pressure (P_p). The gasses are compressed to a higher density (ρ_p) and imparted to a streaming velocity (V_S), moving to the right [7].

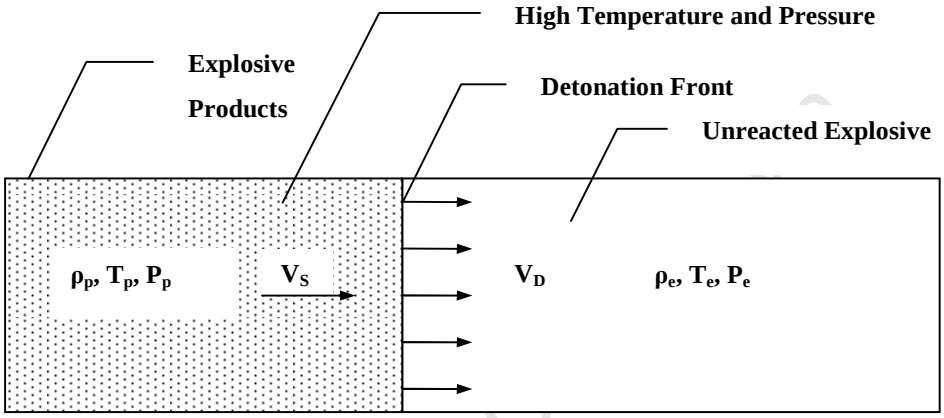

Figure 2: Ideal detonation, showing the position of the detonation front [7]

2.4 Blast Waves

Following the detonation of an explosive, a blast wave develops. Cooper and Kurowski [8] define this blast wave as a high-pressure wave or disturbance, moving through a material at a speed faster than the speed of sound in that material. The blast wave contains most of the energy released by the explosion and is transmitted through the surrounding fluid at a velocity greatly in excess of the gaseous products [7].

The blast wave is a result of the violent expansion of the gaseous products forcing the surrounding air out of the volume it occupies. A layer of compressed air is formed in front of these gases and is known as the blast wave. This violent motion is able to stress a material beyond its elastic limit, so that the material will not return to its original state when the pressure disturbance is relieved [8].

2.5 Measuring Blast Loads

A smoothed pressure-time history for a typical far-field blast wave is shown in Figure 3. After detonation the pressure rises sharply to a maximum pressure $P_s + P_o$ then decays to ambient pressure P_o before dropping to a partial vacuum. The maximum positive pressure is termed the peak overpressure whilst the maximum vacuum pressure is termed the peak underpressure. The peak overpressure is much larger than the peak underpressure as can be seen from Figure 3, and thus the negative phase is often neglected [5].

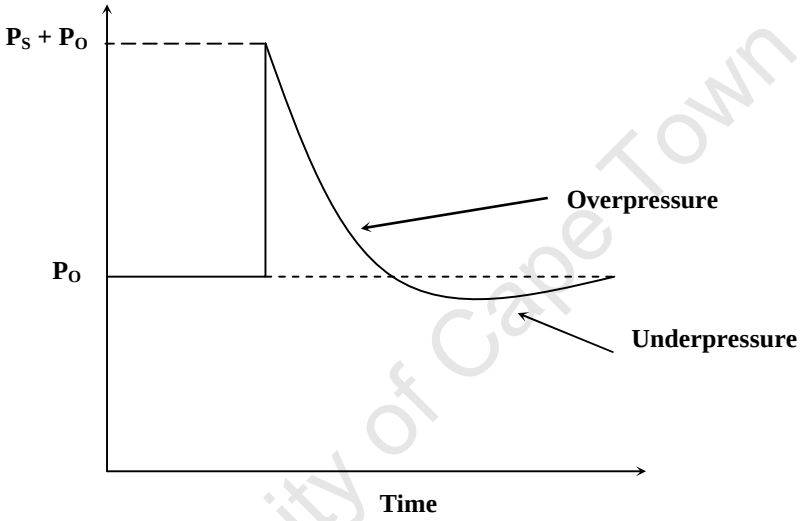

Figure 3: Smoothed pressure-time history for a far-field blast wave [5]

The blast load may be quantified as an impulse represented by the area under the pressure-time curve and is given by the following equation:

$$I = A_o \times \int P(t)dt \tag{2.1}$$

Where A_o is the area over which the impulse is imparted. The impulse is dependent on the peak overpressure, the duration of the pulse and the rate of decay from peak pressure to ambient pressure, commonly known as the transient pressure-time history. Depending on the duration of the pulse, the loading can be classified as impulsive, dynamic or quasi-static.

According to The Steel Construction Institute [9], a blast load is classified as ‘impulsive’(damage caused is dependant on the impulse) if the duration of the load is less than the natural period of the structure, and thus higher loads can be tolerated as the structure has insufficient time to fully respond to the load. If the load duration is much longer than the natural period of the structure, the damage caused is determined by the peak value of the load. This type of loading is classified as ‘quasi-static’. Loading in the transition region is classified as ‘dynamic’, with the damage of the structure dependant on both the peak pressure and impulse.

2.6 Loading Conditions

Blast loads can be generated in a variety of ways such as chemical or mechanical explosions. For example, the bursting of a sealed or partially sealed container with high internal pressure is often referred to as a mechanical explosion. More commonly, blast loads are the result of the detonation of plastic explosives, as described in sections 2.1 to 2.4, and are classified as chemical explosions. The focus of this study is on the mitigation of blast waves generated by the detonation of plastic explosives, and thus all other methods will not be covered in detail. Plastic explosives can be laid out in various ways in relation to the test plate geometry (namely a central circular disk, a uniform spread or concentric annuli), and thus different loading conditions are achievable.

2.6.1 Localised Impulse Loading using Plastic Explosive

The plastic explosive is shaped into a circular disc and placed onto a polystyrene pad. A detonator is attached using a one gram leader of explosive. The pad is placed in direct contact with the test plate, as shown in Figure 4. The explosive is then detonated resulting in localized loading of the test plate i.e. the blast wave is assumed to be acting over a small central region rather than over the entire exposed area of the plate. This method was used by Nurick et al [10, 11].

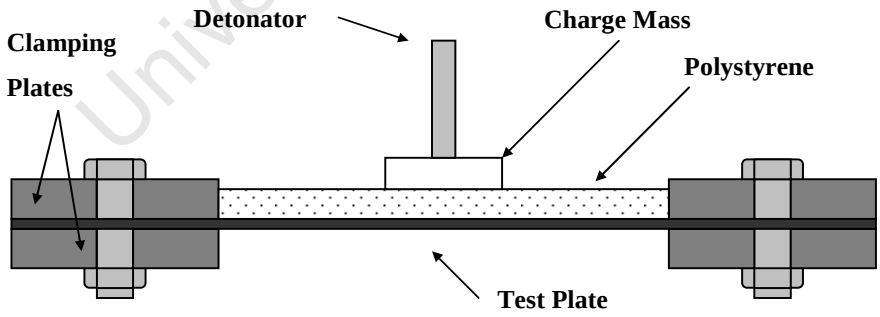

Figure 4: Localized loading

2.6.2 Uniform Impulsive Loading using Plastic Explosive

(i) Concentric Annuli

The plastic explosive is laid out in concentric annuli corresponding to the shape of the test plate, and connected by two cross-leaders of explosive. An example of the layout for a square plate is shown in Figure 5. The annuli are arranged such that there is on average a uniform distribution of explosive over the exposed area of the plate. The reason for using concentric annuli as opposed to a uniform spread of explosive over the entire plate area is the failure to detonate if the explosive charge thickness is less than 2.0 mm, as reported by Nurick and Martin [12]. This limiting factor imposes a restriction on the charge mass that can be used. This method was used by Nurick et al [3, 13, 14].

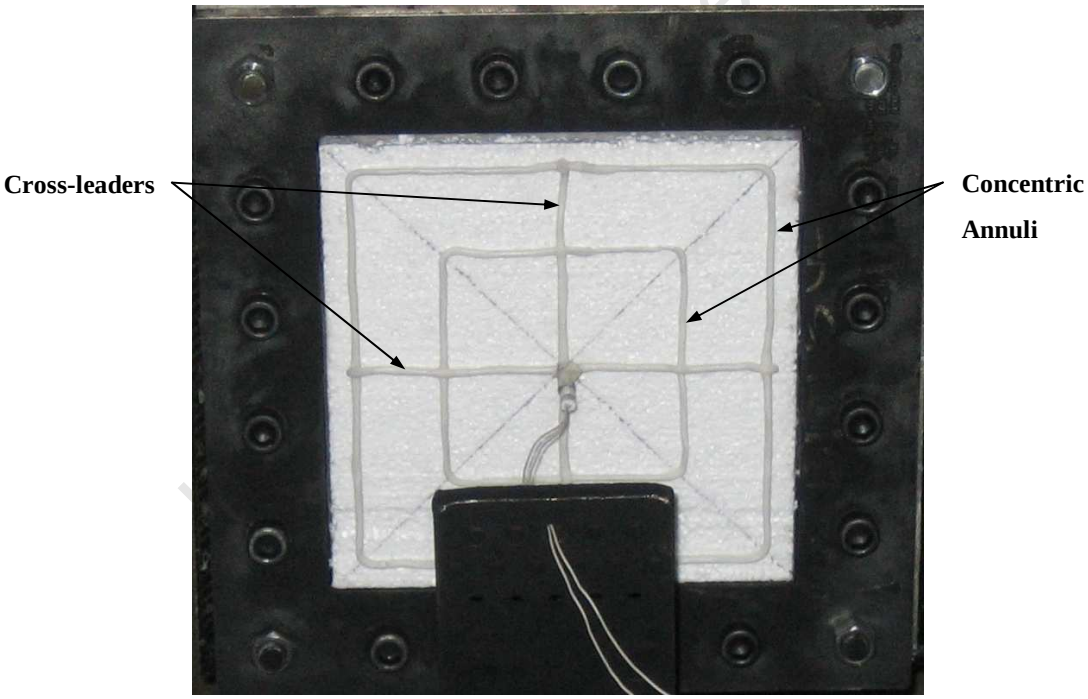

Figure 5: Photograph of the uniform loading layout for a square test plate using concentric annuli [15]

(ii) Stand-off Distance

The plastic explosive is shaped into a circular disc and placed on top of a polystyrene pad. A detonator is attached using a one gram leader of explosive. Instead of the polystyrene being in direct contact with the material, as in the localised loading case, it is placed into the open end of a cylinder, as shown in Figure 6. This creates an air gap between the explosive and the test plate, known as the stand-off distance (S). Recent work by Jacob *et al* [16] investigated the effect of the stand-off distance on the deformation and loading condition of mild steel plates subjected to confined blast loads.

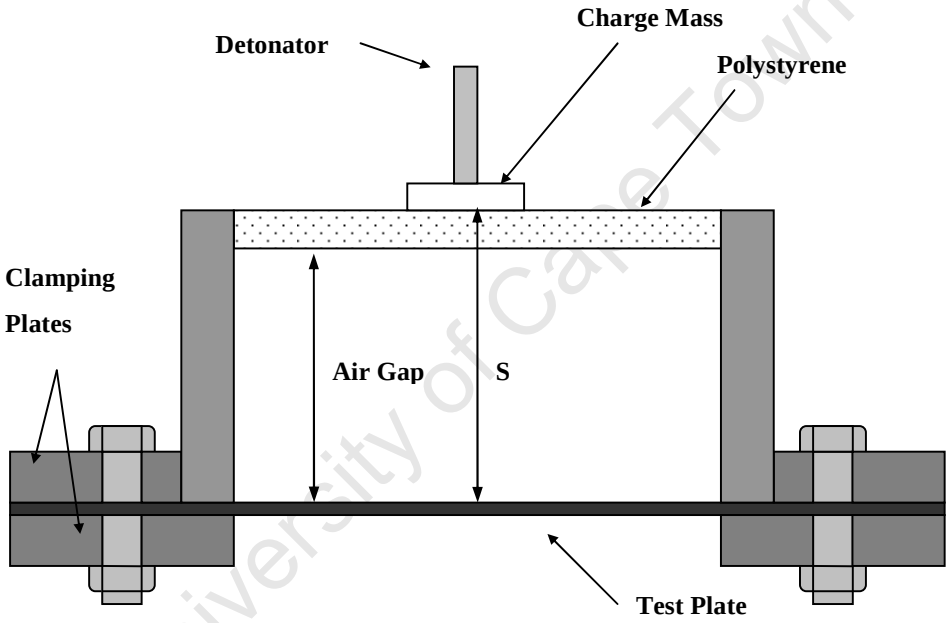

Figure 6: Uniform loading using a stand-off distance

For stand-off distances ranging from 100mm – 300mm a large global dome was observed. This form of deformation has been reported by Nurick *et al* [13, 17] for uniformly loaded plates, loaded by detonating concentric rings of explosive. For stand-off distances ranging from 13mm – 40mm the plate profiles revealed an inner dome, atop a larger global dome. Similar observations were reported by Nurick *et al* [10, 11] for circular and quadrangular plates subjected to localized blast loads. For stand-off distances ranging from 50mm – 75mm the plate profiles exhibited a transition phase between localized and uniform loading.

2.7 Structural Response

The investigation of mild steel plates, subjected to uniform and localised impulsive blast loads, has been widely documented as reported by Nurick and Martin [2, 3]. Dimensionless impulse numbers have been developed according to the various plate geometries (either circular or quadrangular), loading geometries and aspect ratios. An empirical formulae relating large permanent central displacement of a mild steel plate subjected to impulsive loading has been used extensively [13, 16]. The determination of these dimensionless impulse numbers and empirical formulae is covered in section 2.8.

2.7.1 Modes of Failure

Menkes and Opat [18] reported three distinctly different damage modes for fully clamped metal beams loaded impulsively, as shown in Figure 7. The failure modes were classified as:

Mode I: large inelastic deformation.
Mode II: tearing (tensile failure) in outer fibres, at or over the support.
Mode III: transverse shear failure at the support.

Teeling-Smith and Nurick [13] reported similar failure modes for fully clamped circular mild steel plates subject to uniformly distributed impulses. Some additions to Mode II failure were reported by Nurick and Shave [14] classified as:

Mode II*: Partial tearing at the boundary.
Mode IIa: Complete tearing with increasing mid-point deformation.
Mode IIb: Complete tearing with decreasing mid-point deformation.

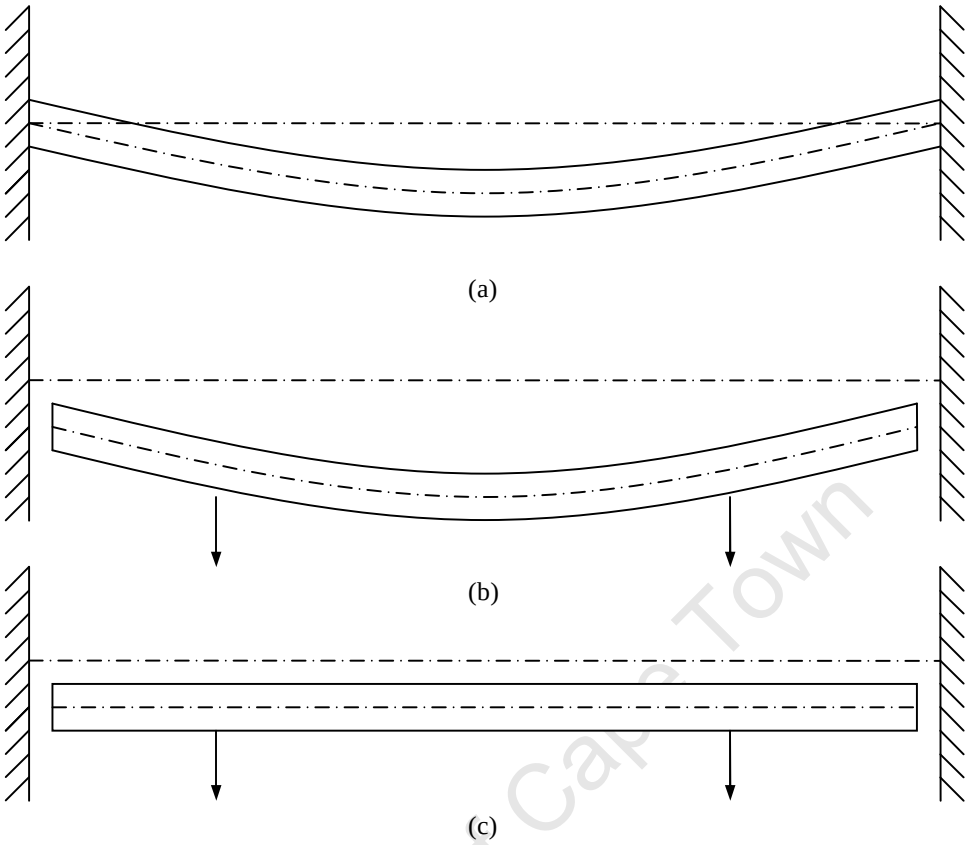

Figure 7: Failure modes for fully clamped beams loaded impulsively. (a) Mode I large inelastic deformation. (b) Mode II tensile tearing at the support. (c) Mode III transverse shear failure at the supports.

2.7.2 Thin Circular Plates Subjected to Impulsive Blast Loading

The failure of circular plates subjected to impulsive loading was investigated by Teeling-Smith and Nurick [13]. Increasing the impulse increased the mid-point deflection of the mild steel plates with the presence of thinning at the boundary. Further increase in impulse resulted in partial tearing at the boundary followed by complete tearing. They reported that the strain rate-sensitive plates exhibited mode I, mode II and mode III failure similar to those reported by Menkes and Opat [18].

2.8 Theoretical Predictions

Johnson derived the following dimensionless damage number as a guide for comparing the behaviour of metals in impact situations:

$$\alpha = \frac{\rho \upsilon^2}{\sigma_d} \tag{2.2}$$

Where (ρ) is the material density, (υ) is the impact velocity and (σ_d) is the damage stress. Alpha (α) however does not consider the method of impact, the interpretation of σ_d, the target geometry and boundary conditions or target dimensions. In order to compare results of deformed plates of similar geometries, boundary conditions and loading, Nurick and Martin [2, 3] introduced factors, which allow all other variables to be normalized into dimensionless groups. Firstly, the Johnson damage number can be written in terms of impulse as follows:

$$\alpha_o = \frac{I^2}{A_o^2 t^2 \rho \sigma_d} = \frac{I_o^2}{t^2 \rho \sigma_d} \tag{2.3}$$

Where I is the total impulse, A_o is the area of the plate over which the impulse is imparted, I_o is the specific impulse I/A_o (impulse per area) and t is the plate thickness. A geometrical damage number was then written as:

$$\psi = \left[\alpha_o \left(\frac{A_o}{A} \right)^2 \right]^{\frac{1}{2}} \tag{2.4}$$

Where A is the area of the plate.

Next the aspect ratio λ was introduced as the relationship between the distance from the plate centre to the nearest boundary and the plate thickness.

$$\lambda = \frac{R}{t}, \text{ for circular plates} \tag{2.5}$$

A loading parameter accounting for the loading area per total area was also introduced as:

$$\zeta = 1 + \ln\left(\frac{R}{R_o}\right) \tag{2.6}$$

Where (R_o) is the radius of the loaded area. This equation implies that as R_o tends toward R, ζ tends towards 1 and the plate is uniformly loaded over the full area. When R_o is very small the loading is considered to be a point-loaded situation and is more concentrated and thus results in a larger midpoint deflection.

Combining the Johnson number with these derived parameters yields a modified damage number that incorporates dimensions and loading:

$$\phi = \psi\lambda\zeta \tag{2.7}$$

For circular plates, uniform impulsive loading (ζ = 1)

$$\phi_c = \frac{I}{\pi R t^2 (\rho\sigma_o)^{\frac{1}{2}}} \tag{2.8}$$

And for circular plates, localized impulsive loading

$$\phi_c = \frac{I\left(1 + \ln\frac{R}{R_o}\right)}{\pi R t^2 (\rho\sigma_o)^{\frac{1}{2}}} \tag{2.9}$$

Nurick and Martin [2, 3] reported an empirical relationship between the mid-point deflection-thickness ratio and the damage number for circular plates as:

$$\frac{\delta}{t} = 0.425\phi_c \tag{2.10}$$

Experiments performed by Jacob [16] for circular plates also revealed a reduction in the mid-point displacement with an increase in stand-off distance, a direct result of the change in loading condition from localized through a transition phase to uniform loading. Jacob proposed a parameter called the stand-off correction factor, (ζ_s) to account for the reduction in mid-point deflection at any given stand-off distance, defined as:

$$\zeta_s = 1 + \ln\left(\frac{S}{R_o}\right) \tag{2.11}$$

Where S is the stand-off distance and R_o is the charge radius. The new loading parameter is then incorporated into dimensionless impulse (ϕ_c) for localized loading as follows:

$$\phi_c = \frac{I\left(1 + \ln\dfrac{R}{R_o}\right)}{\pi R t^2 (\rho\sigma_o)^{\frac{1}{2}}} \times \frac{1}{\zeta_s} \tag{2.12}$$

The stand-off parameter is only incorporated when the charge radius is less than the stand-off distance ($R_o < S$). The parameter thus implies that for a given charge radius increasing the stand-off distance (S) will increase the value of the correction factor (ζ_s) thus decreasing the value of the dimensionless impulse (ϕ_c) and the predicted mid-point displacement of the circular panel.

Similar dimensionless impulse equations to those of Nurick and Martin [2, 3] were derived by Cloete et al [19] for blast loaded annular plates, using an energy analysis with an assumed deformation profile. Following this investigation, a modification to the aspect ratio λ was introduced to account for the central hole in the perforated plate. The modified aspect ratio is as follows:

$$\lambda = \frac{R - R_i}{t}, \text{ for circular plates with a central hole} \tag{2.13}$$

Where R_i is the radius of the central perforation. The dimensionless impulse then becomes:

$$\phi_{cs} = \frac{I}{\pi (R - R_i) t^2 \left(\rho \sigma_o\right)^{\frac{1}{2}}} \times \frac{1 + \ln \frac{R}{R_0}}{1 + \ln \frac{S}{R_0}} \tag{2.14}$$

2.9 Blast Wave Mitigation

Several mitigation techniques have been developed, aimed at attenuating the destructive effects of blast waves. These techniques are broadly classified as either active or passive systems. Active systems respond to a detonation by activating a system to attenuate the blast. Passive systems are embedded within the structural design and unlike active systems they do not require a trigger mechanism to activate them. This investigation focuses on the use of perforated plates as a mitigating media, which is classified as a passive system. Passive systems can be further divided into four sub-categories as follows [20].

2.9.1 Impedance Mismatch

The impedance (Z) of a material is defined as the product of its density (ρ) and stress wave velocity (C) as given in equation 2.15.

$$Z = \rho \times C \tag{2.15}$$

The wave velocity for elastic stress waves in solids is defined as:

$$C_{ES} = \sqrt{\frac{E}{\rho}} \tag{2.16}$$

Where E is the Young's modulus. For plastic stress waves in solids the wave velocity is given by:

$$C_{PS} = \sqrt{\frac{E_P}{\rho}} \tag{2.17}$$

Where, E_p is defined as the slope of the tangent line to the graph of stress versus strain in the plastic region at the relative strain value.

For liquids and gases the wave velocity is defined as:

$$C = \sqrt{\frac{K}{\rho}} \tag{2.18}$$

Where K is the bulk modulus.

Impedance is important in the determination of stress wave transmission and reflection at a boundary between two materials having different impedances. This difference in impedance is known as the impedance mismatch. The greater the impedance mismatch the greater the reflection at the boundary. Kolsky [21] gives the following equations for calculating the percentage of incident stress wave that is reflected (R_w) and transmitted (T_w):

$$R_w = \frac{Z_2 - Z_1}{Z_2 + Z_1} \times 100 \tag{2.19}$$

$$T_w = \frac{2Z_1}{Z_2 + Z_1} \times 100 \tag{2.20}$$

The typical material properties used for calculating the wave velocity and impedance for air, water and steel are listed in Table 1.

Material	Density (kg/m^3)	Bulk Modulus (MN/m^2)	Elastic Modulus (GN/m^2)	Wave Speed (m/s)	Impedance (kg/m^2s)
Air	1.293	0.142	-	331	428
Water	998	2200	-	1485	1.48×10^6
Mild Steel	7800	-	207	5151	40.2×10^6

Table 1: Material properties for air, water [22] and steel [23]

Using equations 2.19 and 2.20, it can be demonstrated that an air to water interface would reflect 99.942% and transmit only 0.058% of the incident stress wave. The calculations are as follows:

$$R_w = \frac{1.48\times10^6 - 428}{1.48\times10^6 + 428}\times100 = 99.942\%$$

$$T_w = \frac{2\times428}{1.48\times10^6 + 428}\times100 = 0.058\%$$

An example of the application of impedance mismatch is the use of a water filled cavity placed between the blast wave and the main structure [20]. No appropriate literature was recovered directly related to this topic.

2.9.2 Sacrificial Cladding

Both structural damage and human response are more sensitive to high transient pressure pulses than lower pressure, long duration pulses of the same impulse magnitude. It is for this reason that sacrificial cladding is used. The outer sacrificial layer surrounds the main structure, which is also referred to as the non-sacrificial structure. In the event of a nearby explosion the sacrificial layer should transform the impulse imparted to the structure by reducing the peak pressure of the blast wave and increasing the load duration. In doing so the sacrificial cladding undergoes a significant amount of irrecoverable deformation [20]. The idealised principle of operation is shown in Figure 8.

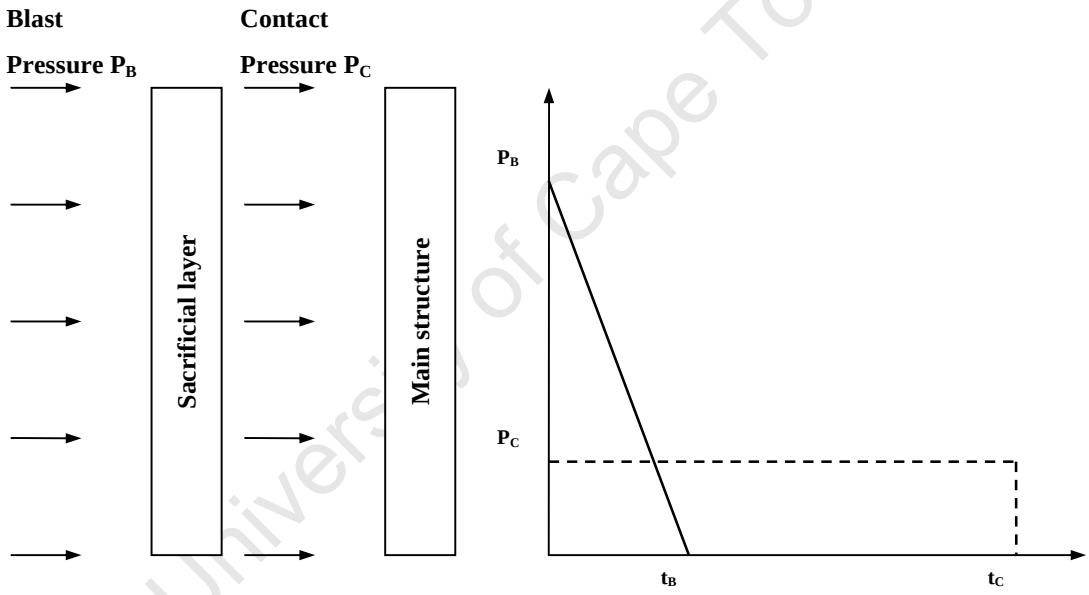

Figure 8: Mechanism of operation for sacrificial cladding [20]

The sacrificial cladding is subjected to the full load of the blast wave with a high transient pressure spike (P_B) over a load duration (t_B). As the cladding deforms the stress transmitted to the main structure is limited by the stress-strain curve of the sacrificial layer, thus transferring a lower pressure (P_C) through the contact point to the non-sacrificial structure over a longer time duration (t_C).

Several different material structures have been used as sacrificial cladding, for example flat metal plates, sandwich panels, plate corrugations and aluminium foam. Radford et al. [24] reported on the performance of clamped sandwich panels subjected to simulated blast loading. Alporas aluminium foam projectiles were used to impact clamped foam core sandwich panels over a central circular area, at velocities of 160ms^{-1} and 570ms^{-1} to simulate blast or shock loading. Monolithic stainless steel plates with the equivalent areal density were tested under the same loading conditions as a means of comparison. The results showed that, for all except the lower impulse tests, the foam sandwich panels performed better than an equivalent mass monolithic plate. Photographs of an aluminium foam sandwich panel and equivalent monolithic plate are shown in Figure 9.

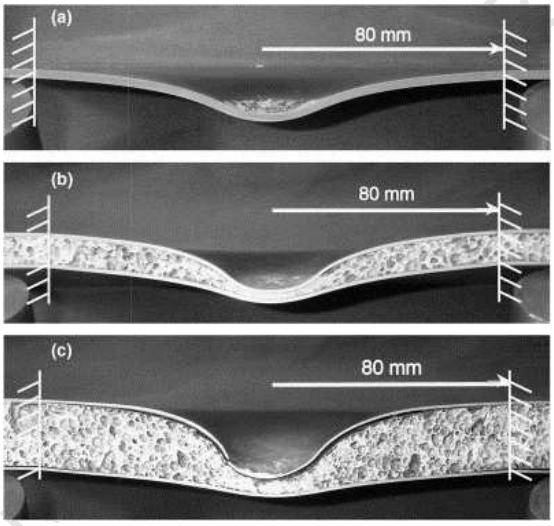

Figure 9: Photographs comparing the blast loaded monolithic steel plate with the aluminium foam sandwich panels of equivalent areal density (23.5kgm^{-2}). The plates were subjected to a specific impulse of 13kNsm^{-2} [24]

2.9.3 Deflection of Blast Waves

Armoured personnel carriers (APC's) with flat bottomed hulls, such as the Humvee shown in Figure 10, are vulnerable to the formation of large gas traps on the underside, in the event of a landmine detonation. As the superheated air from the explosion expands, it creates enough upward force to lift and even throw a six-ton armoured Humvee several feet. The instant acceleration experienced by the soldiers in the crew compartment is severe enough to compress spines and snap necks resulting in sudden death.

Figure 10: Photograph of the Humvee [25]

APC's such as the Buffel, shown in Figure 11A, have V-shaped hulls as shown in Figure 11B. The hull is designed to deflect the blast wave away from the crew cabin, as illustrated in Figure 12, thereby protecting the soldiers and reducing the resultant damage. Inverse V-shaped hulls are also used [26].

A **B**

Figure 11: Photograph of the Buffel mine resistant infantry combat vehicle (A) and V-shaped armoured passenger compartment from the underside of the Buffel (B) [27]

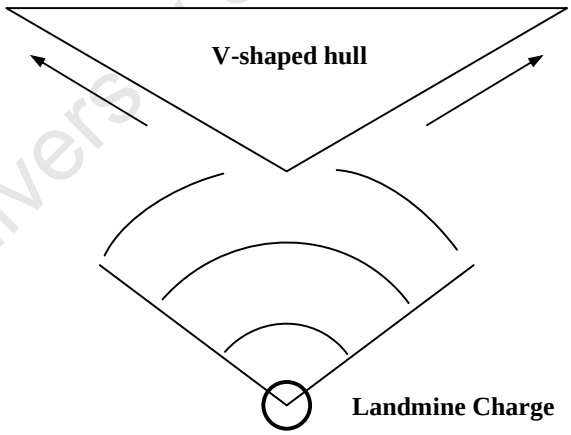

Figure 12: Diagram illustrating deflection of blast wave by V-shaped hull

2.9.4 Attenuation of Blast Waves

Several methods of blast wave attenuation have been investigated, namely through the use of granular filters and perforated plates, yet very little information is available as to their performance. Among the few available papers the most relevant results relating to the attenuation of blast waves are reported by Medvedev *et al* [28] and Britan and Ben-Dor *et al* [29].

(i)Filters

The influence of granular filters on the blast wave transmission through the ventilation system of an underground shelter was investigated by Britan and Ben-Dor *et al* [29]. The intake vent offers a way for the blast wave to enter the shelter should a high explosive weapon hit the ground in the vicinity of the shelter. Britan and Ben-Dor *et al* [29] performed several experiments in a vertical shock tube, shown in Figure 13, in order to investigate the dependence of granular filter performance on the following parameters:

- The filter length, (L)
- The length of the air gap downstream of the filter, (Δ)
- The diameter of the particles composing the filter, (d_{fp})
- The density of the particles composing the filter, (ρ_{fp})

Several pressure transducers monitored the peak overpressure behind the blast wave along the shock tube, both before and after the filter, in order to determine the effects of the various parameters on the filter performance.

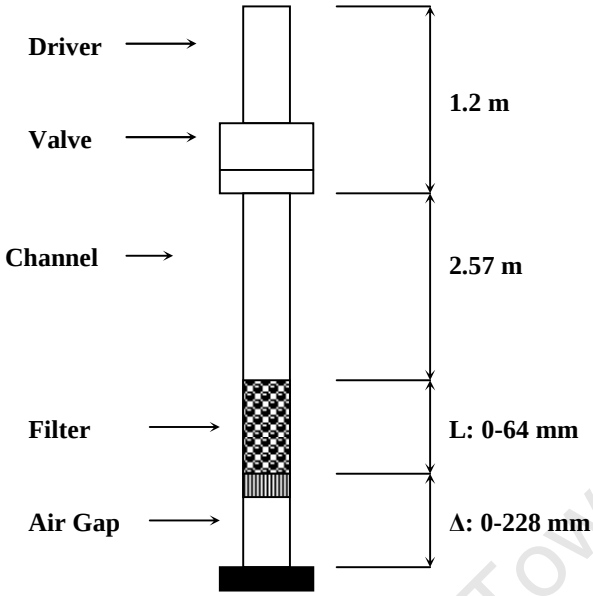

Figure 13: Granular filter experimental shock tube

The driver was filled with air at an initial pressure of 600 ±1 kPa whilst the air in the channel was at atmospheric pressure (100 kPa). The driver and the channel were separated by a pneumatic valve with a rise-time of approximately 1ms. The fast opening of the valve and the difference in pressure between the driver and channel produced a shock wave which propagated down the length of the channel toward the filter.

Britan and Ben-Dor *et al* [29] found, that increasing the filter length to particle diameter ratio (L/d_p), increases the energy loss and thus the larger the extent of the blast wave attenuation. Granular filters followed by an air gap, resulted in a decrease in the total stress transfer to the protected surface. Increasing the air gap behind the filter resulted in a decrease in blast wave pressure. Granular filters without an air gap caused a peak in the total stress higher than that of the test without a filter, making them counter productive.

(ii) Perforated Plates

Medvedev *et al* [28] investigated the use of perforated plates as a means of blast wave mitigation. Several circular plate designs were used, in which Medvedev *et al* [28] varied the number of holes in the plate, the size of the holes and the distance between the holes. A photograph of one of the perforated plates used by Medvedev *et al* [28] is shown in Figure 14. Medvedev *et al* [28] defined a blockage ratio (BR), as the ratio of the area of solid material to perforated material given by the following equation:

$$BR = 1 - \frac{N \times d_o^2}{D^2} \tag{2.21}$$

Where (N) is the total number of holes, (d_o) is the hole diameter and (D) is the overall disc diameter.

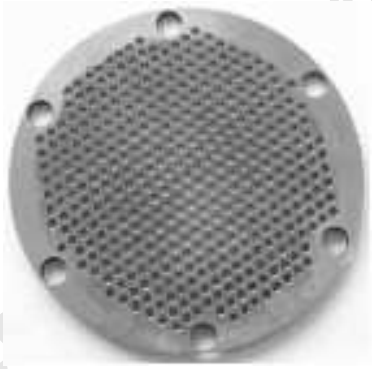

Figure 14: Photograph of a perforated plate used by Medvedev *et al* [28]

Medvedev *et al* [28] reported that from the experimental results, the blast front velocity could be decreased by increasing the blockage ratio. This can be achieved by decreasing the number of holes and/or the size of the holes. The most recent work regarding perforated plates was performed by Langdon *et al* [30] in the Blast Impact and Survivability Research Unit (BISRU) at the University of Cape Town. Langdon *et al* [30] investigated the effect of using thin steel perforated plates as a medium to mitigate blast waves.

A photograph of the test rig used by Langdon et al [30] is shown in Figure 15. The test rig consisted of six clamping plates and three cylindrical tubes. Five of the six clamping plates where threaded to allow for the plates to be screwed onto the cylindrical tubes. The sixth plate had a machined hole 106 mm in diameter corresponding to the inner diameter of the cylindrical tubes.

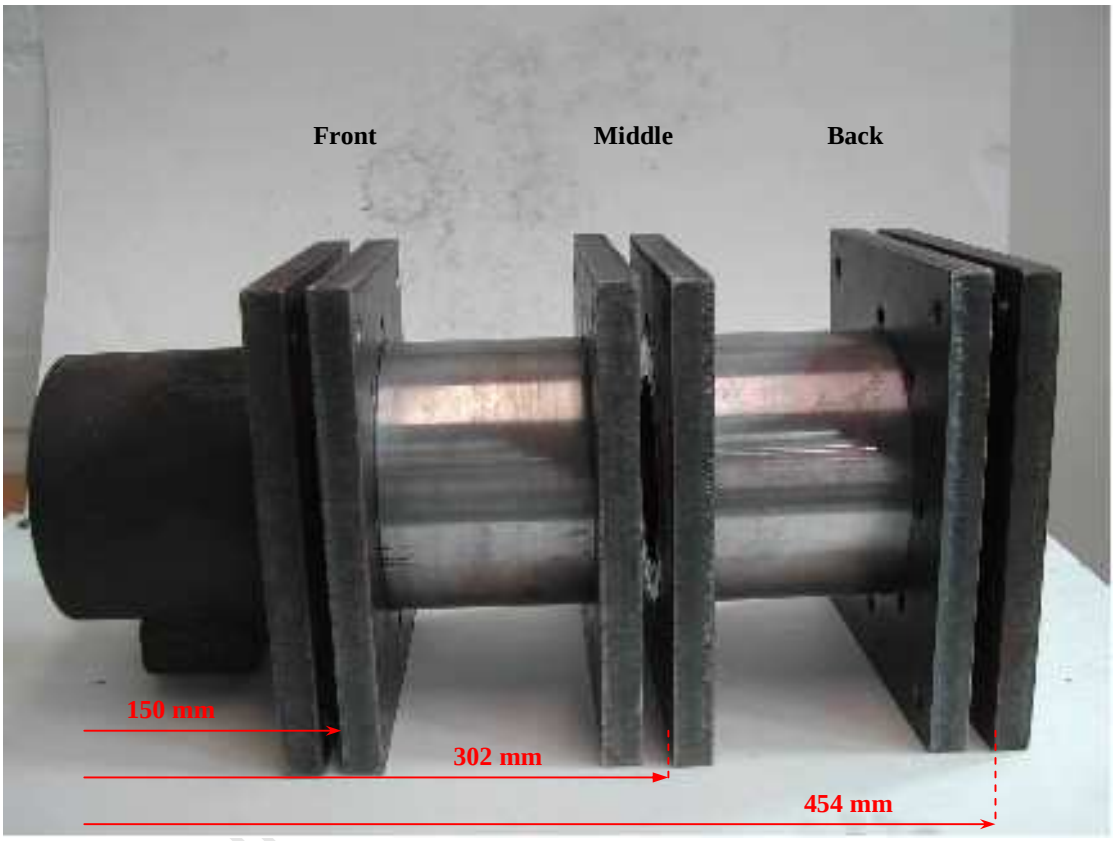

Figure 15: Photograph of the test rig used by Langdon et al [30]

A photograph of the perforated plate design used by Langdon et al [30] is shown in Figure 16, with the plate dimensions presented in Table 2. Mild steel target plates were used to gauge the effect of several parameters on the mitigation performance of the perforated plates, namely the number of plates placed between the explosive charge and the test plate, and their positioning/distance from the explosive charge, known as the stand-off distance (SOD).

Figure 16: Photograph of a perforated plate used by Langdon et al [30]

Thickness mm	Blockage ratio %	Diameter of exposed area mm
2	87	106

Table 2: Dimensions of perforated plates used by Langdon et al [30]

The following three perforated plate configurations were investigated by Langdon et al [30]:

1. One perforated plate was inserted in the front position followed by a target plate in the back position (F-B).

    - The SOD between the explosive and the perforated plate: 150 mm.
    - The SOD between the explosive and the target plate: 450 mm.
    - The separation distance between the plates: 300 mm.

2. One perforated plate was inserted in the middle position followed by a target plate in the back position (-MB).

    - The SOD between the explosive and the perforated plate: 300 mm.
    - The SOD between the explosive and the target plate: 450 mm.
    - The separation distance between the plates: 150 mm.

3. One perforated plate was inserted in both the front and middle positions followed by a target plate in the back position (FMB).

    - The SOD between the explosive and the front perforated plate: 150 mm.
    - The SOD between the explosive and the middle perforated plate: 300 mm.
    - The SOD between the explosive and the target plate: 450 mm.
    - The separation distance between the plates: 150 mm.

Langdon et al [30] also performed a series of tests with no perforated plate in between the blast wave and target plate (--B). A graph of target plate mid-point deflection versus impulse is shown in Figure 17. Langdon et al [30] reported that when using only one perforated plate the positioning was important. Increasing the SOD of the perforated plate and hence reducing the separation distance between the plates, increased the attenuation effect of the perforated plate. This effect was possibly due to the larger air gap and thus the blast wave attenuated itself more before it reached the perforated plate. Increasing the air gap also reduces the pressure build up between the plates. The insertion of one perforated plate between the blast wave and the target plate (F-B, -MB) reduced the target plate mid-point deflection by approximately 65%-75%. The insertion of two perforated plates (FMB) reduced the target plate mid-point deflection by approximately 90%-95%.

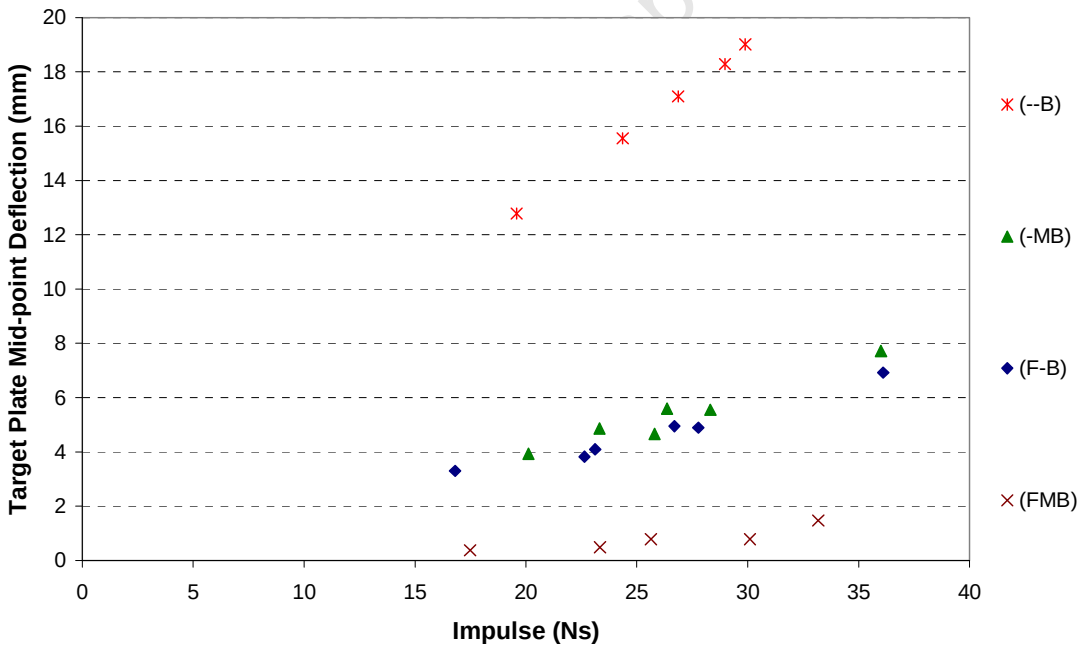

Figure 17: Graph of target plate mid-point deflection versus impulse [30]

3. Experimental Details

This chapter provides the details of blast loading experiments performed on circular mild steel plates by the author in the BISRU Laboratory at the University of Cape Town.

3.1 Experimental Procedure

3.1.1 Ballistic Pendulum

The Ballistic Pendulum, shown in Figure 18, is used to measure the impulse imparted to the plates. The pendulum consists of a steel I-beam suspended by four spring steel cables. The cables are attached to the I-beam by four adjustable screws. Counterweights are used to balance the weight of the test rig attached to the front side of the pendulum to ensure that the tension in each of the spring steel cables is the same. A soft tipped marker is attached to the pendulum on the same side as the counterweight to record the oscillation amplitude of the pendulum on tracing paper. The oscillation relates directly to the impulse generated by the explosive and transmitted to the plates.

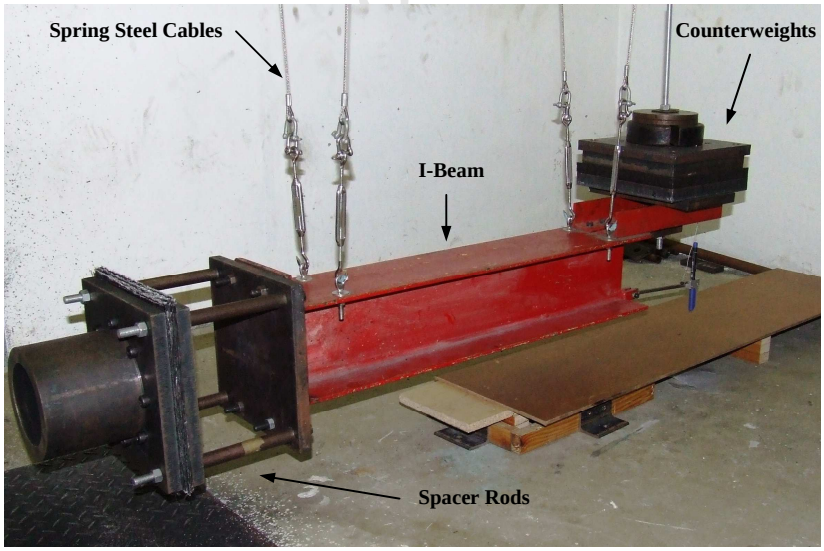

Figure 18: Photograph of ballistic pendulum

The methodology for calculating the impulse imparted to the plates is based on a single degree of freedom model and is given in Appendix B.

3.1.2 Test Rig

The test rig used in the experiments, shown in Figure 19, consisted of two clamping plates, a spacer plate and a cylindrical tube, all manufactured from mild steel. The spacer plate provided a separation distance of 25 mm between the perforated plate and the target plate, whilst the clamping plates secured the test plates in their relative positions. The cylindrical tube had a 106 mm inner diameter and provided a stand-off distance of 300 mm between the explosive and the perforated plate.

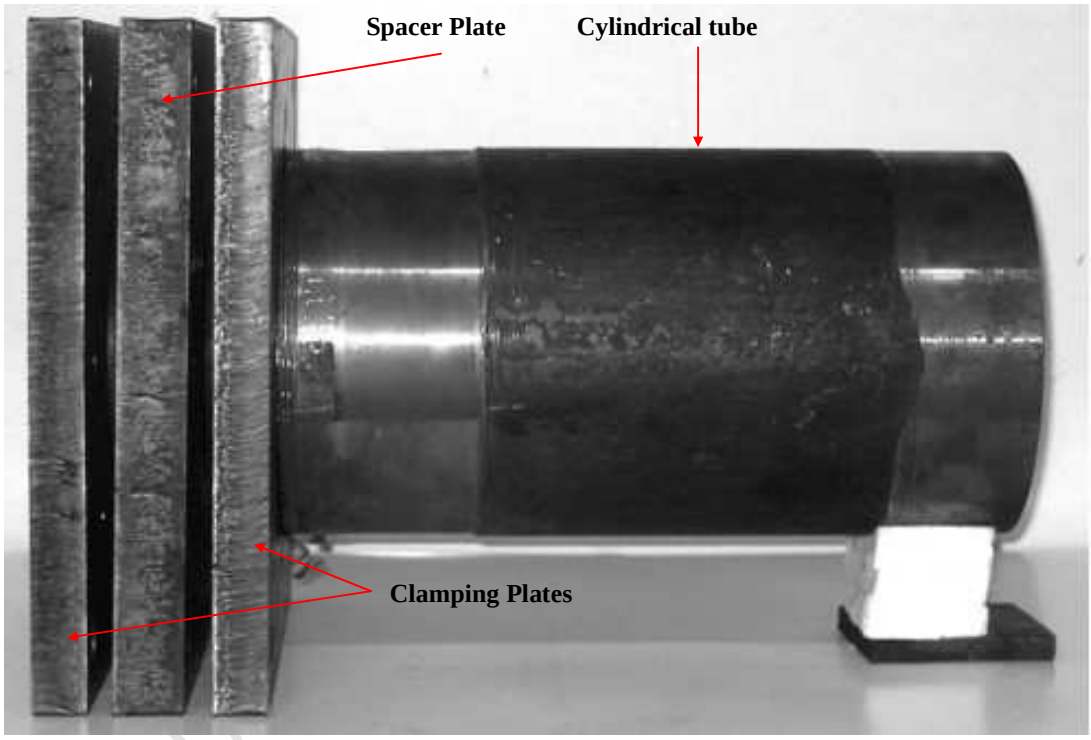

Figure 19: Photograph of test rig used in the experiments

A sectional view of the test rig is shown in Figure 20, indicating the relative positioning of the plates as well as the explosive layout which is discussed in detail in section 3.1.3.

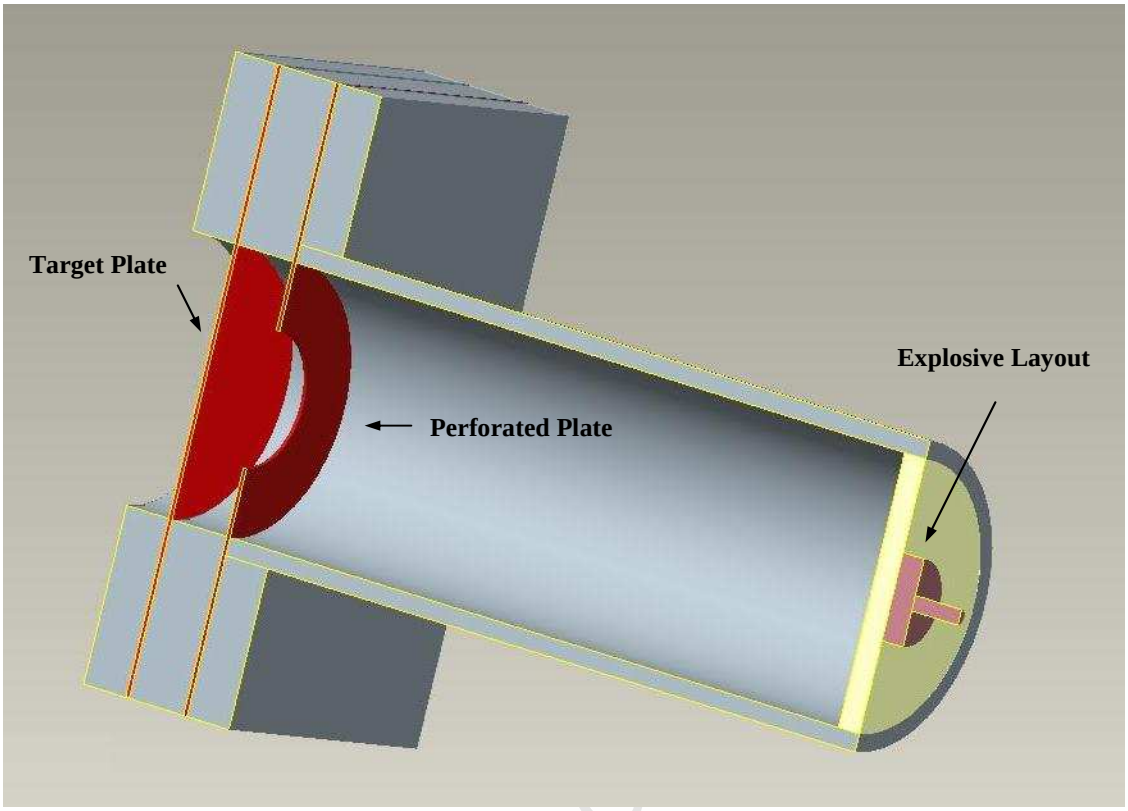

Figure 20: Cross sectional view of test rig

The test rig was mounted to the ballistic pendulum using four spacer rods, shown in Figure 18, allowing the target plate to deform without coming into contact with the pendulum I-beam.

3.1.3 Explosive Load Geometry and Material Properties

The plates were loaded by detonating plastic explosive #4, commonly known as PE4, a combination of RDX and Lithium grease. The material composition, density and detonation velocity of PE4 are listed in Table 3.

PE4 Properties	
% RDX	88
% Lithium Grease	12
Density g/cm^3	1.6
Detonation Velocity m.s^{-1}	8200

Table 3: PE4 material composition [31]

The explosive was shaped into a 34mm diameter circular disk and placed onto a polystyrene pad shown in Figure 21A. A one gram leader was attached to the detonator, providing a means of attaching the detonator to the main charge. A photograph of the detonator is shown in Figure 21B.

A **B**

Figure 21: Photograph of explosive layout (A) and the detonator (B)

The polystyrene pad was then inserted into the front end of the cylindrical tube providing a stand-off distance of 300 mm. The charge was detonated and the blast wave directed down the cylindrical tube toward the plates.

3.1.4 Test Plate Dimensions and Material Properties

Two types of test plates were used for the experiments, namely a target plate (TP) and a perforated plate (PP) shown in Figure 22A and Figure 22B respectively. The plates had a circular exposed area, indicated by the cross hatched region, with a diameter of 106 mm. The target plates had a thickness of 1.6 ± 0.04 mm whilst two perforated plate thicknesses were used, namely 1.6 ± 0.04 mm (classified as deformable) and a nominal thickness of 25 mm (classified as rigid).

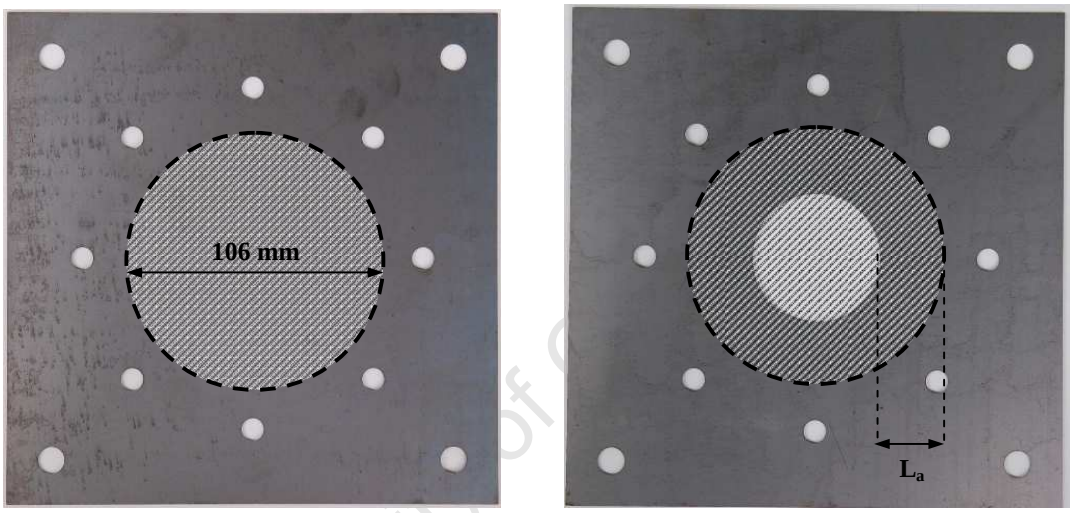

Figure 22: Photographs of the target plate (A) and perforated plate (B)

The arm length of the perforated plate is defined as the distance from the boundary of the exposed area to the edge of the perforation, marked (L_a) in Figure 22B. The arm length parameter was used to describe the perforated plate deformation and in the analysis of the AUTODYN simulations. The perforated plate dimensions are given in Table 4 and Table 5 for plate thicknesses of 1.6mm and 25mm respectively. The blockage ratios where calculated using equation 2.21.

$$BR = 1 - \frac{N \times d_o^2}{D^2} \qquad \text{(Recall 2.21)}$$

Perforated Plate Thickness 1.6 ± 0.04 mm		
Perforated Plate Hole Diameter mm	**Blockage Ratio %**	**Arm Length mm**
92	25	7
75	50	15.5
63	65	21.5
53	75	26.5
35	89	35.5
21	96	42.5

Table 4: Perforated plate dimensions for a plate thickness of 1.6 ± 0.04 mm

Perforated Plate Thickness 25 mm		
Perforated Plate Hole Diameter mm	**Blockage Ratio %**	**Arm Length mm**
53	75	26.5
35	89	35.5

Table 5: Perforated plate dimensions for a nominal plate thickness of 25 mm

The plates were cut from several sheets of mild steel labelled A to F. Uni-axial quasi-static tensile tests were performed at a strain rate of 0.001 s^{-1} to determine the material properties of each sheet. Assuming the mild steel to be rigid-viscoplastic, static yield stresses were calculated using the Cowper-Symonds [32] relation:

$$\frac{\sigma_d}{\sigma_0} = \left(1 + \left(\frac{\dot{\varepsilon}}{D}\right)^{\frac{1}{q}}\right) \tag{3.1}$$

Where (σ_d) is the dynamic yield stress, (σ_0) is the static yield stress, (D) and (q) are material parameters. The values used in this study are D = 844 s^{-1} and q = 2.207 which were found experimentally [33] using mild steel obtained from a locally based supplier. The static yield stresses for each sheet of mild steel are presented in Table 6.

Sheet Number	**Static Yield Stress (MPa)**
A	179
B	192
C	251
D	311
E	234
F	237

Table 6: Mild steel material properties determined from uni-axial tensile tests

3.2 Experimental Measurement and Notation

3.2.1 Impulse

The impulse is calculated from the displacement of the ballistic pendulum. The equations relating the ballistic pendulum displacement to the impulse are given in Appendix B.

3.2.2 Test Plate Deflections

A digital height gauge with an accuracy of ±0.01mm was used to measure the target plate mid-point deflection and the perforated plate average deflection around the edge of the perforation. The target plates were sectioned about the plate centreline and photographed as a means of illustrating the deflection profiles of the plates. One quarter of each perforated plate was sectioned, as shown in Figure 23, and photographed.

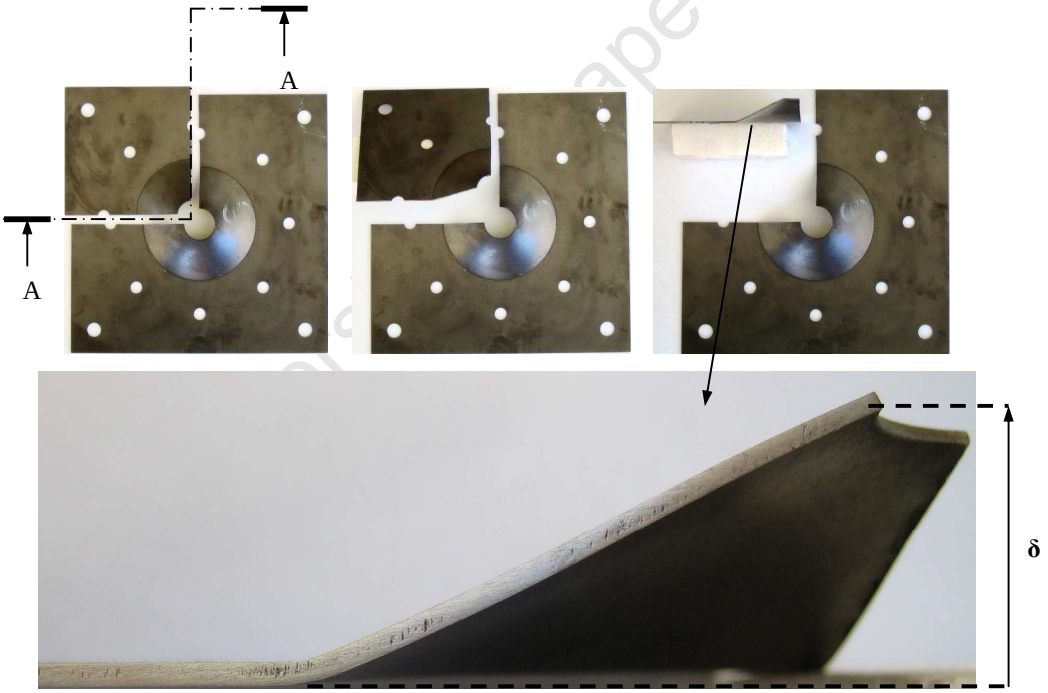

Figure 23: Photograph of the perforated plate cross-section A-A

3.2.3 Test Plate Notation

Each plate was labelled according to the blockage ratio of the perforated plate used, whether or not the perforated plate was classed as deformable, indicated by a “D” or rigid, indicated by an “R” and the mass of explosive used in the test. For example, for a test with a deformable perforated plate with a blockage ratio of 96% and a charge mass of 5 grams including the leader, both plates were marked as follows: BR96D_4+1.

4. Experimental Results

This chapter describes the results from blast tests performed on clamped circular mild steel plates. A total of 63 tests were performed in which both the perforated plate hole size and thickness were varied. A summary of the measured test data is presented in Section 4.2 and a full analysis of the results is given in Chapter 5.

4.1 General Plate Deformation

Large plastic deformation typical of Mode I failure was observed in most cases for both the target plates and perforated plates. The target plate profile resembled a uniform global dome, similar to the results reported by Jacob [16] for stand off distances greater than 100 mm. A photograph of the target plate cross-section is shown in Figure 24, for test BR89R_15+1.

Figure 24: Photograph of target plate cross-section for test BR89R_15+1 (I = 33.2Ns)

A photograph of the perforated plate cross-section is shown in Figure 25, for test BR96D_14+1. The perforated plate deforms about a plastic hinge at the boundary at the edge of the clamp frame indicated by the dashed line.

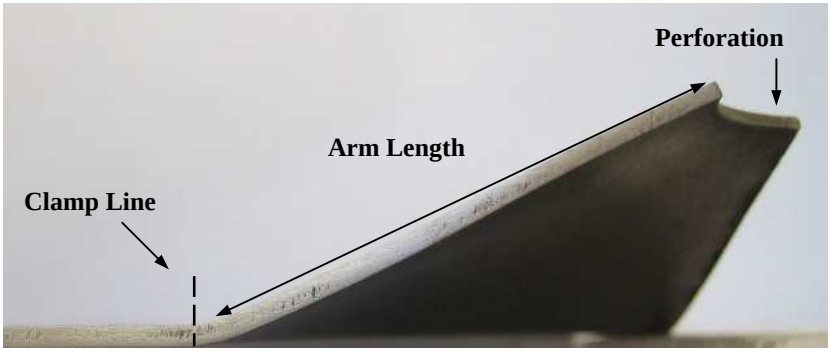

Figure 25: Photograph of perforated plate cross-section for test BR96D_14+1 (I = 30.9 Ns)

Thinning at the boundary was observed for all of the target plates, followed by partial or complete tearing once the threshold impulse had been achieved for the respective blockage ratio. The threshold impulse is defined as the impulse at which partial or complete tearing occurs for a given blockage ratio. A photograph illustrating thinning at the boundary of the target plate is shown in Figure 26, for test BR89R_15+1.

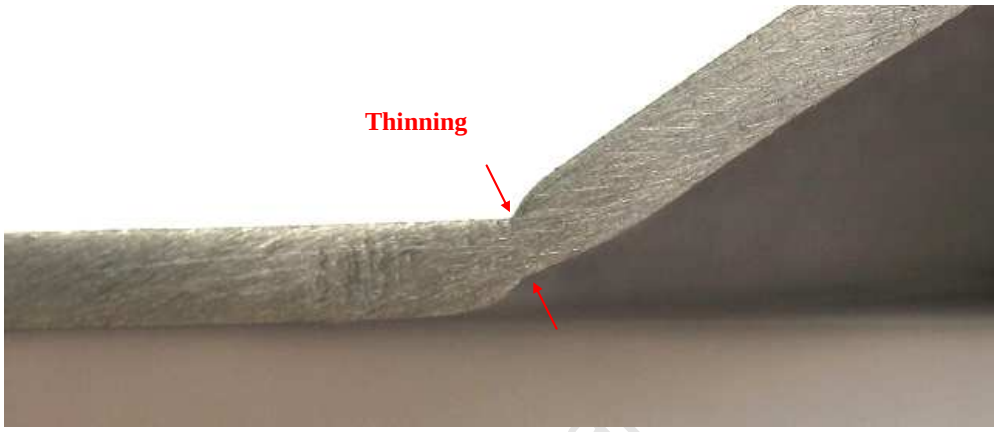

Figure 26: Photograph of thinning at the boundary of the target plate for test BR89R_15+1 (I = 33.2Ns)

Some plates exhibited partial tearing, for example in tests with blockage ratios of 65% and 89 %, the target plates tore around most of the boundary at impulses of 20.0 Ns and 26.8 Ns respectively. A photograph of a typical partially torn plate is shown in Figure 27, for test BR65D_9+1.

Figure 27: Photo graph of partial tearing at the boundary of the target plate for test BR65D_9+1 (I = 20.0Ns)

Other plates exhibited complete tearing, for example in tests with blockage ratios of 25%, 50% and 75%, the target plates tore around the entire boundary at impulses of 25.4 Ns, 21.4Ns and 24.7Ns respectively. The threshold impulse for tearing was not reached for a blockage ratio of 96 %. A photograph of a typical torn plate exhibiting complete tearing at the boundary is shown in Figure 28, for test BR75D_12+1. To the right of the plate in Figure 28, is the circular disc. As the discs tears away from the plate it impacts the pendulum, further deforming its shape.

Figure 28: Photograph of complete tearing at the boundary of the target plate for test BR75D_12+1 (I = 24.7Ns)

4.2 Summary of Experimental Results

A summary of the experimental results are presented in Table 7 through Table 10 for the deformable perforated plates for all blockage ratios and in Table 11 for the rigid perforated plates. The results are discussed in detail in Chapter 5. The data points that are highlighted were not included in the graphs as they appear to be anomalous.

Test Number	Charge Mass (g)	Charge Height (mm)	Impulse (Ns)	Blockage Ratio %	Perforation Diameter (mm)	PP Thickness (mm)	TP Thickness (mm)	PP average deflection (mm)	TP mid-point deflection (mm)
BR0D_4+1	5	3.44	12.1	0	-	-	1.6	-	9.16
BR0D_6+1	7	4.82	14.6	0	-	-	1.6	-	12.05
BR0D_8+1	9	6.20	19.7	0	-	-	1.62	-	14.54
BR0D_10+1	11	7.57	24.7	0	-	-	1.62	-	17.16
BR0D_12+1	13	8.95	25.7	0	-	-	1.6	-	19.05
BR0D_14+1	15	10.33	31.8	0	-	-	1.6	-	Torn
BR25D_4+1	5	3.44	11.2	25	92	1.6	1.6	-0.39	9.36
BR25D_6+1	7	4.82	15.6	25	92	1.6	1.6	-0.49	12.76
BR25D_8+1	9	6.20	19.9	25	92	1.62	16.2	-0.59	15.45
BR25D_9+1	10	6.88	21.1	25	92	1.62	16.4	-0.41	16.48
BR25D_10+1	11	7.57	22.0	25	92	1.62	15.8	-0.73	18.38
BR25D_12+1	13	8.95	25.4	25	92	1.6	1.6	-0.73	Torn

Table 7: Summary of experimental results for blockage ratios of 0% and 25%

Test Number	Charge Mass (g)	Charge Height (mm)	Impulse (Ns)	Blockage Ratio %	Perforation Diameter (mm)	PP Thickness (mm)	TP Thickness (mm)	PP average deflection (mm)	TP mid-point deflection (mm)
BR50D_4+1	5	3.44	11.2	50	75	1.64	1.64	-0.46	9.53
BR50D_6+1	7	4.82	15.6	50	75	1.62	1.58	-0.45	12.20
BR50D_8+1	9	6.20	18.9	50	75	1.58	1.58	-0.87	14.79
BR50D_9+1	10	6.88	20.4	50	75	1.62	1.60	-1.24	16.17
BR50D_9+1	10	6.88	22.9	50	75	1.64	1.62	-1.31	16.30
BR50D_10+1	11	7.57	20.7	50	75	1.60	1.64	-1.29	Torn
BR50D_10+1	11	7.57	21.3	50	75	1.60	1.64	-1.68	Torn
BR65D_4+1	5	3.44	11.5	65	63	1.58	1.58	0.40	8.26
BR65D _6+1	7	4.82	16.0	65	63	1.60	1.60	0.25	11.67
BR65D _8+1	9	6.20	19.1	65	63	1.64	1.64	0.35	14.50
BR65D _9+1	10	6.88	20.0	65	63	1.60	1.60	2.02	Torn

Table 8: Summary of experimental results for blockage ratios of 50% and 65%

Test Number	Charge Mass (g)	Charge Height (mm)	Impulse (Ns)	Blockage Ratio %	Perforation Diameter (mm)	PP Thickness (mm)	TP Thickness (mm)	PP average deflection (mm)	TP mid-point deflection (mm)
BR75D_4+1	5	3.44	13.4	75	53	1.60	1.60	0.32	8.40
BR75D _6+1	7	4.82	16.5	75	53	1.62	1.58	1.49	10.87
BR75D _8+1	9	6.20	20.1	75	53	1.62	1.58	1.71	12.86
BR75D _9+1	10	6.88	21.2	75	53	1.60	1.60	-0.75	Torn
BR75D _9+1	10	6.88	22.3	75	53	1.58	1.60	2.46	13.91
BR75D _10+1	11	7.57	24.1	75	53	1.62	1.60	1.08	15.55
BR75D _12+1	13	8.95	24.7	75	53	1.60	1.64	4.62	Torn
BR89D_4+1	5	3.44	11.8	89	35	1.60	1.60	5.43	6.60
BR89D _6+1	7	4.82	16.7	89	35	1.58	1.58	7.39	8.60
BR89D _8+1	9	6.20	19.9	89	35	1.57	1.58	8.53	10.71
BR89D _9+1	10	6.88	21.4	89	35	1.57	1.62	9.07	11.52
BR89D _10+1	11	7.57	22.3	89	35	1.58	1.60	10.62	11.92
BR89D _11+1	12	8.26	25.5	89	35	1.58	1.60	11.49	13.79
BR89D _12+1	13	8.95	26.8	89	35	1.58	1.58	10.54	Torn

Table 9: Summary of experimental results for blockage ratios of 75% and 89%

Test Number	Charge Mass (g)	Charge Height (mm)	Impulse (Ns)	Blockage Ratio %	Perforation Diameter (mm)	PP Thickness (mm)	TP Thickness (mm)	PP average deflection (mm)	TP mid-point deflection (mm)
BR96D_4+1	5	3.44	11.3	96	21	1.60	1.64	9.03	3.60
BR96D _6+1	7	4.82	16.5	96	21	1.58	1.58	10.89	5.73
BR96D _8+1	9	6.20	20.2	96	21	1.58	1.58	12.21	7.29
BR96D _9+1	10	6.88	21.2	96	21	1.58	1.58	13.66	7.97
BR96D _10+1	11	7.57	22.6	96	21	1.58	1.58	14.97	7.88
BR96D _12+1	13	8.95	27.2	96	21	1.58	1.58	16.40	8.98
BR96D _14+1	15	10.33	30.9	96	21	1.58	1.58	18.55	9.95
BR96D _16+1	17	11.70	31.5	96	21	1.64	1.60	18.89	11.41
BR96D _18+1	19	13.08	31.9	96	21	1.60	1.64	20.27	11.63
BR96D _20+1	21	14.46	35.9	96	21	1.60	1.60	20.49	13.31

Table 10: Summary of experimental results for a blockage ratio of 96%

Test Number	Charge Mass (g)	Charge Height (mm)	Impulse (Ns)	Blockage Ratio %	Perforation Diameter (mm)	PP Thickness (mm)	TP Thickness (mm)	PP average deflection (mm)	TP mid-point deflection (mm)
BR75R_4+1	5	3.44	13.7	75	53	26.68	1.58	-	8.44
BR75R _6+1	7	4.82	15.2	75	53	26.68	1.60	-	11.32
BR75R _8+1	9	6.20	21.6	75	53	26.68	1.58	-	13.74
BR75R _9+1	10	6.88	23.1	75	53	26.68	1.58	-	15.34
BR75R _10+1	11	7.57	21.4	75	53	26.68	1.62	-	Torn
BR75R _12+1	13	8.95	26.6	75	53	26.68	1.58	-	Torn
BR89R_4+1	5	3.44	11.2	89	35	26.68	1.60	-	5.38
BR89R _6+1	7	4.82	16.1	89	35	26.68	1.60	-	8.28
BR89R _8+1	9	6.20	19.7	89	35	26.68	1.60	-	10.89
BR89R _9+1	10	6.88	22.3	89	35	26.68	1.58	-	11.16
BR89R _10+1	11	7.57	24.9	89	35	26.68	1.58	-	12.26
BR89R _12+1	13	8.95	28.2	89	35	26.68	1.58	-	14.17
BR89R _14+1	15	10.33	31.6	89	35	26.68	1.58	-	15.53
BR89R _15+1	16	11.01	33.2	89	35	26.68	1.58	-	14.92
BR89R _16+1	17	11.70	34.4	89	35	26.68	1.60	-	15.60
BR89R _18+1	19	13.08	31.9	89	35	26.68	1.62	-	Torn

Table 11: Summary of experimental results for a rigid perforated plate with blockage ratios of 75% and 89%

5. Analysis of Experimental Results

5.1 Relationship between impulse and charge mass

The relationship between impulse and charge mass is shown in Figure 29 for all the experiments. The impulse increases with an increase in charge mass. A best-fit trend line for the relationship between Impulse (I) and Charge mass (m) is a second order polynomial given by the following equation:

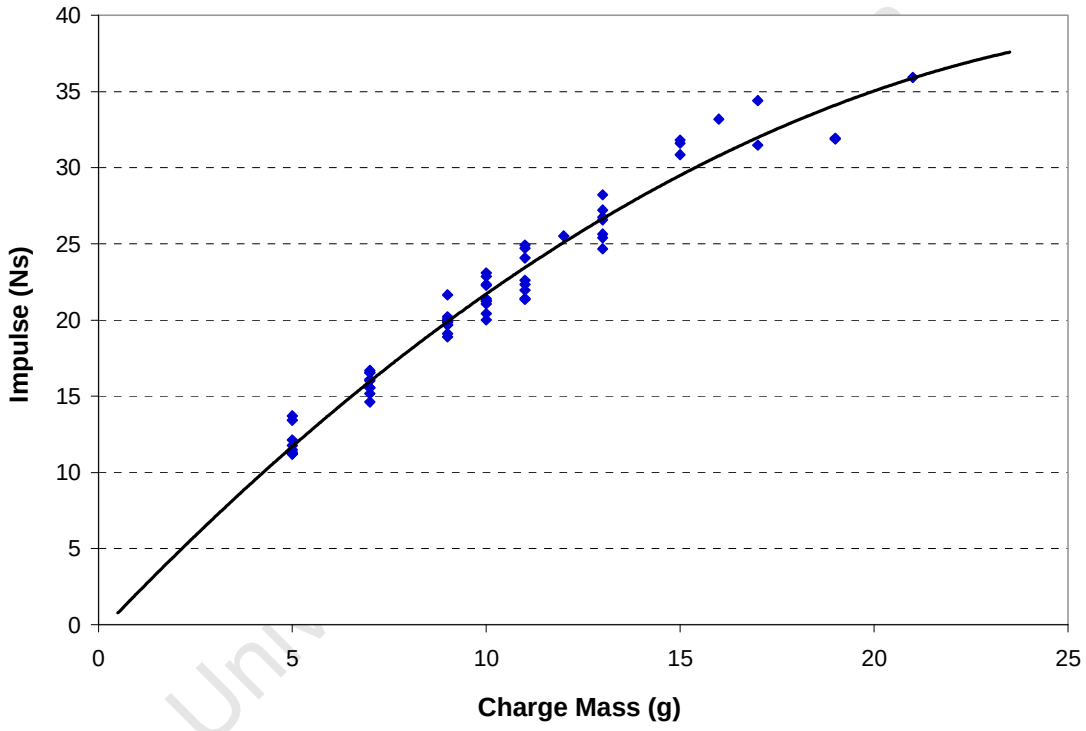

Figure 29: Graph of impulse versus charge mass for all experiments

$$I = -0.0428m^2 + 2.6274m - 0.3454 \quad (5.1)$$

The impulse to charge mass ratio decreases with an increase in charge mass and appears to asymptote. A possible reason for this is the effective mass of explosive. Kennedy [34] explains that the lateral edges of the explosive charge must be subtracted from the total mass in order to estimate the effective mass of explosive that will drive a metal plate to

its maximum velocity. The effective mass is calculated by removing the expected unreacted explosive, measured at 30° to the side of the charge mass, as shown in Figure 30 for two charge masses with constant diameter (d). In each case the shaded region indicates the effective mass of explosive. In cases where the explosive charge diameter is held constant, a maximum effective mass and corresponding height will be reached, beyond which any further increase will not contribute much to the maximum velocity of the plate. The height at which the maximum effective mass occurs is labelled h_{ME}.

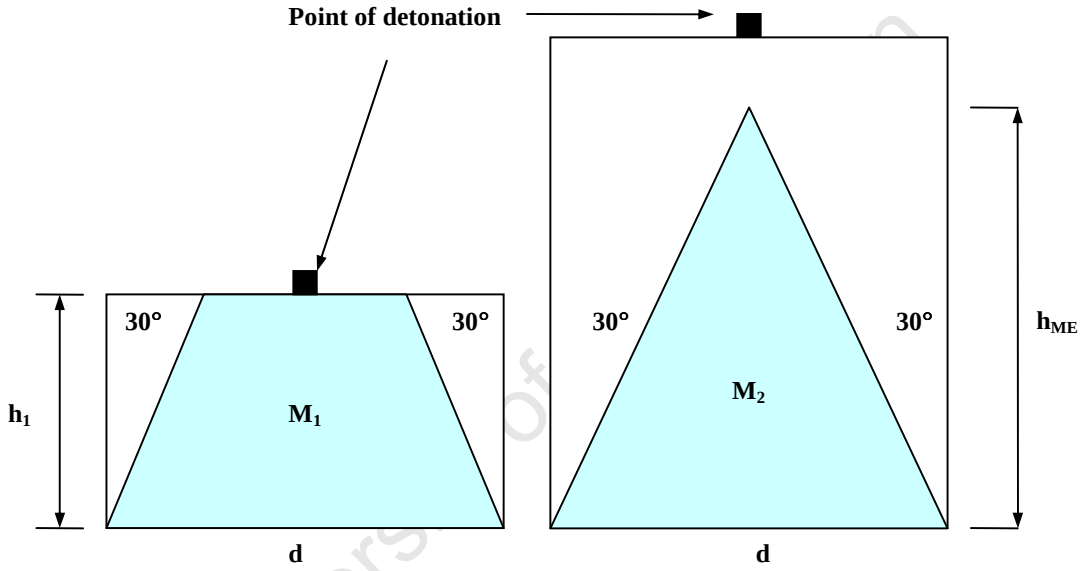

Figure 30: Diagram illustrating the effective mass of explosive indicated by the shaded region

The height at which the maximum effective mass occurs for a given diameter is given by the following equation:

$$h_{ME} = \frac{d}{2\tan 30^{\circ}} \tag{5.2}$$

For a diameter of 34 mm the maximum effective mass occurs at a height of 29.4 mm corresponding to a mass of approximately 42.7 grams.

5.2 Relationship between Impulse and Test Plate Deflection

5.2.1 Relationship between Impulse and Target Plate Mid-Point Deflection

The measured mid-point deflection of the target plates increases with an increase in impulse for all blockage ratios as shown in Figure 31. The orange line indicates the baseline blockage ratio of 0%, where there was no perforated plate in-between the explosive and the target plate. The arrows at the end of each trend line indicate the point at which tearing of the target plate occurs. Tearing for a blockage ratio of 96% was not achieved.

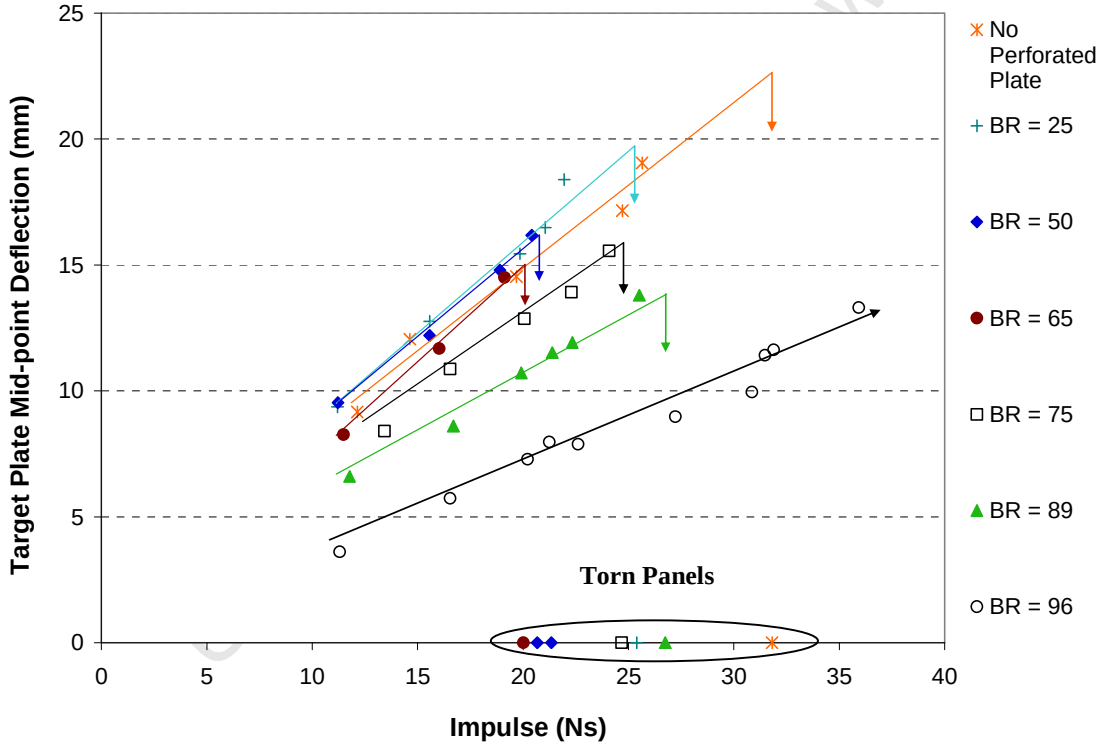

Figure 31: Graph of target plate mid-point deflection versus impulse for all blockage ratios

The following observations were made, from Figure 31:

- For blockage ratios of 25% and 50%, increasing the blockage ratio increases the target plate mid point deflection relative to the baseline ratio.
- A blockage ratio of 65% has little or no effect on the target plate mid point deflection.
- Any further increase in the blockage ratio results in a decrease in the target plate mid point deflection.

Photographs of the cross-sections of target plates for the baseline blockage ratio of 0% are shown in Figure 32 and photographs of plates with other blockage ratios (25% to 96%) are shown in Figure 33 to Figure 38. The target plates exhibited large plastic deformation typical of Mode I failure, with the target plate profile resembling that of a uniform global dome. Similar target plate profiles were reported by Jacob [16] for stand off distances greater than 100mm. The profiles appear to become more uniform with an increase in blockage ratio.

Figure 32: Photograph of the cross-sections of the target plates for the baseline blockage ratio of 0%

Figure 33: Photograph of the cross-sections of the target plates for a blockage ratio of 25%

Figure 34: Photograph of the cross-sections of the target plates for a blockage ratio of 50%

Figure 35: Photograph of the cross-sections of the target plates for a blockage ratio of 65%

Figure 36: Photograph of the cross-sections of the target plates for a blockage ratio of 75%

Figure 37: Photograph of the cross-sections of the target plates for a blockage ratio of 89%

Figure 38: Photograph of the cross-sections of the target plates for a blockage ratio of 96%

(Only 6 out of 10 plate values are labelled for comparison with other blockage ratios)

5.2.2 Relationship between Impulse and Perforated Plate Average Deflection

The general trend for the perforated plates for all blockage ratios was an increase in the average deflection magnitude with an increase in impulse. A graph of perforated plate average deflection versus impulse is shown in Figure 39.

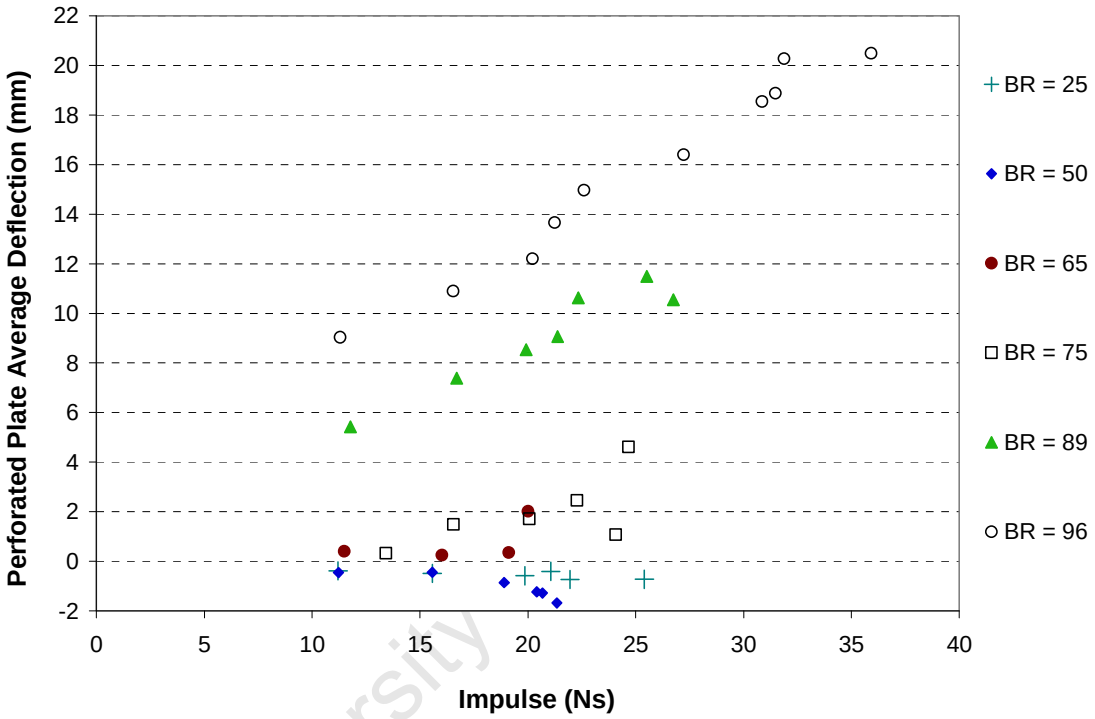

Figure 39: Graph of perforated plate average deflection versus impulse

The graph shows three possible deflection regions depending upon the blockage ratio.

1. For blockage ratios of 25% and 50%:

- The perforated plate deflection is opposite to the direction of the initial blast.
- The perforated plates deform about a plastic hinge at the boundary, with no significant damage along the arm length.

Photographs of the cross-sections of the perforated plates for blockage ratios of 25% and 50% are shown in Figure 40 and Figure 41 respectively. The edge of the clamp frame is indicated by the dashed line.

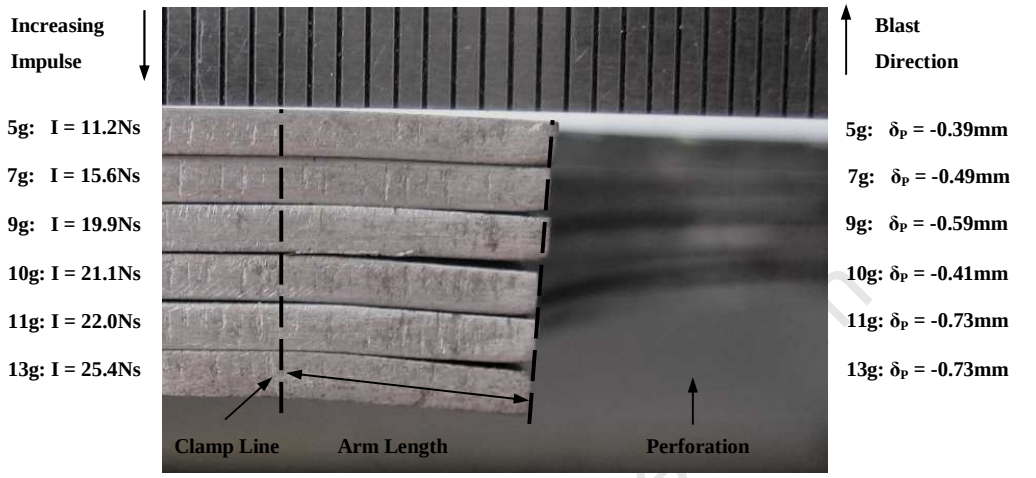

Figure 40: Photograph of the cross-sections of the perforated plates for a blockage ratio of 25%: plate deflection in direction opposite to that of the initial blast

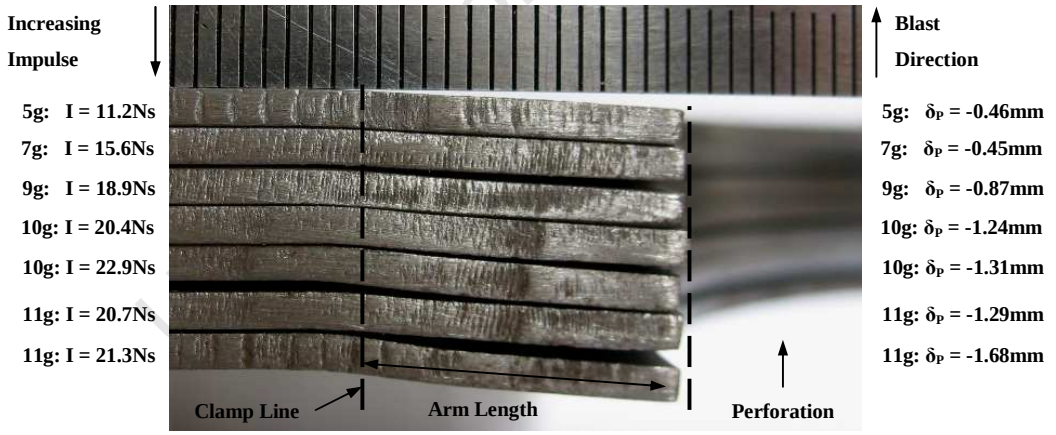

Figure 41: Photograph of the cross-sections of the perforated plates for a blockage ratio of 50%: plate deflection in direction opposite to that of the initial blast

2. For blockage ratios of 65% and 75%:

- Each perforated plate exhibited deflections in the direction of the initial blast and opposite to the direction of the initial blast. Possible reasons for this "buckling" effect shown in Figure 42, are material imperfections, variations in thickness, non-centralization of the blast wave as it comes into contact with the perforated plate and slight variations in the centralization of the hole. The perforated plate deflections recorded in Table 8 and Table 9 are average values.
- The perforated plates for a blockage ratio of 65% show little or no average deflection. Only three tests were performed that did not result in tearing of the target plate. The average deflections of the perforated plates range from 0.25 to 0.4 mm. An increase in impulse had little effect on the average deflections of the perforated plates. This was due to the pressure build up between the test plates.
- An impulse of 20Ns resulted in tearing of the target plate which alleviated the pressure build up between the plates and enabled the perforated plate to fully deflect, with a final measured deflection of 2.02 mm. A photograph of the cross-sections of the perforated plates for a blockage ratio of 65% is shown in Figure 43.

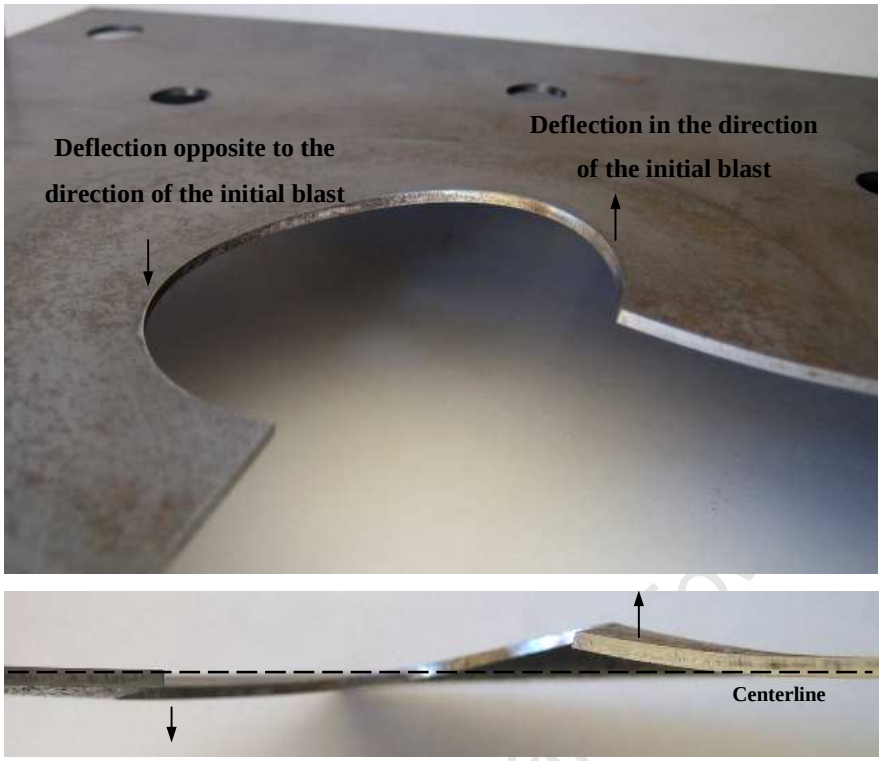

Figure 42: Photograph of the cross-section of the perforated plate for test BR75D_8+1 (I = 20.1Ns), plate deforms both in the direction of the initial blast and opposite to the direction of the initial blast

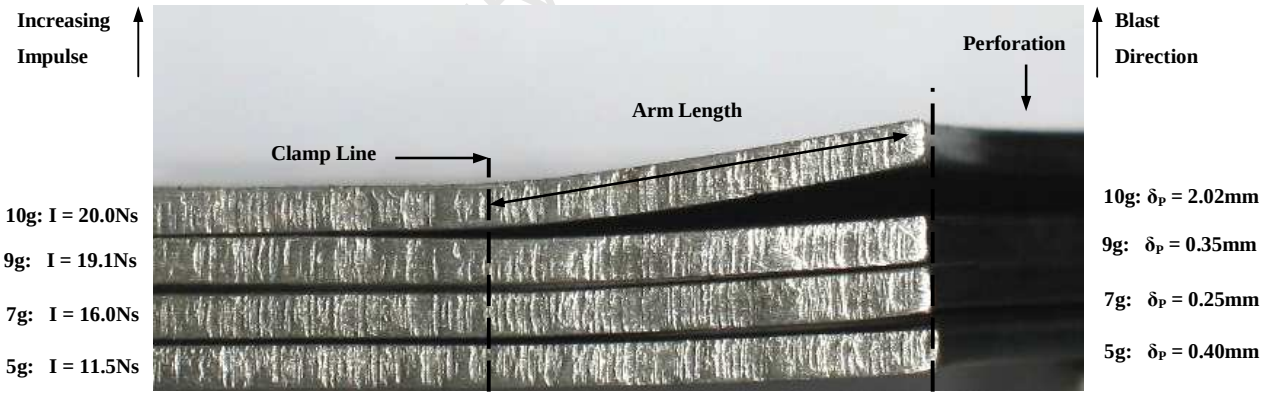

Figure 43: Photograph of the cross-sections of the perforated plates for a blockage ratio of 65%: plates deform both in the direction of the initial blast and opposite to the direction of the initial blast

3. For blockage ratios of 89% and 96%:

- The perforated plate deflections are in the same direction as the initial blast.
- The perforated plates show similar deformation characteristics to those for blockage ratios of 25% and 50%, deforming about a plastic hinge at the boundary.
- There is no significant bulging along the arm length for the majority of the plates. At the highest impulse of 35.9Ns, for a blockage ratio of 96% there was some bulging along the arm length. Photographs of the cross-sections of the perforated plates for blockage ratios of 89% and 96% are shown in Figure 44 and Figure 45 respectively.

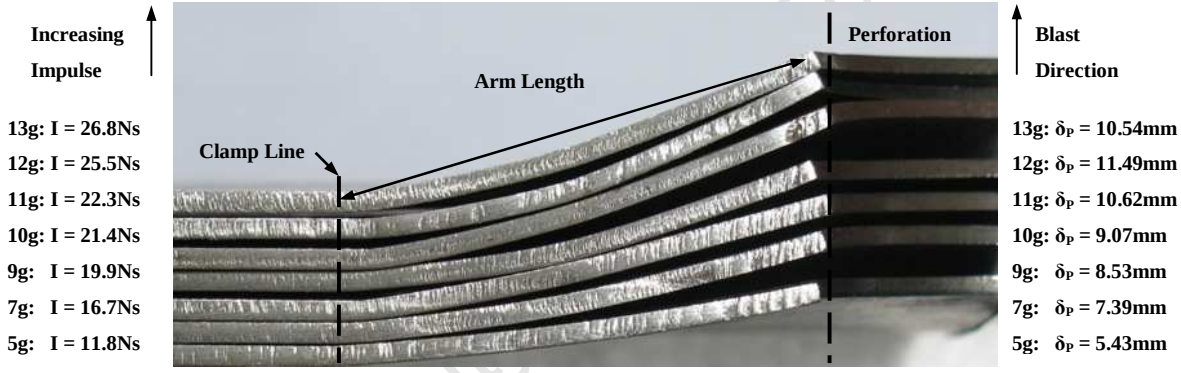

Figure 44: Photograph of the cross-sections of the perforated plates for a blockage ratio of 89%: plate deflection in same direction as the initial blast

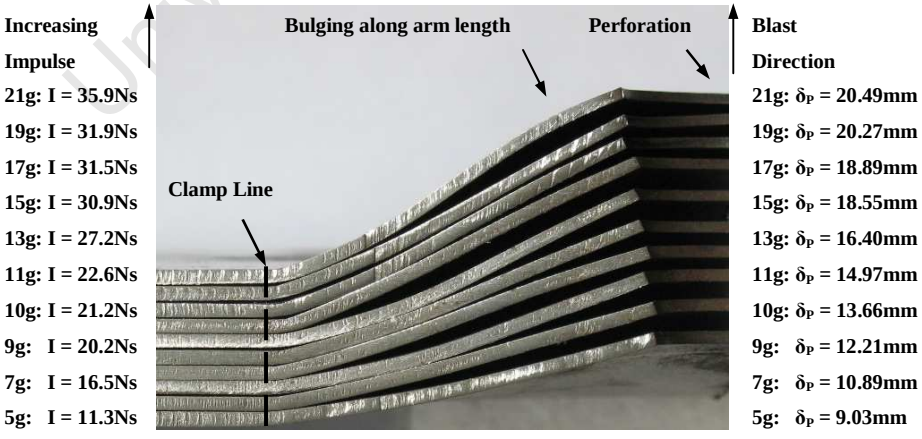

Figure 45: Photograph of the cross-sections of the perforated plates for a blockage ratio of 96%: plate deflection in same direction as the initial blast

5.3 Relationship between the Blockage Ratio and the Target Plate Mid-point Deflection

A graph of target plate mid-point deflection versus blockage ratio is shown in Figure 46 for the average measured impulse for all charge masses. All observations are made relative to the mid-point deflection of the target plate for the baseline blockage ratio of 0% (that is, no perforated plate in between the explosive and the target plate).

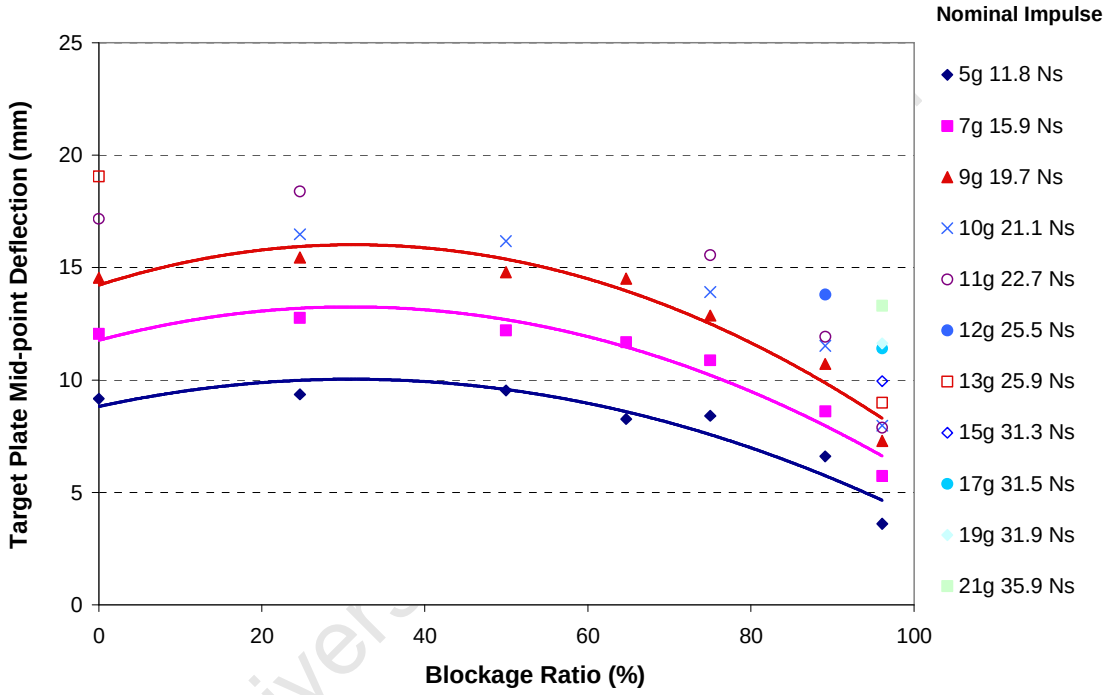

Figure 46: Graph of target plate mid-point deflection versus blockage ratio

The following observations were made, from Figure 46:

- At lower impulses an increase in blockage ratio from the baseline ratio of 0% to 25% or 50% had no significant effect on the mid-point deflection of the target plate.
- At higher impulses (namely 19.7Ns and 22.7Ns) an increase in blockage ratio from the baseline ratio of 0% to 25% caused a slight increase in the mid-point deflection of the target plate.

- Increase in blockage ratio above 50% resulted in a decrease in the mid-point deflection. A best-fit trend line for charge masses of 5g, 7g and 9g are shown in Figure 46. All other charge masses had an insufficient number of data points to accurately predict a trend. The best-fit trend line for each charge mass is a second order polynomial given by the following equations:

$$5g: \delta_T = -0.0013BR^2 + 0.0785BR + 8.8176 \quad (5.3)$$

$$7g: \delta_T = -0.0016BR^2 + 0.0963BR + 11.762 \quad (5.4)$$

$$9g: \delta_T = -0.0018BR^2 + 0.1149BR + 14.216 \quad (5.5)$$

5.4 Relationship between Blockage Ratio and the Perforated Plate Average Deflection

The perforated plate average deflection is given as a function of blockage ratio in Figure 47, for the average measured impulse for all charge masses. Positive average deflection values indicate plate deflections in the same direction as the blast wave, whilst negative average deflection values indicated plate deflections in the opposite direction to that of the blast wave.

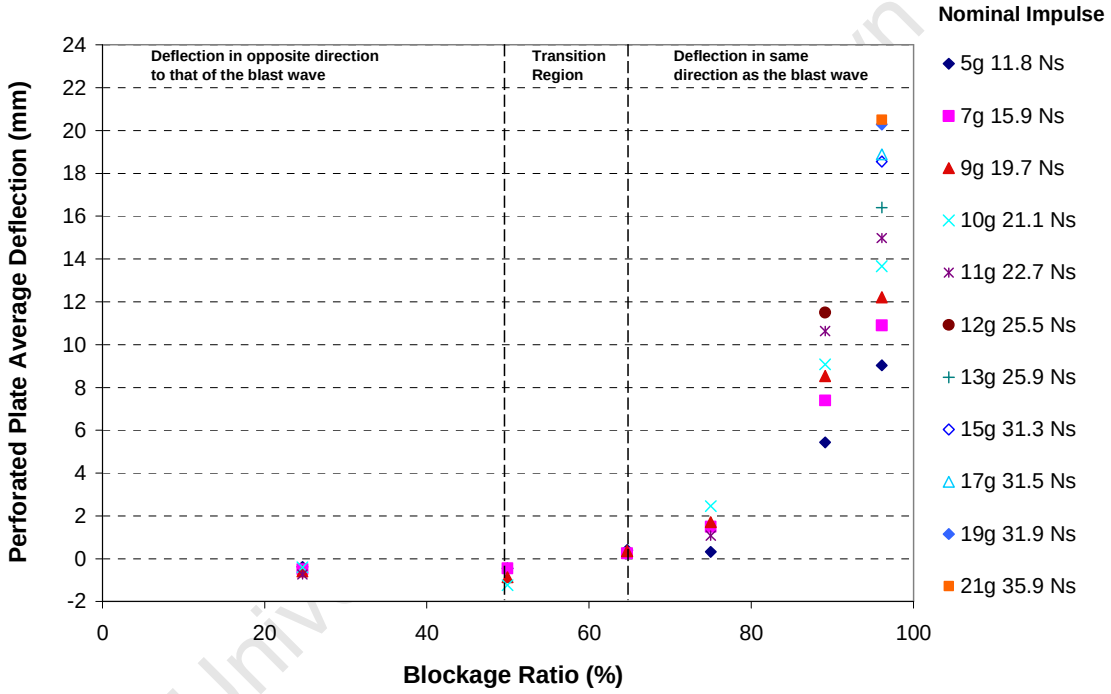

Figure 47: Graph of perforated plate average deflection versus blockage ratio

The following observations were made, from Figure 47:

- For blockage ratios of 25% and 50%, the perforated plate average deflections were in the opposite direction to that of the initial blast. An increase in blockage ratio from 25% to 50% for a given impulse had little or no effect on the perforated plate average deflection.

- For blockage ratios of 65% to 96%, the perforated plate average deflections were in the same direction as the initial blast. An increase in blockage ratio results in an increase in average deflection for all impulses except 11.8Ns, where an increase from 65% to 75% resulted in a decrease in average deflection.
- The transition from negative to positive average deflections occurs between blockage ratios of 50% and 65%.
- For blockage ratios less than 65% there is little spread in deflection for impulses between 11.8Ns and 21.1Ns. The plates are more sensitive to impulse at higher blockage ratios. This is expected, as increasing the blockage ratio increases the perforated plate arm length and hence the surface area over which the blast wave acts. The plate will also experience larger moments as the arm length increases.

A photograph of the cross-sections of the perforated plates for all blockage ratios at a nominal impulse of 19.7Ns is shown in Figure 48. The perforated plate deflection increased from 0.59mm to 0.87mm in the direction opposite to that of the initial blast, with an increase in blockage ratio from 25% to 50%. For a blockage ratio of 65% the deflection direction changes with the perforated plate deforming 0.35mm in the same direction as the initial blast. Any further increase in blockage ratio increases the average deflection of the perforated plate (in the direction of the initial blast) to 1.71mm, 8.53mm and 12.21mm for blockage ratios of 75%, 89% and 96% respectively.

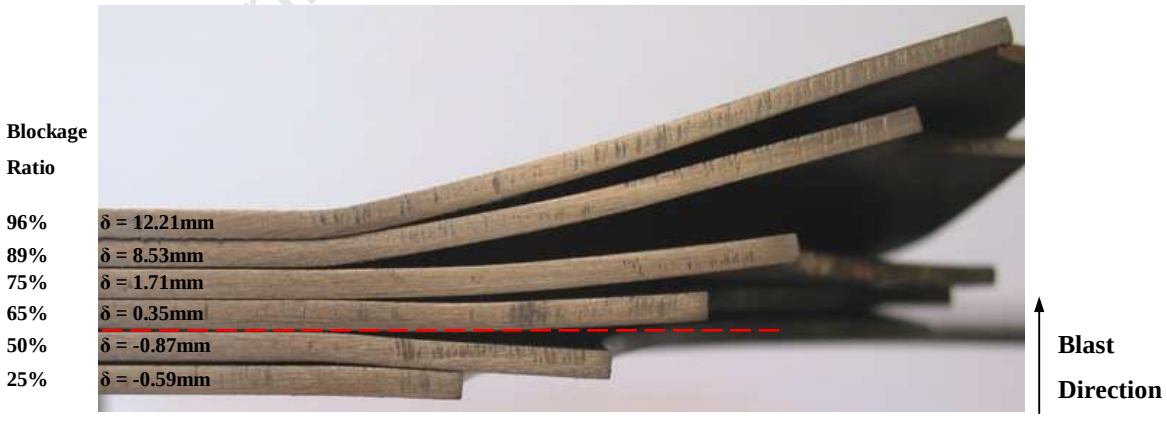

Figure 48: Photograph of the cross-sections of the perforated plates for all blockage ratios at a nominal impulse of 19.7Ns

5.5 Relationship between Blockage Ratio and the Impulse at Tearing of the Target Plate

A graph of impulse at tearing of the target plate versus blockage ratio is given in Figure 49. The red dashed line is the baseline impulse value of 31.81Ns, at which tearing of the target plate for the baseline blockage ratio of 0% occurred. A best-fit trend line is a second order polynomial given by the following equation:

$$I_t = 0.0042BR^2 - 0.432BR + 32.31 \quad (5.6)$$

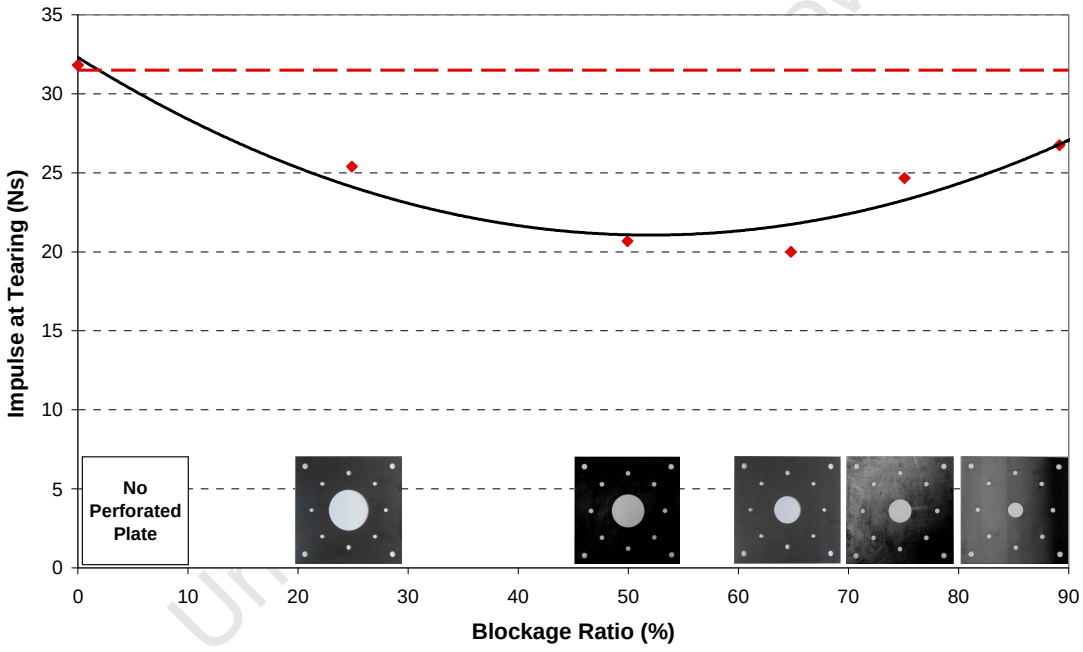

Figure 49: Graph of impulse at tearing versus blockage ratio

The graph shows a decrease in the impulse at tearing (I_t) with an increase in blockage ratio. The turning point occurs at a blockage ratio of 51% after which the impulse at tearing increases with any further increase in blockage ratio.

The turning point was calculated as follows:

$$\frac{dI_t}{dBR} = 0$$

$$\frac{dI_t}{dBR} = 0.0084BR - 0.432 = 0$$

$$BR = \frac{0.432}{0.0084} \approx 51\%$$

The only blockage ratio with an impulse at tearing greater than that of the baseline value is a blockage ratio of 96% with tests up to an impulse of 35.9Ns performed without tearing of the target plate.

5.6 Relationship between Blockage Ratio and Maximum Mid-point Deflection of the Target Plate before Tearing

A graph of maximum mid-point deflection of the target plate versus blockage ratio is shown in Figure 50.

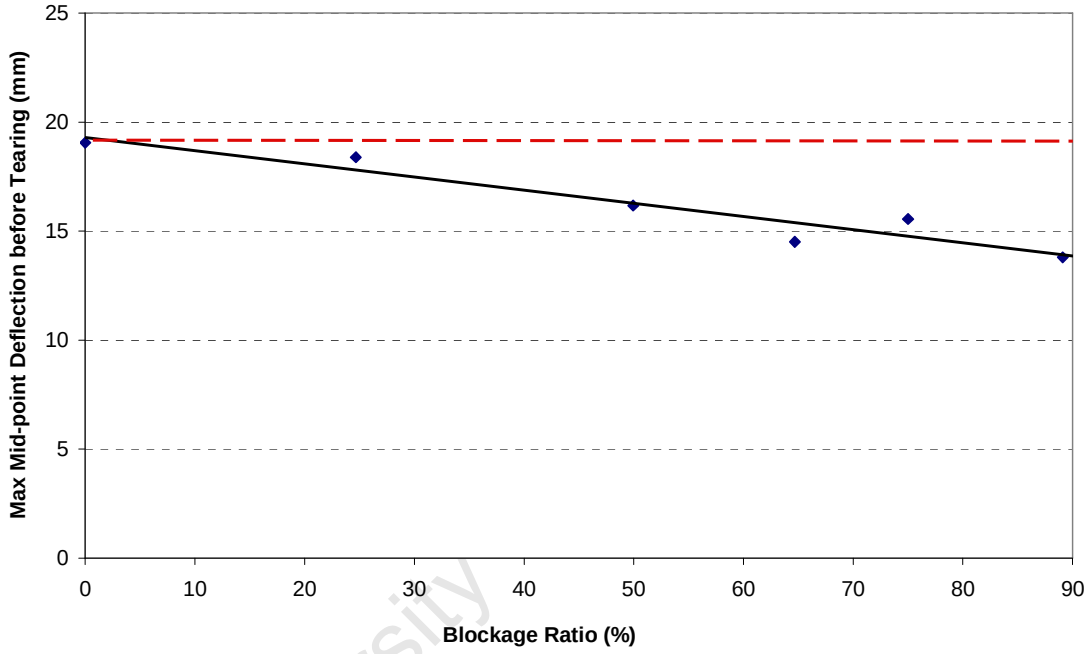

Figure 50: Graph of maximum mid-point deflection before tearing versus blockage ratio

The red dashed line indicates the maximum mid-point deflection before tearing of the target plate for the baseline blockage ratio of 0%. The linear trend line shows a decrease in the maximum mid-point deflection before tearing with an increase in blockage ratio. Possible reasons for this trend are the increase in the restriction of gas flow into the air gap between the plates with an increase in blockage ratio, and the effects of the blockage ratio on the specific impulse distribution across the target plate. The impulse distribution across the target plate was investigated using AUTODYN and is discussed in section 8.3 on page 134.

5.7 Effect of the Plastic Deformation Mechanism on the Performance of the Perforated Plates

In order to investigate which mechanism is most effective at providing protection to the target plate, namely the plastic deformation of the perforated plate or its load disruption capabilities, a second set of tests were performed for blockage ratios of 89% and 75% with the perforated plate thickness increased from 1.6 mm to 25 mm. This eliminated the plastic deformation mechanism of the panel. The graph of target plate mid-point deflection versus impulse is shown in Figure 51 for both blockage ratios.

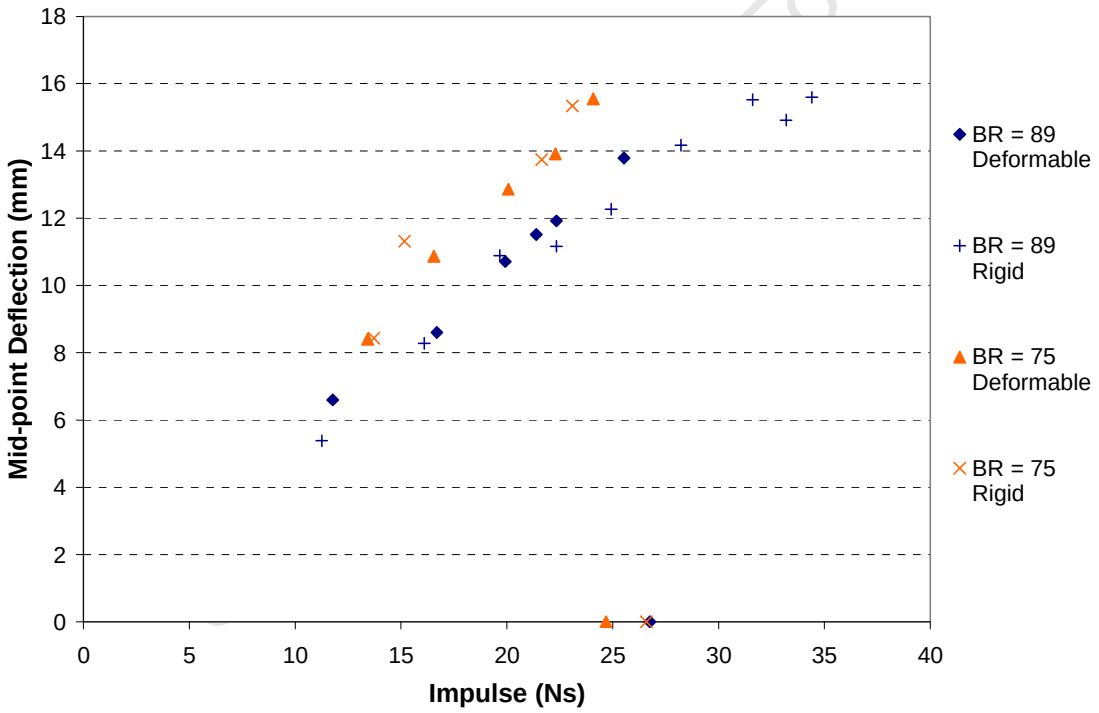

Figure 51: Graph of target plate mid-point deflection versus impulse for blockage ratios of 75% and 89% where both rigid and deformable perforated plates were used

The following observations were made, from Figure 51:

- Eliminating the plastic deformation mechanism of the perforated plate had no discernable influence on the mid-point deflection of the target plate for a given impulse.
- For a blockage ratio of 75% the mid-point deflections varied by less than 0.3 of a plate thickness.
- For a blockage ratio of 89% the mid-point deflections varied by less than 1 plate thickness.
- Eliminating the plastic deformation mechanism of the perforated plate increases the impulse at tearing for a given blockage ratio, resulting in a 7.7% increase for a blockage ratio of 75%.
- For a blockage ratio of 89% using deformable perforated plates, target plate tearing occurred at 26.75Ns. In tests with a rigid perforated plate the threshold impulse of the target plates was not reached. The target plates managed to withstand an impulse of 34.4Ns without tearing, 28.6% higher than the tests where deformable perforated plates were used.

Photographs of the cross-sections of the target plates for blockage ratios of 75% and 89%, for the rigid perforated plate configuration tests are shown in Figure 52 and Figure 53 respectively. Photographs of the cross-sections of the target plates for the deformable perforated plate configuration tests are shown in Figure 36 and Figure 37 on page 53, for blockage ratios of 75% and 89% respectively.

Figure 52: Photographs of the cross-sections of the target plates for a rigid perforated plate with blockage ratio of 75%

Figure 53: Photographs of the cross-sections of the target plates for a rigid perforated plate with blockage ratio of 89%

5.8 Effect of Separation Distance on the Test Plate Deflections

To investigate the effect of the separation distance on the test plate deflections, the closest comparable results, namely the results for blockage ratios of 75% and 89% with a separation distance of 25mm, were compared to the results for test set-up number three performed by Langdon et al [30] with a separation distance of 150mm and a blockage ratio of 82%. A comparison of the test set-ups is given Table 12.

Test Series	**BR %**	**SOD to PP mm**	**Separation mm**	**PP thickness mm**	**TP thickness mm**
Langdon et al [30] (-M B)	82	300	150	2	1.6
BR89D	89	300	25	1.6	1.6
BR75D	75	300	25	1.6	1.6

Table 12: Comparison of test set-up geometries

The closest comparable blockage ratios varied by 8.5%. The results in Figure 31 on page 51 and Figure 39 on page 54, show that both the target plate and perforated plate deflections are sensitive to blockage ratio. For this reason the influence of blockage ratio on the test plate deflections was also considered by including interpolated data points for a blockage ratio of 82%.

The perforated plates used by Langdon et al [30] were 0.4mm thicker. The results in Figure 51 on page 66 show that there is no sensitivity of mode I deflection magnitude for the target plates with a variation in perforated plate thickness. The difference in thickness was accounted for by dividing each plate deflection by its thickness.

5.8.1 Effect of Separation Distance on the Perforated Plate Deflection

The graph of perforated plate average deflection-thickness ratio (d/t) versus impulse is shown in Figure 54. Perforated plate data points where tearing of the target plate occurred, were not included. The red dashed line indicates the interpolated data points for the equivalent blockage ratio of 82% and a stand-off distance of 25mm.

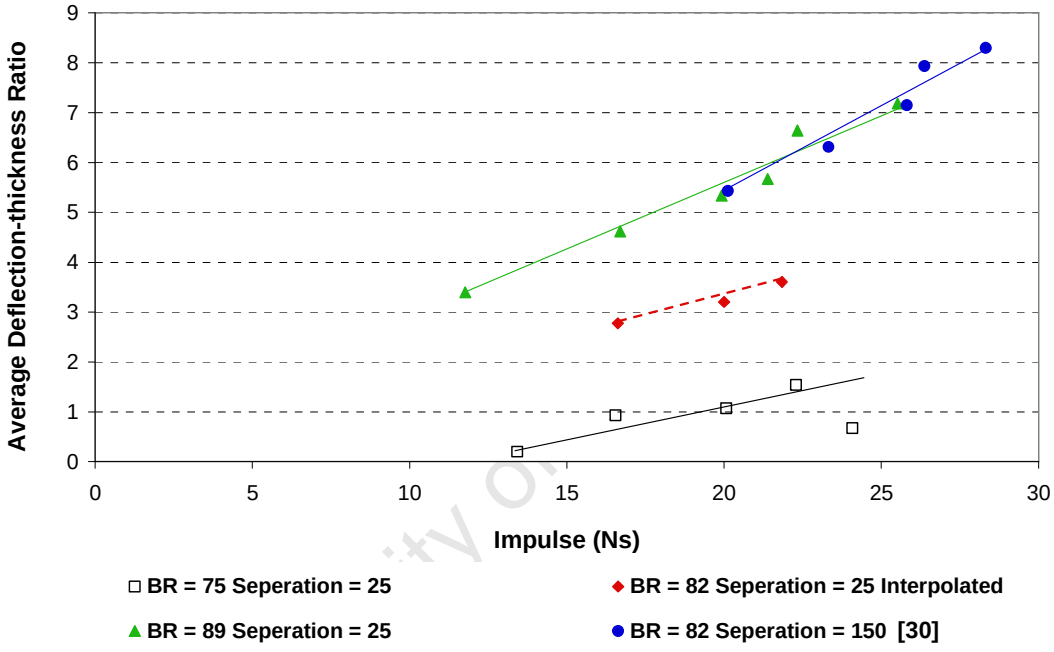

Figure 54: Graph of perforated plate average deflection-thickness ratio versus impulse for separation distances of 25mm and 150mm respectively

The perforated plate deflections from Langdon et al [30] for a blockage ratio of 82% and a separation of 150mm are very close to that of the current test series with a blockage ratio of 89% and a separation of 25mm. However, the red trend-line shows interpolated results for a blockage ratio of 82% and it is evident that the greater separation distance i.e. Langdon et al [30] resulted in higher perforated plate deflections. The attempt to eliminate the effect of the blockage ratio indicated an increase in the displacement of the perforated plates of 2.23 plate thicknesses with an increase in the separation distance for a nominal impulse of 20Ns as shown in Table 13.

A possible reason for the increase in the average deflection is that increasing the separation distance reduces the pressure build up between the plates, allowing the pressure build up on the front face of the perforated plate to cause larger deflections.

Impulse Ns	**Separation = 25 mm**			**Separation = 150 mm**
	BR = 75%	**BR = 82% (Interpolated)**	**BR = 89%**	**BR = 82%**
	d/t	**d/t**	**d/t**	**d/t**
20	1.07	3.20	5.33	5.43

Table 13: Comparison of perforated plate results for separation distances of 25mm and 150mm for a nominal impulse of 20Ns

5.8.2 Effect of Separation Distance on the Target Plate Deflection

The graph of target plate mid-point deflection-thickness ratio (d/t) versus impulse for the target plates for both separation distances is shown in Figure 55. The red dashed line indicates the interpolated data points for the equivalent blockage ratio of 82% and a stand-off distance of 25mm.

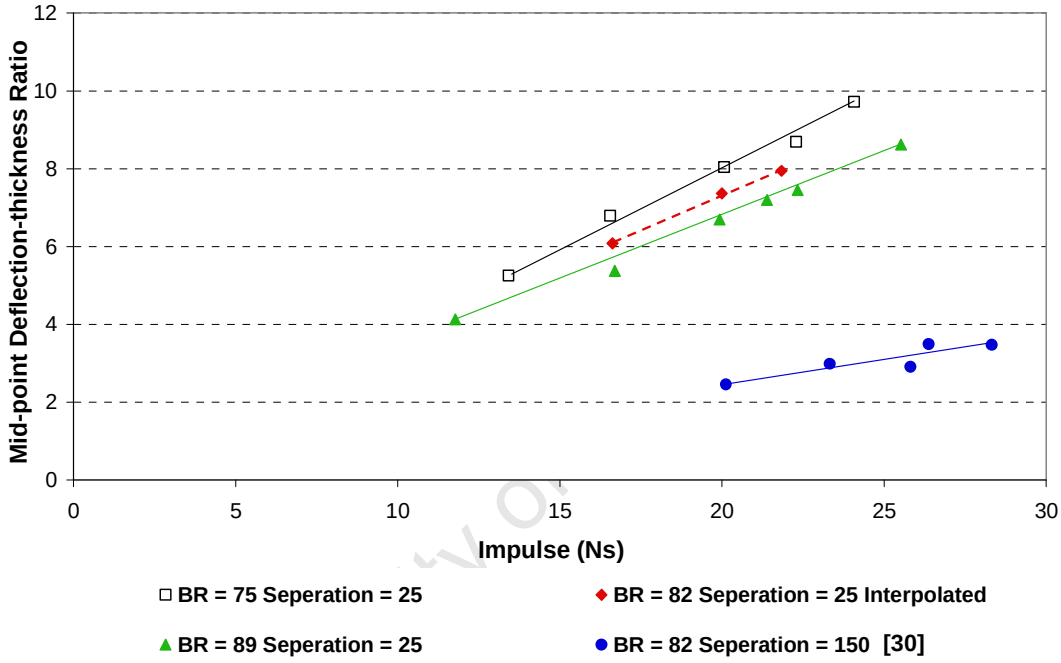

Figure 55: Graph of target plate mid-point deflection-thickness ratio versus impulse for a separation distance of 25 mm and 150 mm respectively

The target plate deflections from Langdon et al [30] for a blockage ratio of 82% and a separation of 150mm are significantly lower than that of the current test series for all blockage ratios, including the interpolated results for a blockage ratio of 82%. It is evident that the greater separation distance i.e. Langdon et al [30] resulted in lower target plate deflections. The attempt to eliminate the effect of the blockage ratio indicated a decrease in the displacement of the target plates of 4.91 plate thicknesses with an increase in the separation distance for a nominal impulse of 20Ns as shown in Table 14.

A possible reason for the decrease in the mid-point deflection is that increasing the separation distance once again reduces the pressure build up between the plates and hence the pressure acting on the target plate.

Impulse Ns	**Separation = 25 mm**			**Separation = 150 mm**
	BR = 75%	**BR = 82% (Interpolated)**	**BR = 89%**	**BR = 82%**
	d/t	**d/t**	**d/t**	**d/t**
20	8.04	7.37	6.69	2.46

Table 14: Comparison of target plate results for a separation distance of 25 and 150 mm

6. AUTODYN Computational Simulation

AUTODYN is an engineering software package specifically designed for solving non-linear dynamic problems using Lagrange, ALE, Euler and other mesh free solvers. [35]

6.1 Lagrange and Euler Solvers

The Lagrange solver is used for modelling solid continua while the Euler solver is generally used for the modelling of fluids and gases. Lagrange divides the structure up into blocks using interconnected nodes which move with the material as it deforms. Euler uses a grid fixed in space through which material can flow. The state of each block in the grid is determined from the state of the individual materials present in that block.

Governing equations such as the conservation of momentum, the conservation of mass and the conservation of energy, are used to set up partial differential equations which are then solved using the finite difference method in order to calculate the stresses and strains in the material at a given time.

6.2 Material Modelling

For isotropic materials the deformation can be split into two independent parts namely the Volumetric and Deviatoric stresses. Volumetric stresses are those associated directly with changes in the volume of a body without producing any distortion to the shape of the body and are governed by the equation of state. Deviatoric stresses are those associated directly with changes in shape and are calculated using the strength model. In addition to these, it is necessary to specify a failure criterion for solids, as materials can only sustain limited tensile stresses and strains.

6.2.1 Air Model

The air is modelled as an ideal gas with the ideal gas equation being the equation of state, which is most commonly written as:

$$PV = nR_gT \tag{6.1}$$

Alternatively the ideal gas law may be expressed as follows:

$$P = \rho_a(\gamma - 1)E_0 \tag{6.2}$$

Where ρ_a is the air density, γ is the ratio of specific heats namely C_p / C_v where C_v is the specific heat at constant volume, C_p is the specific heat at constant pressure and E_0 is the specific internal energy given by:

$$E_0 = C_vT \tag{6.3}$$

Where T is the temperature. The material properties of air are given in Table 15 and are obtained from the material library in AUTODYN [35].

Air, Equation of state – Ideal gas					
ρ_a (g/cm^3)	T (K)	C_p (kJ/kgK)	C_v (kJ/kgK)	γ	E_0 (kJ/kg)
1.225 x 10^{-3}	288.2	1.005	0.718	1.4	206.8

Table 15: Material properties for air used in the simulations, obtained from the material library in AUTODYN [35]

6.2.2 Detonation Model

The Jones-Wilkens-Lee equation of state, commonly known as JWL [36], is used to model the rapid expansion of high explosive detonation products. The initiation of the explosive is idealised as a detonation line moving cell by cell through the explosive. The pressure of the expanding gas is given by:

$$p = A\left(1-\frac{\omega\rho_p}{R_1\rho_e}\right)\exp\left(-R_1\frac{\rho_e}{\rho_p}\right)+B\left(1-\frac{\omega\rho_p}{R_2\rho_e}\right)\exp\left(-R_2\frac{\rho_e}{\rho_p}\right)+\omega\rho E_0 \tag{6.4}$$

Where A, B, R_1, R_2 and ω are empirically derived constants, ρ_e is the density of the explosive, ρ_p is the density of the explosive products and E_0 is the specific internal energy. The closest approximation to PE4 in the AUTODYN material library is C4. The material properties are given in Table 16 and are obtained from the material library in AUTODYN [35]. Once the explosive has been completely burned leaving behind gases at high temperature and pressure, AUTODYN will revert back to the ideal-gas equation of state for the remainder of the computation.

C4 Explosive, Equation of state - JWL								
ρ_e (g/cm^3)	**A (GPa)**	**B (GPa)**	**R_1**	**R_2**	**ω**	**CJ Detonation Velocity**	**CJ Energy/Volume (kJ/m^3)**	**CJ Pressure (MPa)**
1.601	609.8	12.96	4.5	1.4	0.25	8193	9.0 x 10^6	28.0

Table 16: Material properties for C4 used in the simulations, obtained from the material library in AUTODYN [35]

6.2.3 Solids Model

Equation of state

A linear equation of state was used for solids, determined by assuming the pressure is independent of the internal energy and that changes in the material density are small and reversible. The linear equation of state is given by

$$p(\rho) = K\mu \tag{6.5}$$

Where K is the bulk modulus and μ is the compression. [35]

Strength Model

The stress in the deforming material is given by equation (6.6). The strain hardening effect is modelled using power law hardening. Uni-Axial tensile tests provided the true stress-strain data from which the values of A, B and n where obtained from a best fit between the true stress-strain curve of the experimental data and the power law hardening curve. The strain rate effects on the material where modelled using the Cowper-Symonds [32] relation.

$$\sigma = (A + B\varepsilon^{n})\left(1 + \left(\frac{\dot{\varepsilon}}{D}\right)^{\frac{1}{q}}\right) \tag{6.6}$$

Power Law Hardening

Strain Rate Dependence

6.3 Detonation Mesh Refinement

To detonate the explosive, a volume of air is first created with the desired mesh density, then filled with the explosive and detonated. The detonation mesh is thus defined as the air mesh into which the explosive is placed and detonated. Increasing the number of blocks in the air in turn increases the number of blocks through the thickness of the explosive and hence the detonation mesh density.

6.3.1 The Effect of Detonation Mesh Density on the Simulated Pressure of the Explosive

The detonation properties such as pressure, density and temperature of the detonation products, are often characterised as the Chapman-Jouguet (CJ) values of the explosive [37]. These values represent the corresponding maximums of the variables in the detonation products for **confined** detonation and may not be achieved in the detonation of an **unconfined explosive** [38].

The C-J pressure of C4 is approximately 28 MPa. Several different mesh sizes were modelled in order to evaluate the effect of the detonation mesh density on achieving the CJ pressure of the explosive. An axis-symmetric model was used, consisting of a 100mm x 50mm air block, shown in Figure 56, filled with 5 grams of C4 explosive.

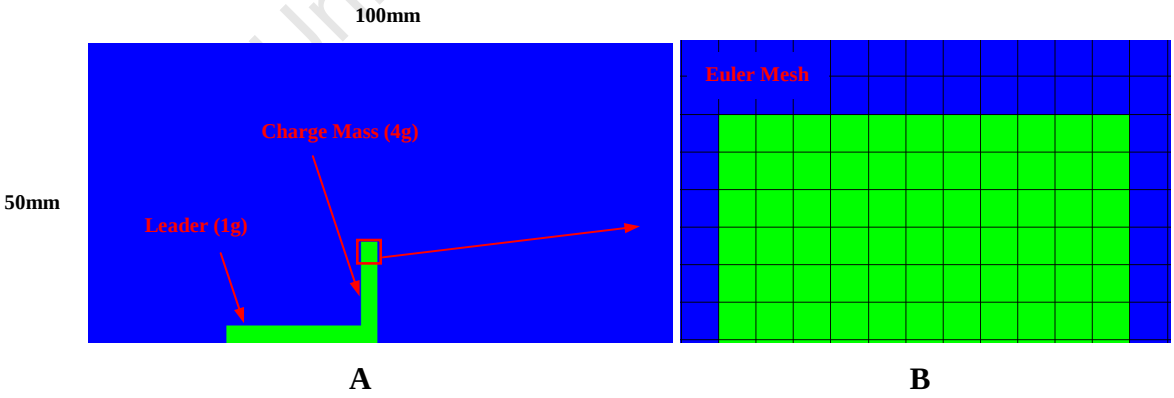

Figure 56: Detonation mesh refinement model (A) and zoomed view of explosive mesh (B)

The mesh sizes that were investigated along with the maximum pressure achieved during detonation are presented in Table 17, with all mesh labelling in an i x j notation as follows:

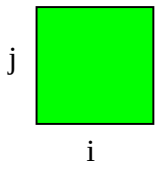

Detonation Mesh No.	Detonation Mesh Size (mm)	Max Detonation Pressure Achieved (MPa)
1	1 x 1	13.44
2	0.5 x 0.5	19.02
3	0.25 x 0.25	22.32
4	0.1 x 0.1	25.42

Table 17: Detonation mesh sizes and maximum pressures achieved

A typical pressure distribution through the explosive during detonation is shown in Figure 57. Mesh 4 gave the closest value to that of the theoretical CJ value, achieving a maximum detonation pressure of 25.42MPa. Further detonation mesh refinement was not possible, with smaller mesh sizes failing to run. The maximum detonation pressure of C4 for unconfined detonation was therefore taken as 25.42MPa. This is 9.21% lower than that of the CJ pressure, which was considered acceptable since the unconfined nature of the detonation would give CJ pressures lower than 28MPa.

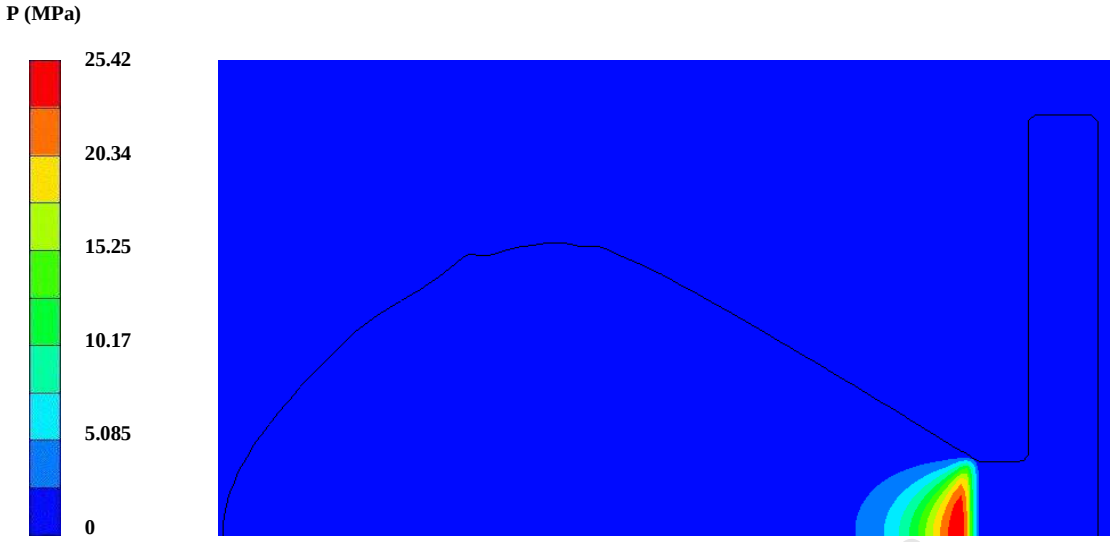

Figure 57: Pressure distribution through the explosive during detonation for mesh size 4 at 2.4μs

The computation time for mesh 4 was approximately an hour and a half; six times that of mesh 3 with a computation time of 15 minutes, on a SUN computer with 2.6GHz Dual-Core AMD Opteron processor and 2G RAM. Further investigation was done on these two mesh sizes to determine the effects of the detonation mesh density on the calculated impulse and whether or not the coarser mesh could be used in order to save computation time.

6.3.2 The Effect of Detonation Mesh Density on Impulse

To investigate the effects of the detonation mesh density on the resulting impulse, the pressure-time history was recorded at several gauge points at the right hand boundary of the model as shown in Figure 58, for a 5 gram charge mass for both detonation mesh 3 and 4. The pressure-time history was recorded for a load-duration of approximately 38μs (time taken from the arrival of the blast wave at the right hand boundary), the integral of which gave the specific impulse at each gauge point.

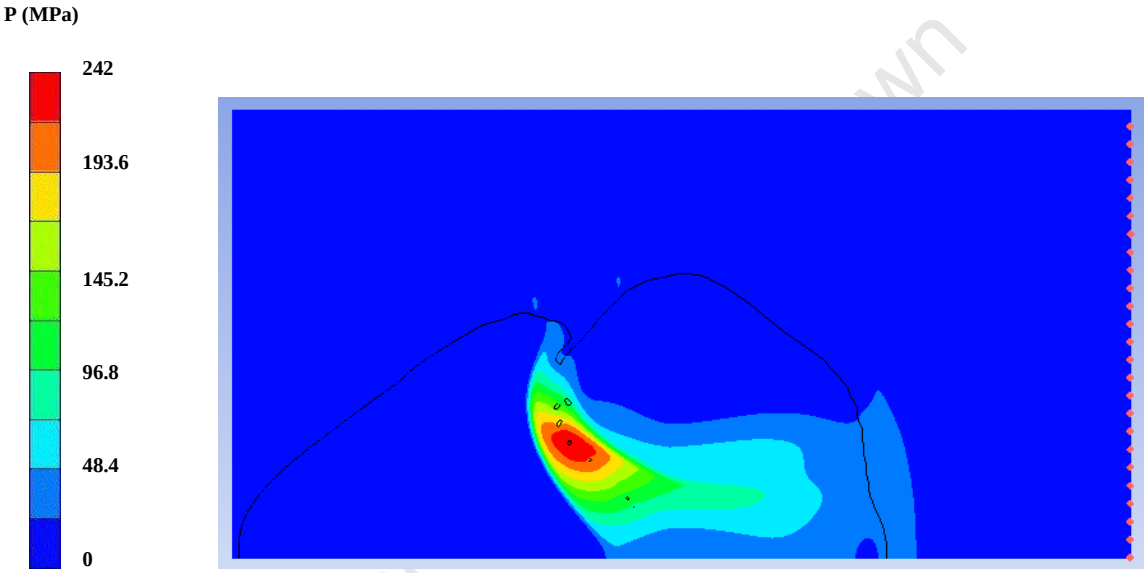

Figure 58: AUTODYN model for mesh 3, at 7.1μs, used to investigate the effects of the detonation mesh on the impulse measured at the boundary

The impulse was then calculated by multiplying the specific impulse value at each gauge point by the area over which the impulse acted. The results for both mesh sizes are presented in Table 18.

Detonation Mesh No.	Detonation Mesh Size (mm)	Impulse (Ns)	Load Duration (μs)
3	0.25 x 0.25	7.48	37
4	0.1 x 0.1	8.08	38

Table 18: Comparison of impulses measured at the boundary for various detonation mesh sizes

The impulse measured at the boundary varied by 8% depending on the detonation mesh size. However it was not clear as to whether this difference in impulse was due to the detonation mesh density or the air mesh density in which the pressure-time history was recorded. For this reason the 5 gram charge was first detonated in mesh number 4 then mapped (state variables are transferred from one mesh size to another) onto an air mesh 0.25mm x 0.25mm (equivalent to detonation mesh size 3) for the remainder of the simulation. The results of the simulation are presented in Table 19.

Detonation Mesh No.	Detonation Mesh Size (mm)	Air Mesh Size (mm)	Impulse (Ns)	Load Duration (μs)
3	0.25 x 0.25	0.25 x 0.25	7.48	37
4	0.1 x 0.1	0.1 x 0.1	8.08	38
4	0.1 x 0.1	0.25 x 0.25	8.03	37

Table 19: Comparison of impulses measured at the boundary for various air mesh sizes in which the pressure-time history was recorded

From the simulation it was clear that the detonation mesh density is the dominant factor. The variation in air mesh density in which the pressure-time history was recorded had less than 1% effect on the final impulse. The results however were for a small scale simulation, 100mm by 50mm in dimension. The pressure wave travelled only 50mm down the tube before coming into contact with the boundary at which the impulse was calculated for a load-duration of approximately 38μs.

The final model was approximately 500mm by 53mm in dimension, over 5 times larger. The pressure wave travelled 300mm down the tube before coming into contact with the boundary, at which the impulse was calculated for a load-duration of approximately 1.3ms in comparison to the 38μs. It thus had to be investigated as to how much of a factor the detonation mesh density was, 300mm down the tube for an impulse calculated over a time-duration nearly 35 times longer.

The computation time for the small scale model was between 6 and 12 hours. For a larger model an air mesh size of 0.1mm x 0.1mm or 0.25mm x 0.25mm would be computationally too expensive. The small scale models showed that coarsening the air mesh reduced the computation time, with less than 1% effect on the final impulse. In order to reduce the computation time of the larger model the explosive was first detonated in mesh size three and four, and then mapped onto a coarser air mesh for the rest of the simulations.

The state variables for both detonation mesh sizes were mapped onto a model 400mm x 53mm in dimension with an air mesh size of 0.5mm x 0.5mm. The simulations were run for a time-duration of approximately 1.5ms allowing the pressure wave to travel 300mm down the tube, to where it first came into contact with the plates. The impulse was then calculated at the right hand boundary for a load-duration of approximately 1.34ms, in the same manner as before. The results are presented in Table 20.

Detonation Mesh No.	Detonation Mesh Size (mm)	Air Mesh Size (mm)	Impulse (Ns)	Load Duration (ms)
3	0.25 x 0.25	0.5 x 0.5	11.91	1.341
4	0.1 x 0.1	0.5 x 0.5	12.08	1.346

Table 20: Comparison of impulses measured at the boundary 300 mm away from the point of detonation for various detonation meshes

The results show that for a larger model the dependence of the final impulse on the detonation mesh reduces significantly, with a difference in impulse of less than 1.5%. From this investigation **a mesh size of 0.25mm x 0.25mm was used for the detonation** of all charge masses in order to reduce the computation time.

6.4 Air Mesh Refinement

From the refinement of the detonation mesh it was found that the optimum detonation mesh size was 0.25mm x 0.25mm. The detonation mesh refinement also revealed that for large scale models an air mesh of 0.25mm x 0.25mm or 0.1mm x 0.1mm became computationally expensive. To shorten the computation time, the detonation was first modelled with a fine detonation mesh (0.25mm x 0.25mm) for all charge masses until the explosive had achieved its highest pressure (namely 22.32 MPa) at which point it was then mapped onto a coarser air mesh. At this point the equation of state was the ideal gas equation.

Three air mesh sizes were investigated, in which both the mesh size and aspect ratio were varied. The results of the simulations are presented in Table 21.

Detonation Mesh Size (mm)	Air Mesh Size (mm)	Impulse (Ns)	Load Duration (ms)
0.25 x 0.25	0.25 x 0.25	12	1.34
0.25 x 0.25	0.5 x 0.25	11.86	1.34
0.25 x 0.25	0.5 x 0.5	11.91	1.34

Table 21: Comparison of impulses measured at the boundary for various air mesh sizes

The results show that for a detonation mesh of 0.25mm x 0.25mm, coarsening the air mesh had less than a 1.2 % effect on the final impulse measured at the boundary. The effect of the mesh size aspect ratio was investigated by choosing one of the aspect ratios as 2:1 instead of 1:1. This had little effect on the impulse; however a difference in the blast wave profile was noted. Pressure contour plots (t = 90.9µs) simulated using AUTODYN are shown in Figure 59, Figure 60 and Figure 61 for an air mesh size of 0.5mm x 0.25mm, 0.25mm x 0.25mm and 0.5mm x 0.5mm respectively. The dashed lines indicate the axis of symmetry about the centre of the cylindrical tube. The mesh aspect ratios are illustrated in the top left hand corner of each figure.

The pressure contour plots show a variation in pressure of less than 6% with a variation in the air mesh size. There was however a distinct difference in the pressure profiles with a variation in aspect ratio. Doubling the length of the cell resulted in a bulging of the blast wave profile toward the axis of symmetry, as shown in Figure 59.

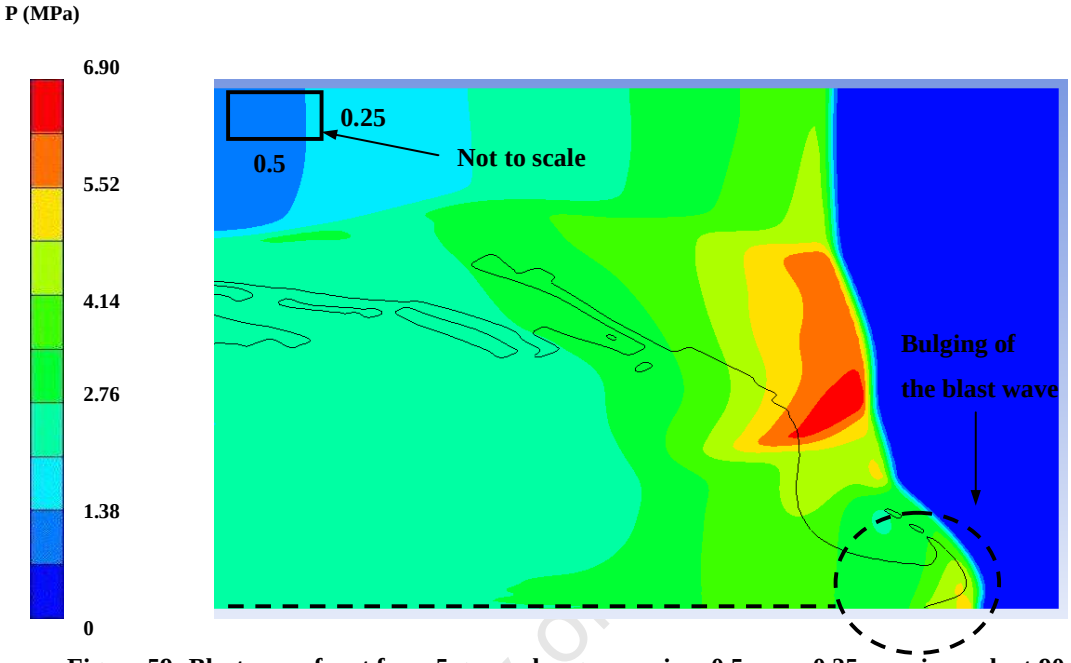

Figure 59: Blast wave front for a 5 gram charge mass in a 0.5mm x 0.25mm air mesh at 90.9 µs

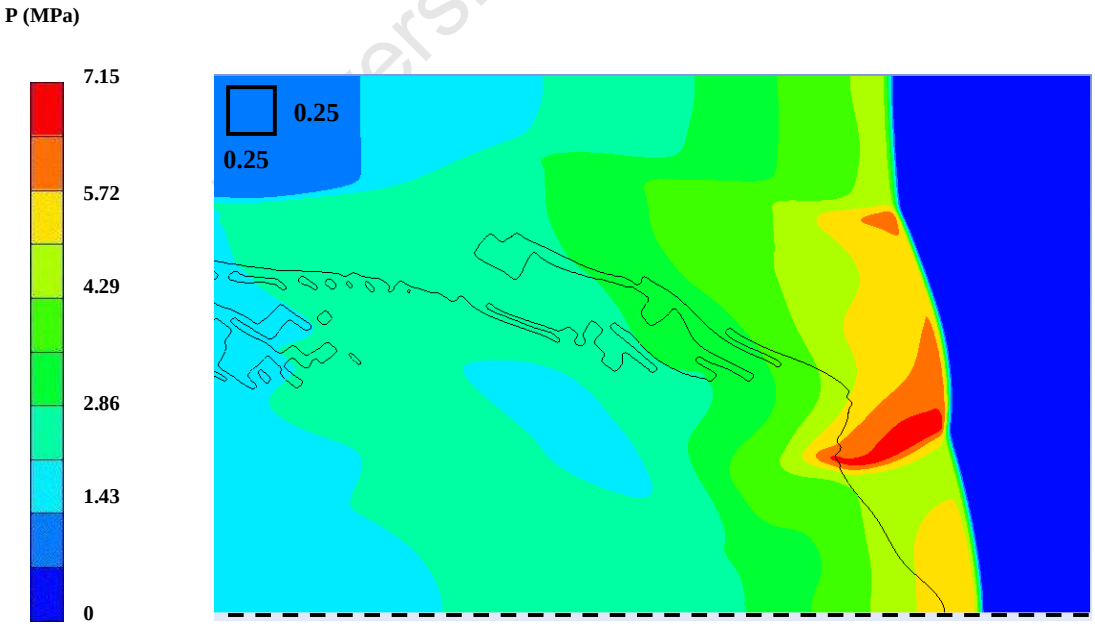

Figure 60: Blast wave front for a 5 gram charge mass in a 0.25mm x 0.25mm air mesh at 90.9 µs

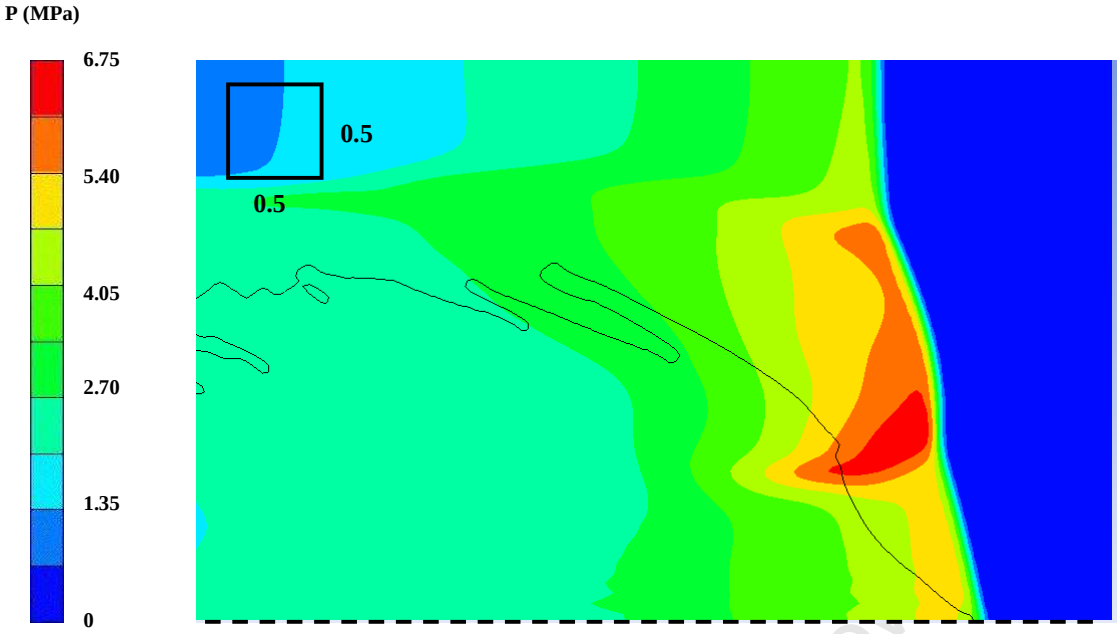

Figure 61: Blast wave front for a 5 gram charge mass in a 0.5mm x 0.5mm air mesh at 90.9 µs

6.5 Test Plate Mesh Refinement

A parameter study was performed in order to investigate the effect of the through thickness mesh size on the deformation profile of the plate. The model used for the test plate mesh refinement is shown in Figure 62. The model consisted of a 100mm x 50mm air block with a mesh size of 0.25mm x 0.25mm filled with 5 grams of explosive. A mild steel test plate 1.6mm x 50mm was introduced into the model. The plate mesh sizes that were investigated are listed in Table 22.

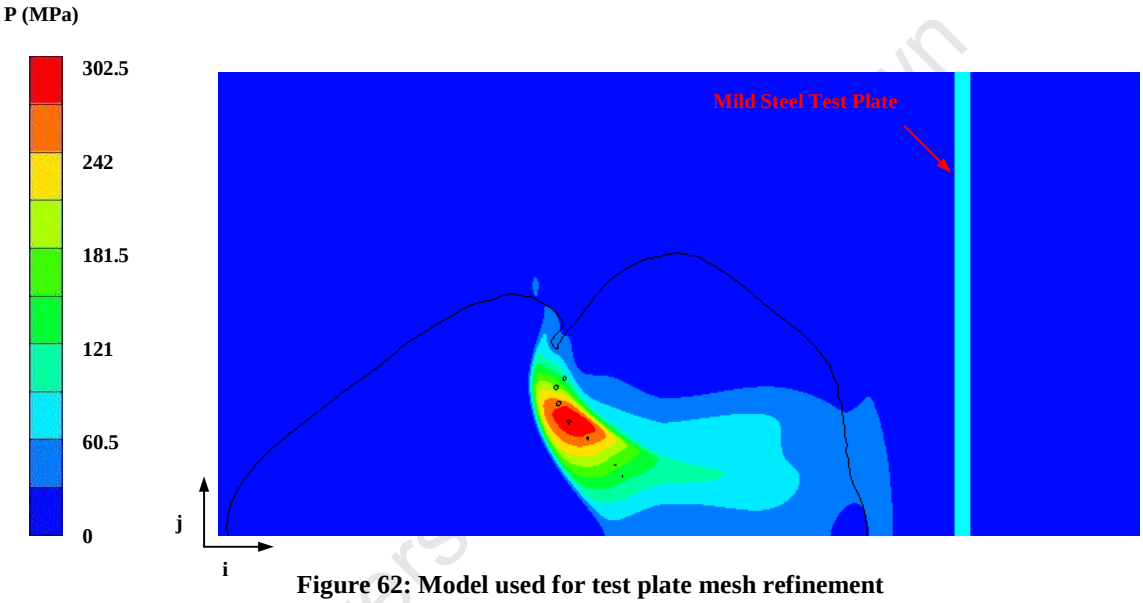

Figure 62: Model used for test plate mesh refinement

Mesh No.	No. of blocks through the		Mesh Size (mm)
	Thickness	Length	
1	2	94	0.8 x 0.53
2	3	94	0.53 x 0.53
3	4	94	0.4 x 0.53
4	5	94	0.32 x 0.53
5	6	94	0.26 x 0.53
6	7	94	0.23 x 0.53

Table 22: Comparison of test plate mesh sizes

Gauges were placed along the length of the plate in order to measure the plate deflection and obtain a final deformation-profile. The gauges were positioned 4 cells apart, starting halfway through the first cell as shown in Figure 63.

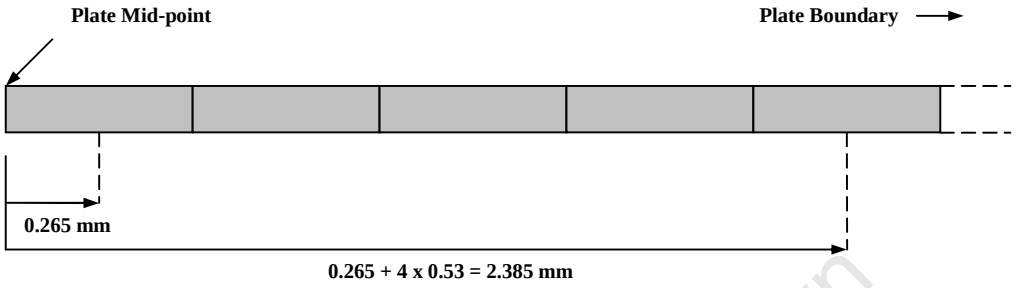

Figure 63: Diagram indicating the gauge placement along the target plate

The models for both mesh number one and five failed, with AUTODYN indicating that the time step was too small and hence no solution could be found. Final deflection profiles were plotted in Excel for the remaining mesh sizes, as shown in Figure 64, at a constant time interval of 182.3μs.

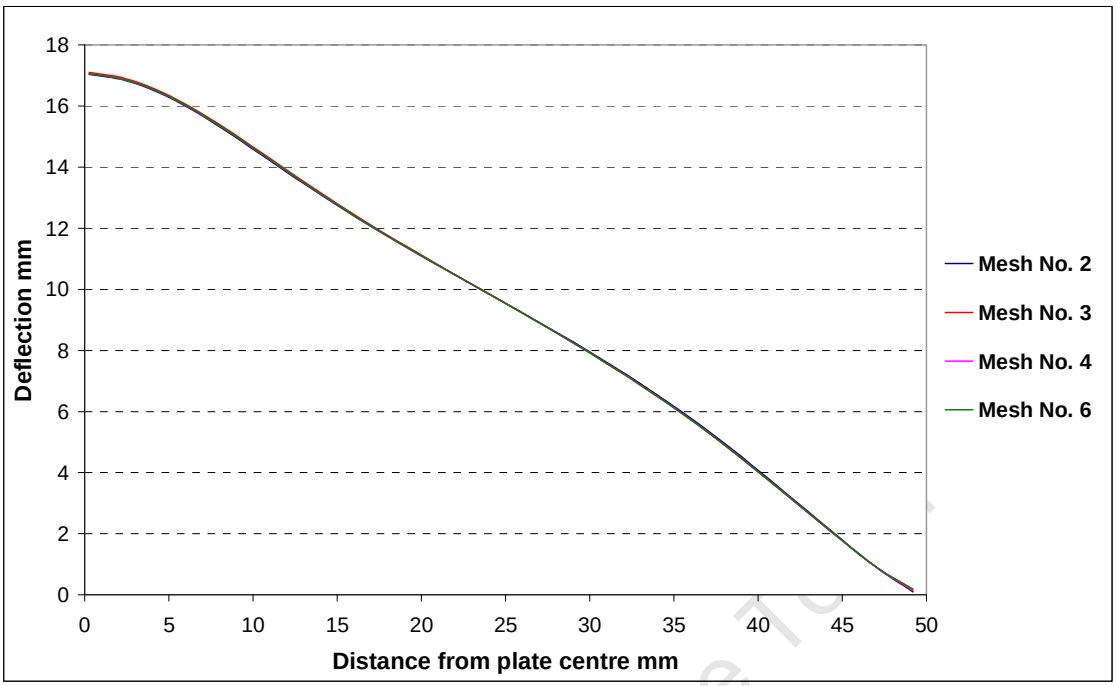

Figure 64: Comparison of final deflection profiles for various target plate mesh sizes

Varying the target plate mesh size had no significant effect on the deformation profile of the plate however the investigation did eliminate mesh numbers one and five. The final chosen mesh size depended on the interaction between the mesh of the Euler and Lagrange components in the model. It is required that the Euler mesh of the air be finer than the Lagrange mesh in the plate. Therefore the finer the plate mesh, the finer the air mesh and the more computationally expensive the model becomes. The **chosen air mesh size is 0.5mm x 0.5mm** and therefore in order to keep the plate mesh larger than the air mesh without changing the air mesh, **plate mesh number two was chosen**.

6.6 Final AUTODYN Model

6.6.1 Deflection Model Dimensions

An axi-symmetric model was used to calculate the target plate and perforated plate deflections, which consisted of an air block 500mm x 53mm, as shown in Figure 65. The dashed red line indicates the axis of symmetry whilst the solid red lines indicate where outflow boundaries have been specified, allowing both gas and C4 products to escape. The dashed black lines indicate the front and back ends of the cylindrical blast tube; no boundary condition was specified along the length of the tube as the default boundary condition in AUTODYN is a reflective boundary simulating the tube wall.

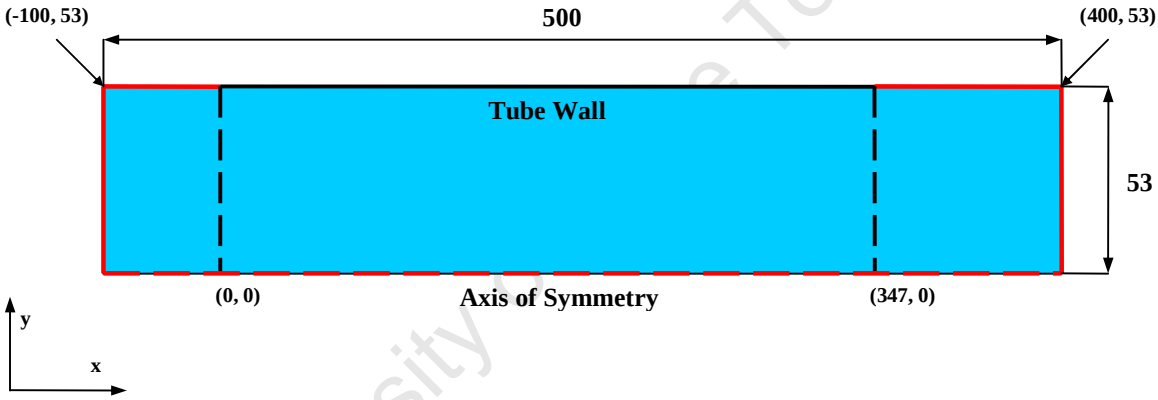

Figure 65: Axis-symmetric model used for calculating the test plate deflections

The test plates were inserted in their relative positions as shown in Figure 66 for blockage ratios of 0% and 96%. The plate was extended beyond the boundary of the blast tube by 25.44mm to enable boundary conditions to be applied, simulating the clamping of the plates. Two boundary conditions were specified for the plates indicated by the solid red lines labelled (A) and (B) in Figure 66 and Figure 67. A zero-y velocity boundary condition was specified at the top edge of each plate labelled (A), and a zero-x velocity boundary condition was specified along the right edge of the extended section of each plate labelled (B).

These two conditions maintained the relative position of the plate whilst still allowing the material at the left hand boundary of the extended section, indicated by the blue line labelled (C) in Figure 67, to flow plastically as the plate deformed.

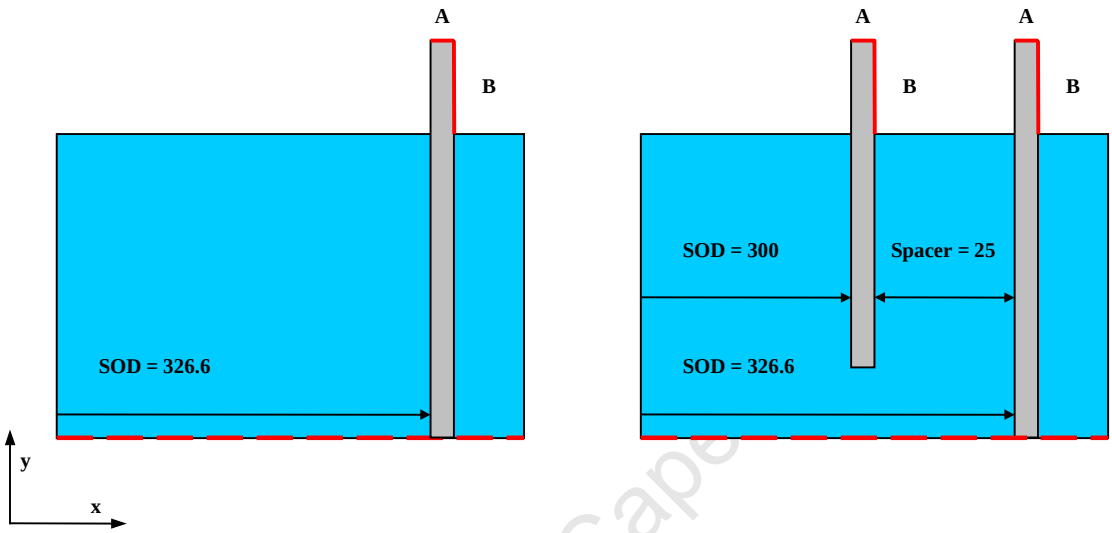

Figure 66: Diagram indicating test plate positioning

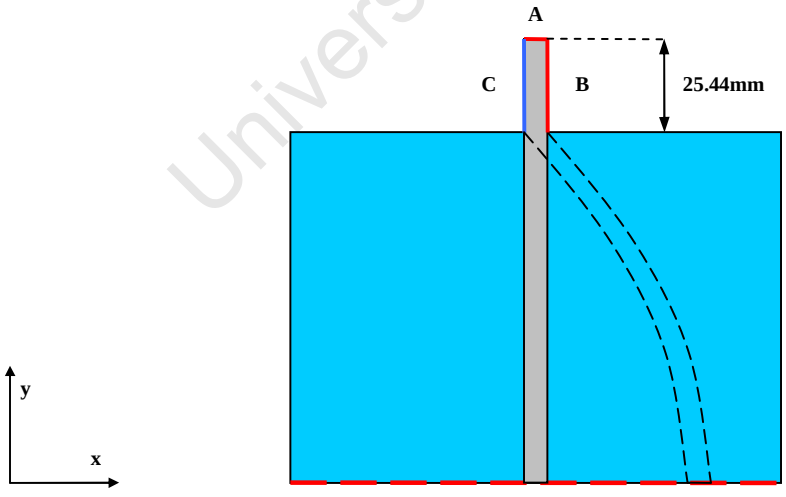

Figure 67: Diagram indicating test plate boundary conditions marked in red

6.6.2 Impulse Model Dimensions

In order to estimate the impulse measured by the pendulum using AUTODYN, the pressure acting on the surface of the plates needed to be recorded for the full load duration, from initial pressure rise back to atmospheric. During this time the test plates deform. There is however, no option in AUTODYN allowing gauges to be attached to the surface of the plate in order for them to move with the plate as it deforms. Three different methods of estimating the pressure acting on the surface of the plate using AUTODYN were investigated, for a blockage ratio of 0% with a 5 gram charge mass:

1. The plate was allowed to deform and the pressure was recorded at the original position of the plate as the blast wave passed, as shown in Figure 68A.
2. The plate was fixed by applying a zero velocity boundary to one of the plate faces, and the pressure recorded on the surface of the rigid plate, as shown in Figure 68B.
3. The plate was eliminated entirely and a reflective boundary condition applied at the right hand boundary where the plate would have been, as shown in Figure 68C. This eliminated the interaction between the Lagrange and Euler components and thus reduced the computation time.

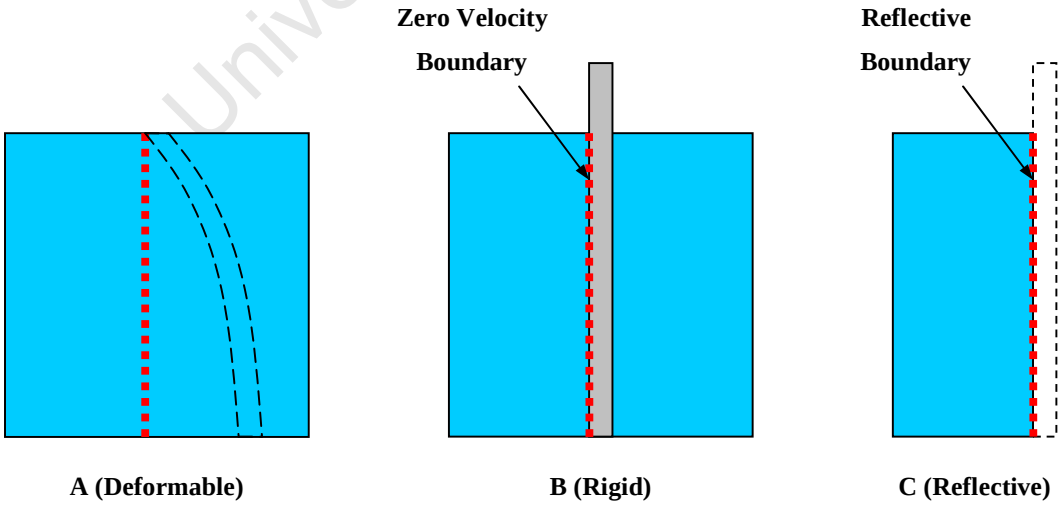

Figure 68: Possible gauge positioning for calculating impulse acting on the target plate

The gauges were placed in the air blocks immediately in front of the target plate and spaced 2mm apart starting at the axis of symmetry to the tube boundary as shown in Figure 69.

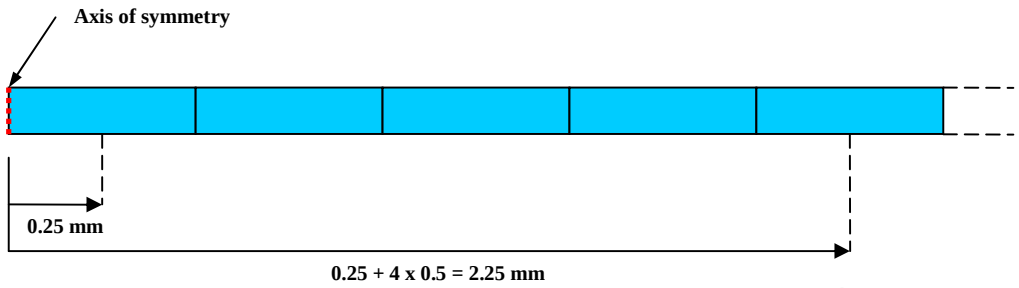

Figure 69: Diagram indicating the gauge placement in the air along the length of the target plate

The results are presented in Table 23, and show a difference in impulse from the experimental result of approximately -2.7%, -0.7% and -0.25% for the deformable, rigid and reflective methods respectively.

Method No.	Impulse Ns	Load Duration ms
Experimental Result	12.14	
1. Deformable	11.81	1.3
2. Rigid	12.05	1.2
3. Reflective	12.08	1.3

Table 23: Comparison of impulses calculated using the rigid method, with and without a target plate and at the original position of a deformable target plate

Method three was therefore used for all impulse calculations as it gave the closest estimate of the impulse measured by the pendulum, and significantly reduced the computation time by eliminating the interaction between the Lagrange and Euler components. The model used for calculating the impulse for all tests with a blockage ratio of 0% is shown in Figure 70. The red dotted line indicates the position of the gauges.

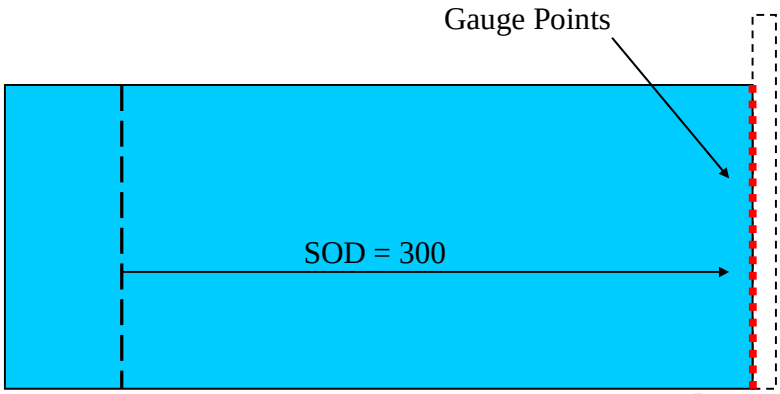

Figure 70: Model used for calculating impulses for a blockage ratio of 0%

For all other blockage ratios a similar method was applied to calculate the impulse. A void was left in place of the perforated plate and additional reflective boundaries indicated by the solid red line in Figure 71 were assigned along the arm length (L_a) of the perforated plate. The dotted red lines indicate the position of the gauges.

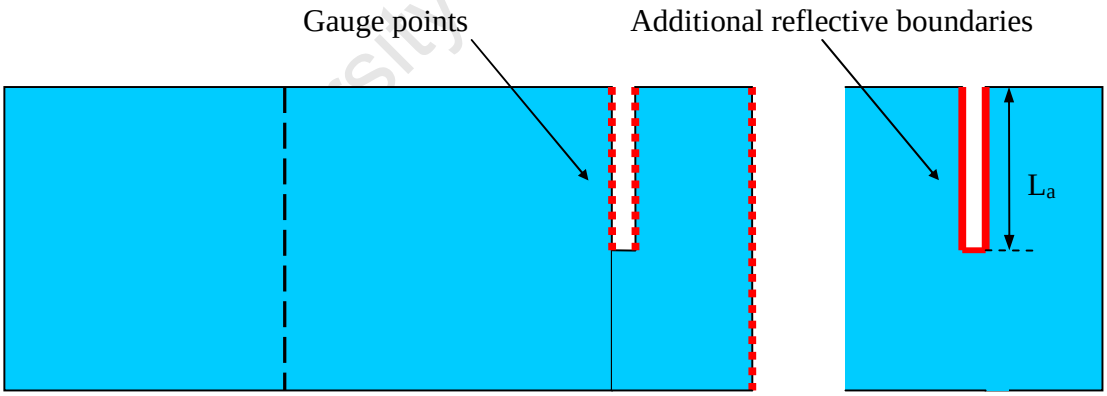

Figure 71: Model used for calculating the impulses for blockage ratios of 25 to 96%

The numerically predicted impulse imparted to the pendulum (I_{PEND}) is calculated as follows:

$$I_{PEND} = I_{TF} + I_{PF} - I_{PB} \tag{6.7}$$

Where:

- I_{TF} is the impulse imparted to the front face of the target plate over the full load duration.
- I_{PF} is the impulse imparted to the front face of the perforated plate over the full load duration
- I_{PB} is the impulse imparted to the back face of the perforated plate over the full load duration.

The direction in which each impulse acts is illustrated in Figure 72.

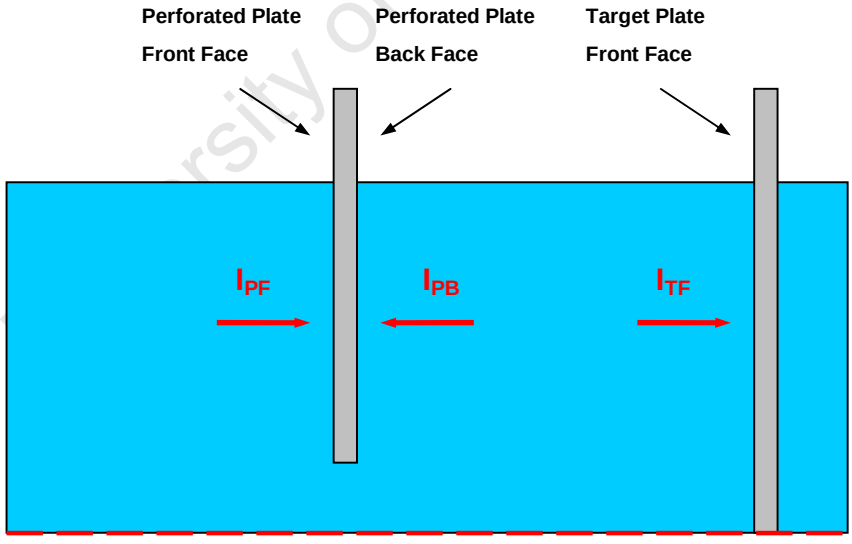

Figure 72: Diagram illustrating impulse directions

6.6.3 Final AUTODYN Model Mesh Sizes

The mesh sizes for the final model are summarised in Table 24.

Part		Mesh Size (mm)	Number of blocks for the perforated plate	
			i-direction	j-direction
Detonation		0.25 x 0.25	100	100
Air		0.5 x 0.5	1000	106
Target Plate		0.53 x 0.53	3	148
Perforated Plates:				
∅ (mm)	BR			
21	96	0.53 x 0.53	3	128
35	89	0.53 x 0.53	3	115
53	75	0.53 x 0.53	3	98
63	65	0.53 x 0.53	3	88
75	50	0.53 x 0.53	3	77
92	25	0.53 x 0.53	3	61

Table 24: Mesh sizes used in the final model

The number of blocks along each perforated plate length was calculated by adding the perforated plate arm length (L_a) to the length of the extended section (25.44mm), dividing by the block length (0.53mm) and rounding off to the nearest block.

7. Computational Results

7.1 Test Plate Deflection and Response Time

In order to calculate the deflections of both the target plate and perforated plate the model was run until the plates reached equilibrium. The target plate deflection-time history for a blockage ratio of 0% at an impulse of 20.9Ns is given in Figure 73 for nine out of twenty five points along the plate profile from the centre to the boundary. The points along the profile of the plate reach equilibrium at approximately 275µs in this case, relative to detonation at 0µs.

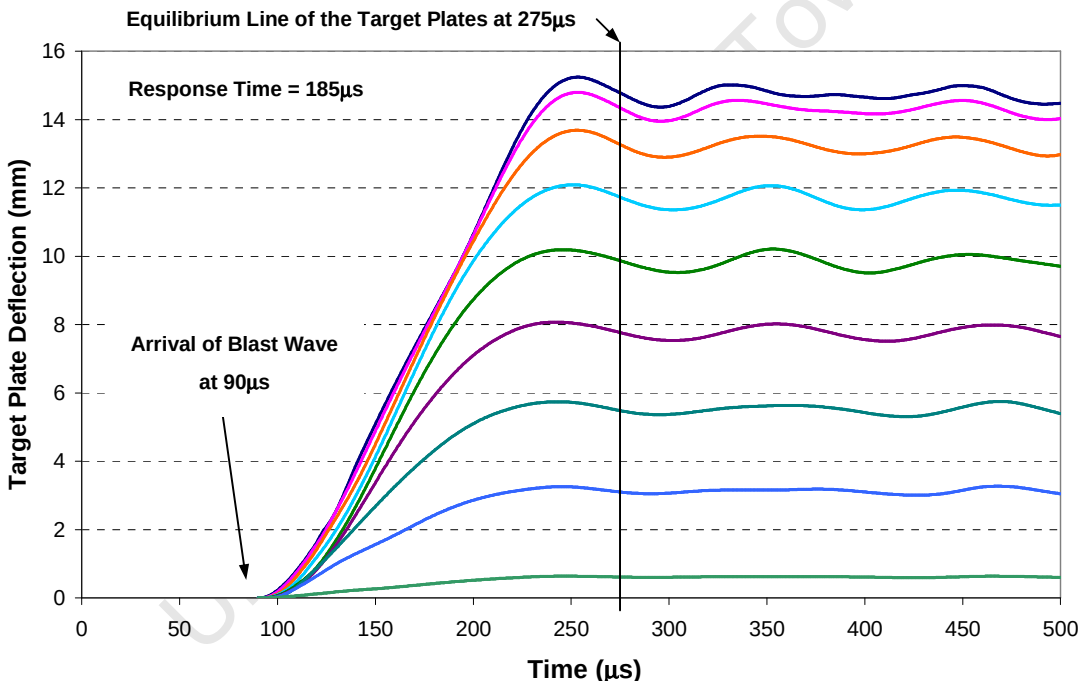

Figure 73: Graph of the deflection-time history along the target plate profile for a blockage ratio of 0% at an impulse of 20.9Ns

The response time of the target plates was taken as the time interval from the arrival of the blast wave at the target plate surface to equilibrium. An increase in the impulse resulted in a decrease in the response time of the target plates.

7.2 Test Plate Profile Comparison

The target plate and perforated plate profiles were traced and digitised. The profiles of the test plates for a 9 gram charge mass were plotted in excel and compared to the computational profiles for all blockage ratios. The profiles across charge masses of 5, 9 and 11 grams were also compared for a blockage ratio of 89%.

7.2.1 Target Plate Profile Comparison

Cross-sections of the computational and experimental target plates for a 9 gram charge mass are shown in Figure 74 for a blockage ratio of 89%. Both target plates exhibited a large global dome typical of uniform loading.

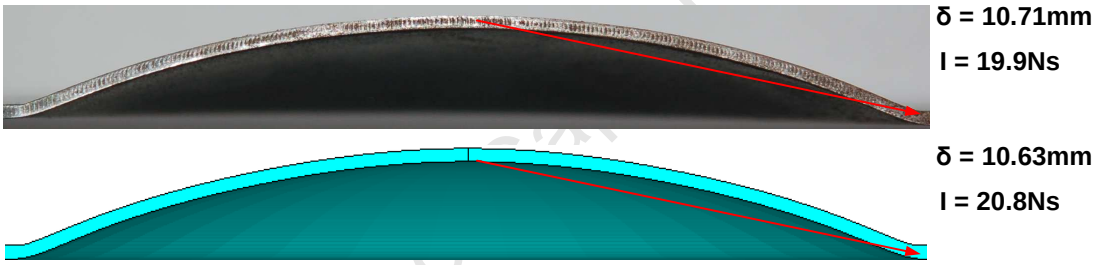

Figure 74: Target plate cross-sections for a 9 gram charge mass and a blockage ratio of 89%

The experimental and computational target plate profiles for several blockage ratios (namely 0%, 50%, 89% and 96%) are shown in Figure 75, for a 9 gram charge mass. The target plate profiles for several charge masses (namely 5, 9 and 11 grams) are shown in Figure 76, for a blockage of 89%. The target plate profiles show good correlation, with variations in deflection of less than 1 plate thickness. The target plate profiles for a 9 gram charge mass for blockage ratios of 25%, 65% and 75% are shown in Appendix C.

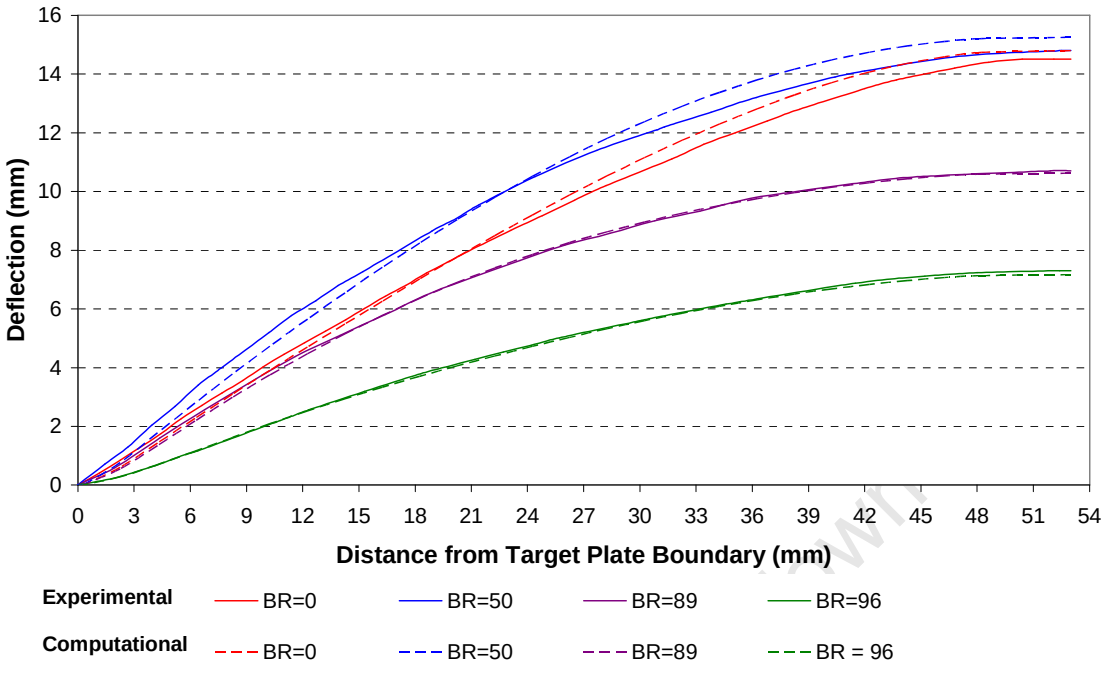

Figure 75: Graph of the experimental and computational target plate profiles for a 9 gram charge mass and blockage ratios of 0%, 50%, 89% and 96%

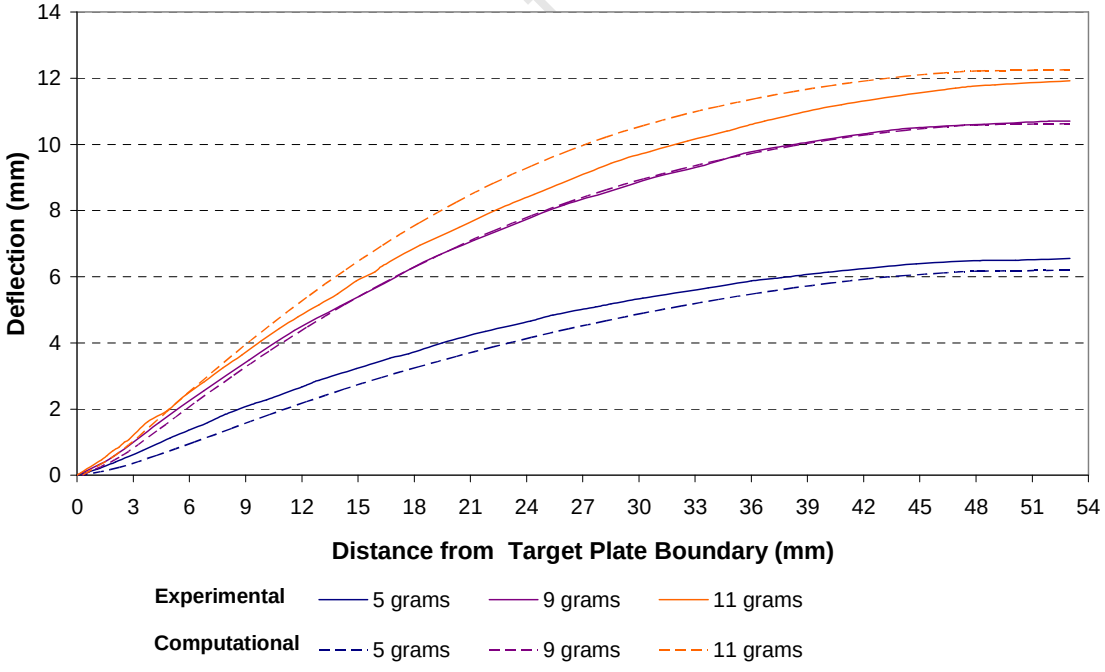

Figure 76: Graph of the experimental and computational target plate profiles for a blockage ratio of 89% and charge masses of 5, 9 and 11 grams

7.2.2 Perforated Plate Profile Comparison

Cross-sections of the computational and experimental perforated plates for a 9 gram charge mass are shown in Figure 77 for a blockage ratio of 89%. Both perforated plates showed deformation about a plastic hinge with little or no deformation along the arm length.

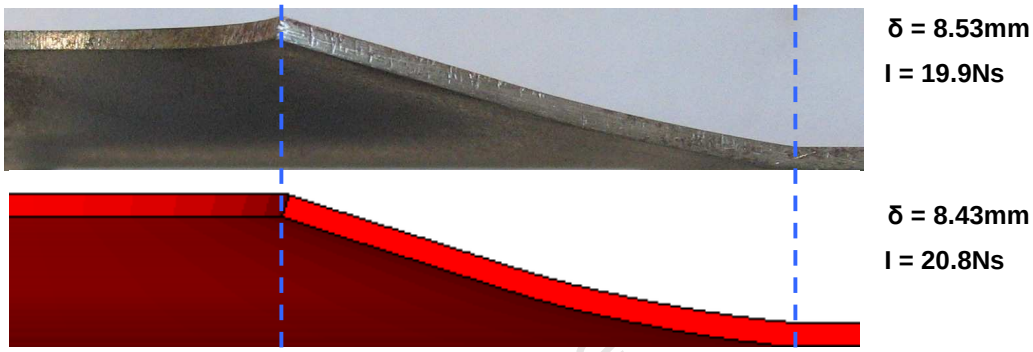

Figure 77: Perforated plate cross-sections for a 9 gram charge mass and a blockage ratio of 89%

The experimental and computational perforated plate profiles for several blockage ratios (namely 50%, 65%, 89% and 96%) are shown in Figure 78, for a 9 gram charge mass. The perforated plate profiles for several charge masses (namely 5, 9 and 11 grams) are shown in Figure 79, for a blockage of 89%. The perforated plate profiles show good correlation with variations in deflection of less than 1 plate thickness. The perforated plate profiles for a 9 gram charge mass for a blockage ratio of 25% are shown in Appendix C.

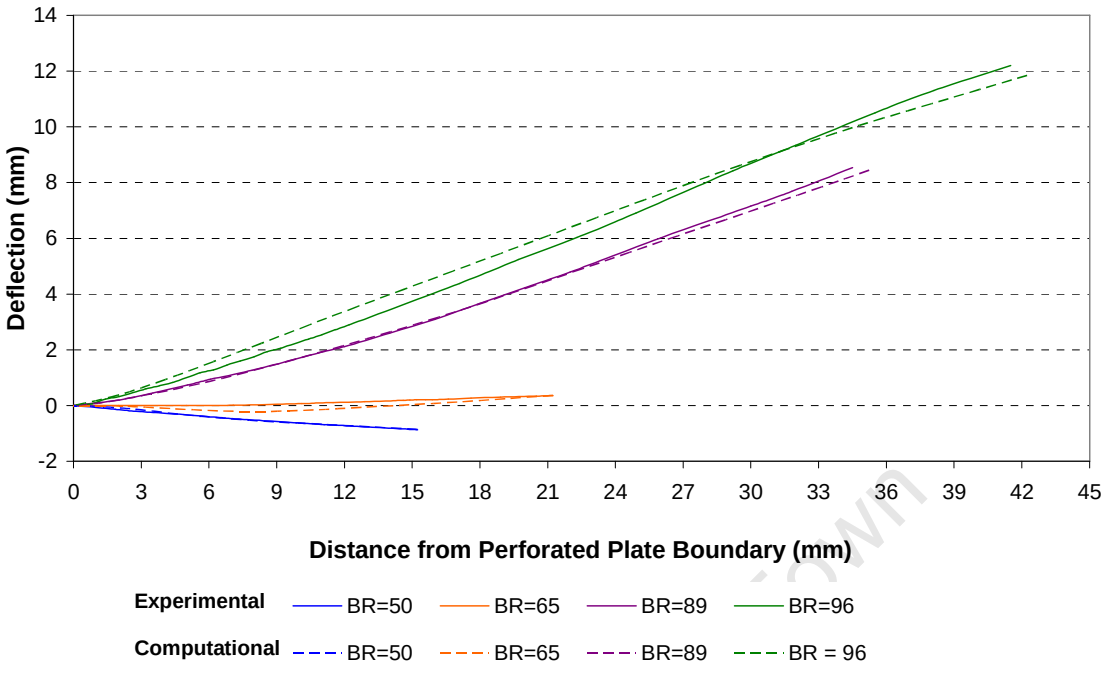

Figure 78: Graph of the experimental and computational perforated plate profiles for a 9 gram charge mass and blockage ratios of 50%, 65%, 89% and 96%

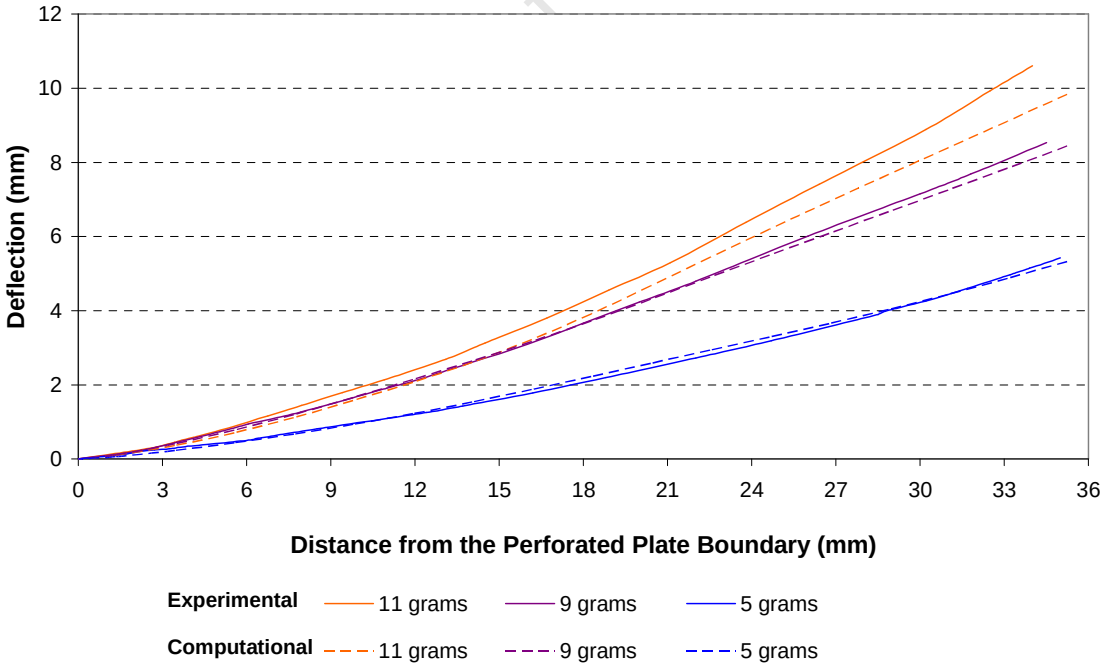

Figure 79: Graph of the experimental and computational perforated plate profiles for a blockage ratio of 89% and charge masses of 5, 9 and 11 grams

7.3 Blast Load Classification

Typical pressure-time histories are given in Figure 80, measured at the mid-point of the target plate and at the edge of the perforation of the perforated plate. The full load durations from initial pressure rise back to ambient conditions, ranged from 1.18ms to 2.10ms.

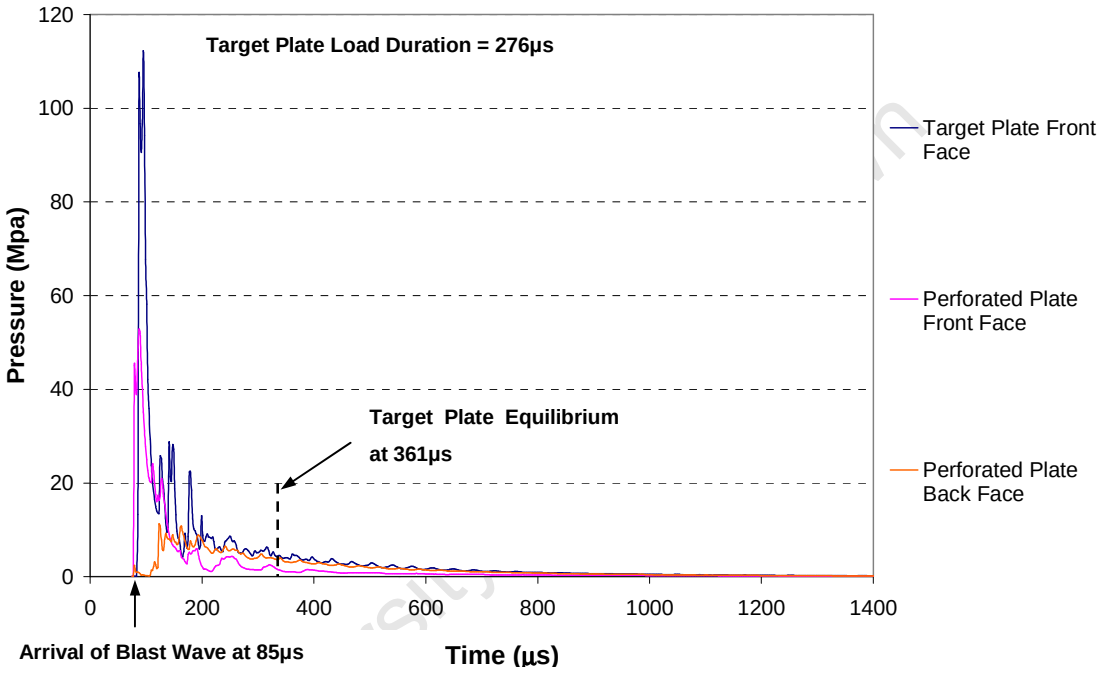

Figure 80: Graph of the pressure-time histories for a blockage ratio of 89% at an impulse of 20.8Ns

According to the Steel Construction Institute [9], a blast load is classified as 'impulsive' (damage caused is dependant on the impulse) if the duration of the load is less than the natural period of the structure. The target plate load duration was assumed to be the response time of the target plate (time interval from the arrival of the blast wave at the target plate surface to equilibrium). Any pressure acting on the target plate after equilibrium does not contribute to the deformation of the plate. The response times of the target plates, calculated using AUTODYN, ranged from 160µs to 367µs. The response times increased with an increase in blockage ratio, possibly due to the restriction of gas flow through the perforation, and decreased with an increase in impulse.

Young *et al* [39] gives the following equations for calculating the natural period (P_n) of circular plates fixed at the boundary:

$$P_n = \frac{1}{f} \tag{7.1}$$

$$f = \frac{K_n}{2\pi}\sqrt{\frac{Dg}{wr^4}} \tag{7.2}$$

$$D = \frac{Et^3}{12\left(1-\upsilon^2\right)} \tag{7.3}$$

$$\frac{w}{g} = m = \rho V \tag{7.4}$$

Where:

f = natural frequency of the plate

K_n = 10.2 (constant for plate geometry)

E = Young's modulus

g = gravitational constant

w = plate weight

m = plate mass

t = plate thickness

r = plate radius

υ = poisons ratio

ρ = plate density

V = plate volume

The natural period of the target plates was calculated as 66μs. The target plate load durations (response times) were between 3.2 and 5.5 times longer than the natural period of the target plates and therefore the blast loads are classified as 'dynamic'. The resultant damage to the plates therefore includes an investigation into the pressures and impulses acting on the plates. The load durations for all blockage ratios are given in Table 25.

Charge Mass (g)	Impulse AUTODYN Prediction (Ns)	Target Plate		Perforated Plate	
		Response Time (μs)	Full Load Duration (ms)	Front Face Full Load Duration (ms)	Back Face Full Load Duration (ms)
BR = 0					
5	12.1	216	1.18	-	-
7	16.4	196	1.20	-	-
9	20.9	185	1.24	-	-
11	25.2	165	1.31	-	-
13	29.2	160	1.30	-	-
BR = 25					
5	12.1	216	1.18	1.19	1.20
7	16.4	198	1.22	1.24	1.24
9	20.9	181	1.20	1.34	1.34
11	25.0	179	1.23	1.28	1.28
BR = 50					
5	12.2	266	1.19	1.19	1.20
7	16.4	219	1.23	1.23	1.25
9	21.1	203	1.27	1.26	1.27
BR = 65					
5	12.2	280	1.20	1.18	1.20
7	16.5	222	1.21	1.23	1.24
9	21.0	214	1.22	1.25	1.25
BR = 75					
5	12.3	287	1.20	1.18	1.20
7	17.6	249	1.24	1.23	1.23
9	22.7	242	1.29	1.27	1.27
11	27.4	232	1.31	1.30	1.31
BR = 89					
5	12.0	307	1.49	1.19	1.46
7	16.4	279	1.48	1.24	1.48
9	20.8	276	1.49	1.34	1.48
11	25.2	268	1.50	1.38	1.48
BR = 96					
5	11.6	367	2.09	2.10	2.10
7	16.1	332	1.87	1.88	1.88
9	20.5	302	1.92	1.92	1.92
11	24.6	288	1.92	1.92	1.92
13	28.7	287	1.90	1.91	1.91

Table 25: Load durations for blockage ratios of 0% to 96%

7.4 Preliminary Results

A preliminary investigation was performed for the baseline blockage ratio of 0% in order to determine if the chosen model gave reasonable results. The graph of target plate mid-point deflection versus impulse for both the experimental and computational results is given in Figure 81.

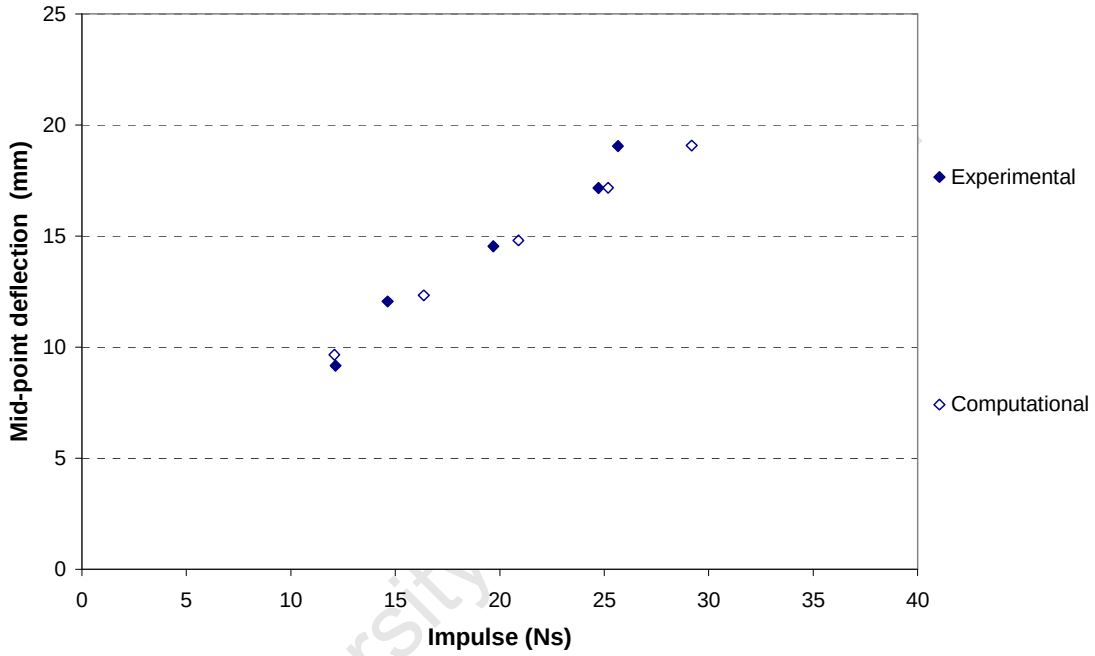

Figure 81: Graph of target plate mid-point deflection versus impulse for both the experimental and AUTODYN results for a blockage ratio of 0%

There was good correlation between the results with a maximum variation in impulse of 13.8% of the measured value for a given charge mass and a variation in the displacement values ranging from 0.01 to 0.31 plate thicknesses. A comparison of the results is presented in Table 26.

Charge Mass (g)	Impulse			Target Plate Deflection		
	Experimental (Ns)	AUTODYN Prediction (Ns)	Difference %	Experimental (mm)	AUTODYN Prediction (mm)	Difference in plate thicknesses d/t
5	12.1	12.1	0	9.16	9.65	0.31
7	14.6	16.4	11.8	12.05	12.33	0.18
9	19.7	20.9	6.1	14.54	14.8	0.16
11	24.7	25.2	1.9	17.16	17.17	0.01
13	25.7	29.2	13.8	19.05	19.07	0.01

Table 26: Comparison of the results obtained from the experiments and AUTODYN simulations for the baseline blockage ratio of 0%

7.5 Comparison of Experimental and Computational Impulse Results

The graph of charge mass versus impulse for the experimental and computational results is given in Figure 82. Out of twenty eight impulse values that were calculated using AUTODYN, the simulations predicted impulses within -9% and +13.8% of the experimental values, with the majority of the impulse values within +1.7% and +13.8%. As the charge mass increases the computationally predicted impulses become larger than the experimental values. It is expected that the majority of the computational impulse values would be higher, as AUTODYN is an ideal model not taking into account factors such as the effective mass of explosive.

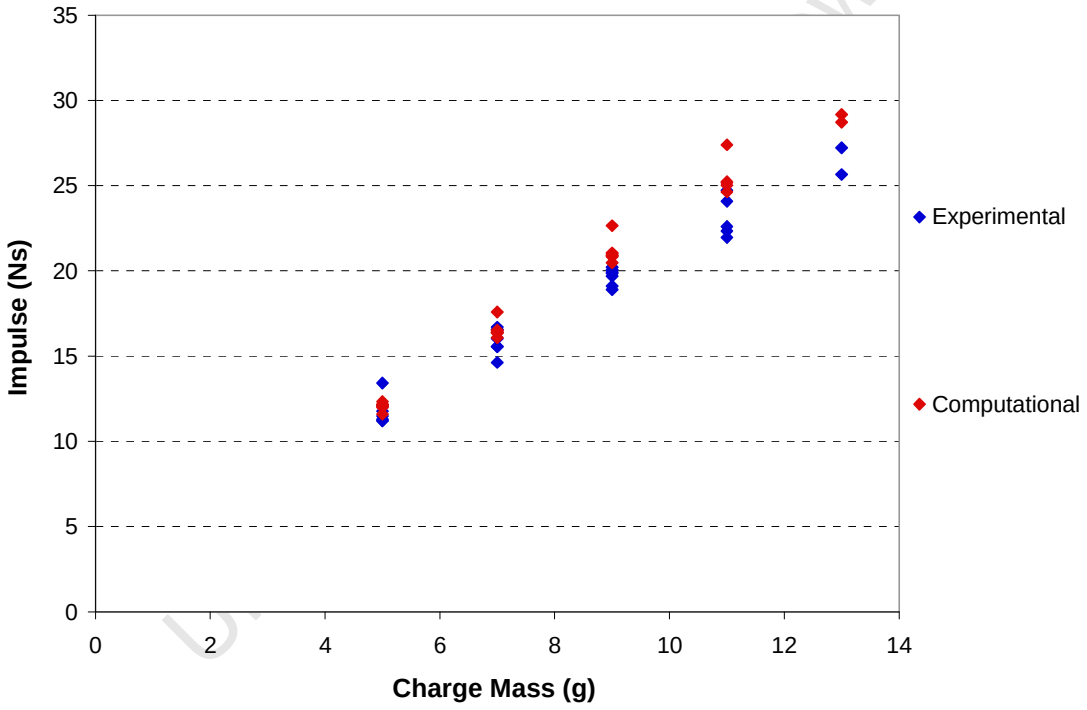

Figure 82: Graph of impulse versus charge mass for both experimental and computational results

A comparison between the experimental and computational impulse results is presented in Table 27 for blockage ratios of 25% to 96%. The comparisons include a breakdown of the impulse distribution between the perforated plate and target plate; these values were determined using AUTODYN.

Charge Mass (g)	Impulse		AUTODYN Impulse Breakdown			
	Experimental (Ns)	AUTODYN Prediction (Ns)	Target Plate I_{TF} (Ns)	Perforated Plate		
				I_{PF} (Ns)	I_{BF} (Ns)	Net (Ns)
BR = 25						
5	11.2	12.1	13.0	+ 2.1	- 3.1	-1.0
7	15.6	16.4	17.7	+ 2.9	- 4.2	-1.3
9	19.9	20.9	22.8	+ 3.5	- 5.4	-1.9
11	22.0	25.0	27.4	+ 4.0	- 6.4	-2.4
BR = 50						
5	11.2	12.2	13.7	+ 4.6	- 6.2	-1.6
7	15.6	16.4	18.9	+ 5.9	- 8.4	-2.5
9	18.9	21.1	24.3	+ 7.5	- 10.7	-3.2
BR = 65						
5	11.5	12.2	13.2	+ 6.3	- 7.4	-1.1
7	16.0	16.5	18.4	+ 8.3	- 10.2	-1.9
9	19.1	21.0	24.2	+ 10.1	- 13.2	-3.2
BR = 75						
5	13.4	12.3	12.8	+ 7.6	- 8.1	-0.5
7	16.5	17.6	18.2	+ 9.9	- 10.4	-0.6
9	20.1	22.7	24.3	+ 12.1	- 13.8	-1.7
11	24.1	27.4	29.5	+ 14.6	- 16.7	-2.1
BR = 89						
5	11.8	12.0	13.2	+ 9.5	- 10.7	-1.2
7	16.7	16.4	18.9	+ 12.9	- 15.4	-2.4
9	19.9	20.8	24.3	+ 16.3	- 19.8	-3.5
11	22.3	25.2	29.1	+ 19.8	- 23.7	-3.9
BR = 96						
5	11.3	11.6	14.1	+ 10.6	- 13.1	-2.5
7	16.5	16.1	18.6	+ 14.8	- 17.3	-2.5
9	20.2	20.5	25.3	+ 18.7	- 23.5	-4.8
11	22.6	24.6	31.4	+ 22.4	- 29.2	-6.8
13	27.2	28.7	37.1	+ 26.0	- 34.3	-8.3

Table 27: Comparison of experimental and computational impulse results for blockage ratios of 25% to 96%

7.6 Comparison of Experimental and Computational Deflections

7.6.1 Comparison of Experimental and Computational Target Plate Mid-point Deflections

A graph of target plate mid-point deflection versus impulse for both the experimental and computational results is shown in Figure 83. The experimental results are represented by the closed marker and the computational results by the open marker. The target plate mid-point deflections showed good correlation, with variations ranging from 0.01 to 0.74 plate thicknesses. Only one pair of data points fell outside this range, as indicated on the graph, having a difference in mid-point deflection of 1.22 plate thicknesses. A comparison between the experimental and computational mid-point deflection results is presented in Table 28.

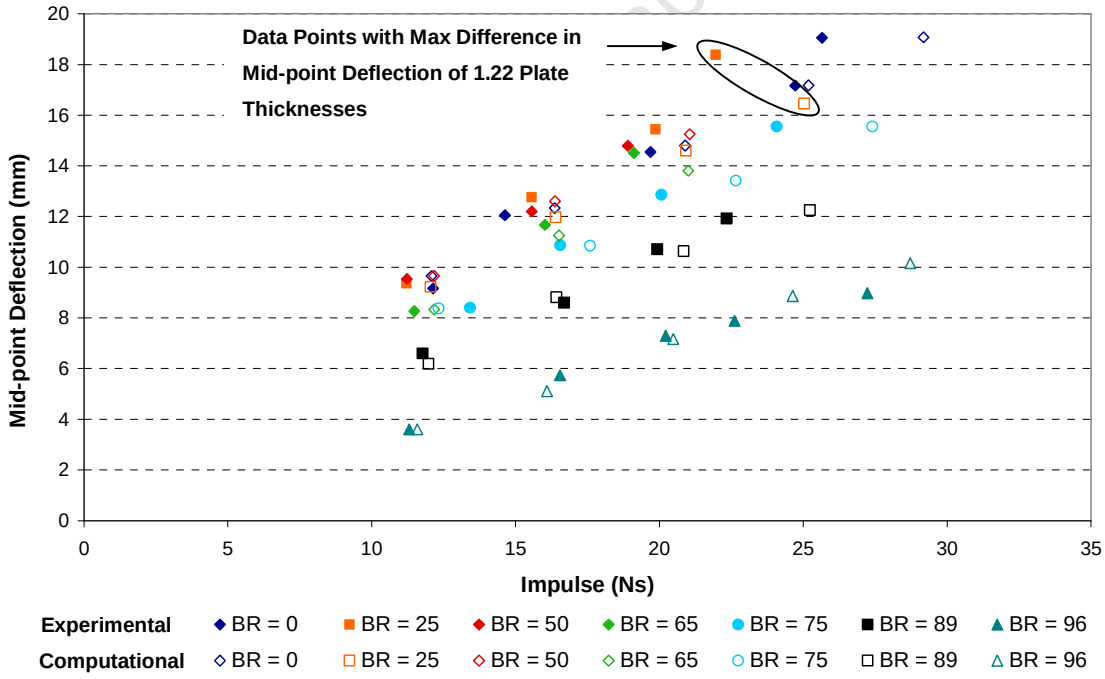

Figure 83: Graph of target plate mid-point deflection versus impulse for both the experimental and computational results for blockage ratios of 25% to 96%

Charge Mass (g)	Target Plate Deflection		
	Experimental (mm)	AUTODYN Prediction (mm)	Difference in plate thicknesses d/t
BR = 25			
5	9.36	9.22	- 0.09
7	12.76	11.97	- 0.50
9	15.45	14.59	- 0.53
11	18.38	16.45	- 1.22
BR = 50			
5	9.53	9.66	+ 0.08
7	12.20	12.60	+ 0.25
9	14.79	15.25	+ 0.29
BR = 65			
5	8.26	8.33	+ 0.04
7	11.67	11.25	- 0.26
9	14.50	13.80	- 0.43
BR = 75			
5	8.40	8.38	- 0.02
7	10.87	10.85	- 0.01
9	12.86	13.42	+ 0.35
11	15.55	15.55	0.00
BR = 89			
5	6.60	6.20	- 0.25
7	8.60	8.82	+ 0.14
9	10.71	10.63	- 0.05
11	11.92	12.25	+ 0.21
BR = 96			
5	3.60	3.60	0.00
7	5.73	5.11	- 0.39
9	7.29	7.16	- 0.08
11	7.88	8.86	+ 0.62
13	8.98	10.15	+ 0.74

Table 28: Comparison of experimental and computational target plate mid-point deflection results for blockage ratios of 25% to 96%

7.6.2 Comparison of Experimental and Computational Perforated Plate Average Deflections

A graph of perforated plate average deflection versus impulse for both the experimental and computational results is shown in Figure 84 for the blockage ratios of 25% to 75% and Figure 85 for the blockage ratios of 89% and 96%. The experimental results are represented by the closed marker and the computation results by the open marker. The experimental perforated plate average deflections for blockage ratios of 25% to 65% were less than 1mm in magnitude. The AUTODYN predictions with regard to magnitude were relatively good, with variations ranging from 0.01 to 0.36 plate thicknesses.

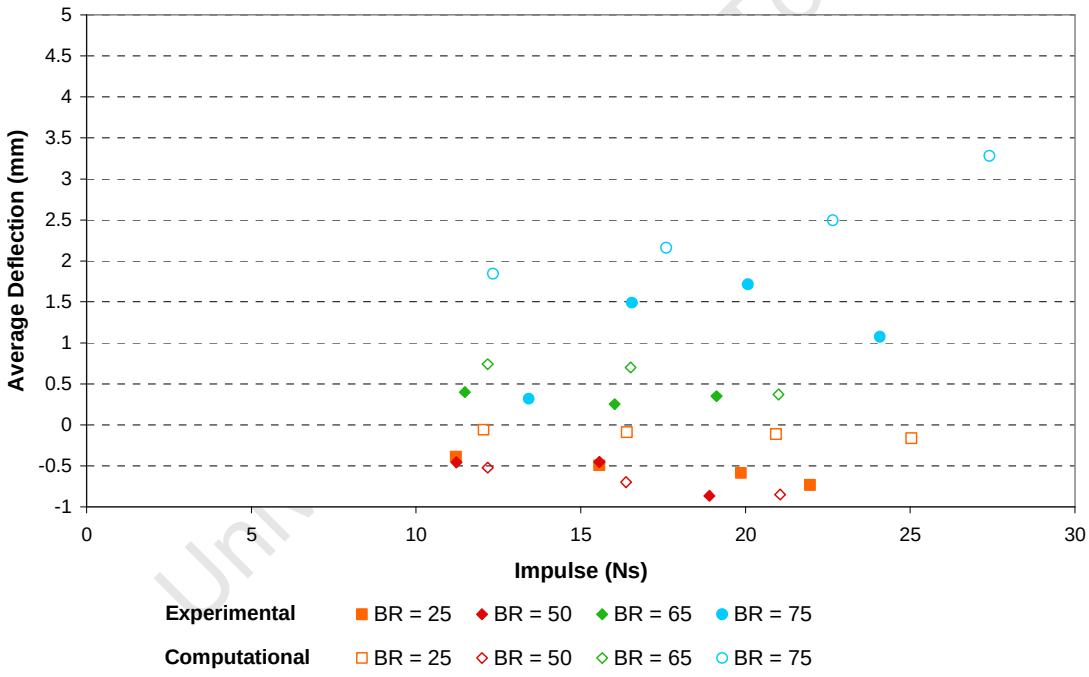

Figure 84: Graph of perforated plate average deflection versus impulse for both the experimental and computational results for blockage ratios of 25% to 75%

The direction of the perforated plate deflections was of more interest for blockage ratios of 25% and 50%, and in this respect the computational results correlated well with the experimental results, with AUTODYN predicting negative deflections, as observed in the experiments.

The perforated plates with a blockage ratio of 75% exhibited buckling, with final experimental deflections in both the positive and negative direction. The computational results did not predict this buckling behaviour, but did predict positive deflections within the experimental variation of each panel.

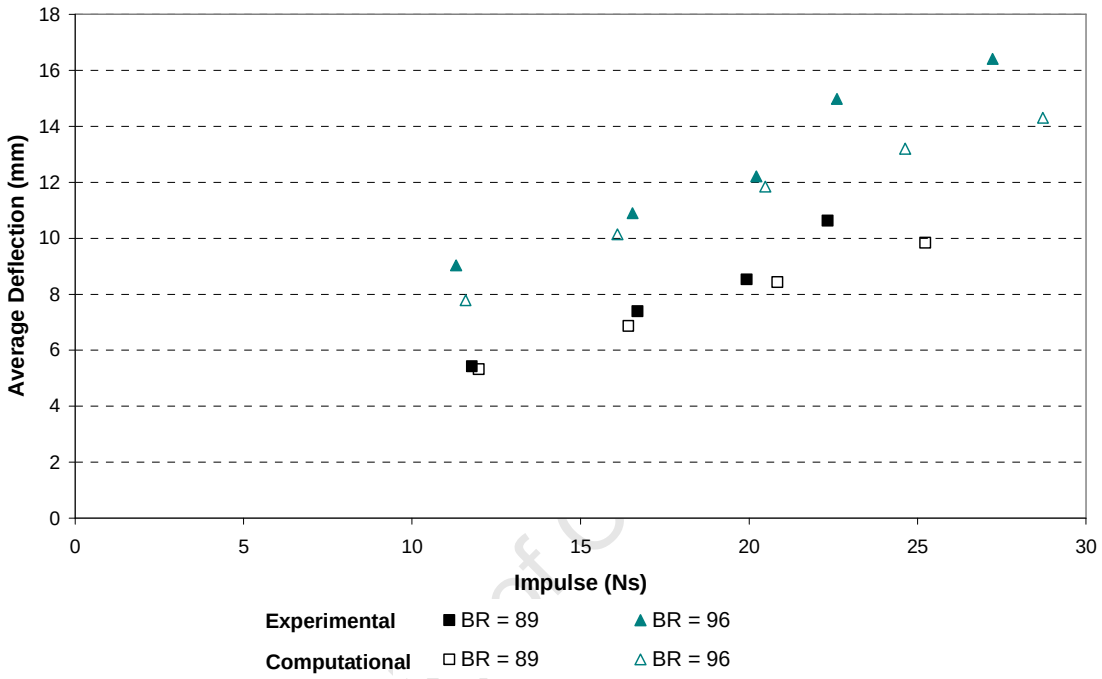

Figure 85: Graph of perforated plate average deflection versus impulse for both the experimental and computational results for blockage ratios of 89% and 96%

Blockage ratios of 89% and 96% showed good correlation between the experimental and computational results for charge masses between 5 and 9 grams. The plate deflections varied by between 0.07 and 0.95 plate thicknesses. At higher charge masses, namely 11 and 13 grams the deflections varied by as much as 1.38 of a plate thickness. A comparison between the experimental and computational results for all blockage ratios is presented in Table 29.

Charge Mass (g)	Perforated Plate Deflection		
	Experimental (mm)	AUTODYN Prediction (mm)	Difference in plate thicknesses d/t
BR = 25			
5	-0.39	-0.06	+ 0.20
7	-0.49	-0.09	+ 0.25
9	-0.59	-0.12	+ 0.30
11	-0.73	-0.16	+ 0.36
BR = 50			
5	-0.46	-0.52	- 0.04
7	-0.45	-0.70	- 0.15
9	-0.87	-0.85	+ 0.01
BR = 65			
5	0.40	0.74	+ 0.21
7	0.25	0.70	+ 0.28
9	0.35	0.37	+ 0.01
BR = 75			
5	0.32	1.84	+ 0.95
7	1.49	2.16	+ 0.42
9	1.71	2.50	+ 0.49
11	1.08	3.28	+ 1.38
BR = 89			
5	5.43	5.32	- 0.07
7	7.39	6.86	- 0.34
9	8.53	8.43	- 0.07
11	10.62	9.84	- 0.50
BR =96			
5	9.03	7.78	- 0.78
7	10.89	10.14	- 0.48
9	12.21	11.85	- 0.23
11	14.97	13.20	- 1.12
13	16.40	14.30	- 1.33

Table 29: Comparison of experimental and computational perforated plate average deflection results for blockage ratios of 25% to 96%

8. Discussion

8.1 Influence of Blockage Ratio on Transient Response

Further insight into the interaction between the blast wave and the test plates was gained from the AUTODYN simulations. The experimental and computational results revealed three distinct blockage ratio regions with regards to the perforated plate deflection. For blockage ratios of:

- 25% and 50% the perforated plates deformed in the opposite direction to the blast
- 89% and 96% the perforated plates deformed in the same direction as the blast
- 65% and 75% the experimental results showed deformation in both directions whilst the computational results deformed in the positive direction within the experimental variation of each panel.

One blockage ratio was chosen from each region and the simulation for 9 gram charge mass detonation was analysed.

8.1.1 Simulated Plate Response: Opposite to Blast Direction

The resultant deflections of the perforated plates with blockage ratios of 25% and 50% were in the opposite direction to the initial blast, deforming away from the target plate. A graph of perforated plate deflection versus time is shown in Figure 86 for a blockage ratio of 25% and a 9 gram charge mass. The pressure-time histories measured at the edge of the perforation nearest the centre, as shown in Figure 87A, for both the front and back faces of the perforated plate and the net effective pressure are also shown in Figure 86. The positive region of the net effective pressure represents the net pressure acting on the front face of the perforated plate in the same direction as the initial blast. The negative region represents the net pressure acting on the back face of the perforated plate in the opposite direction to the initial blast. The time is measured relative to detonation.

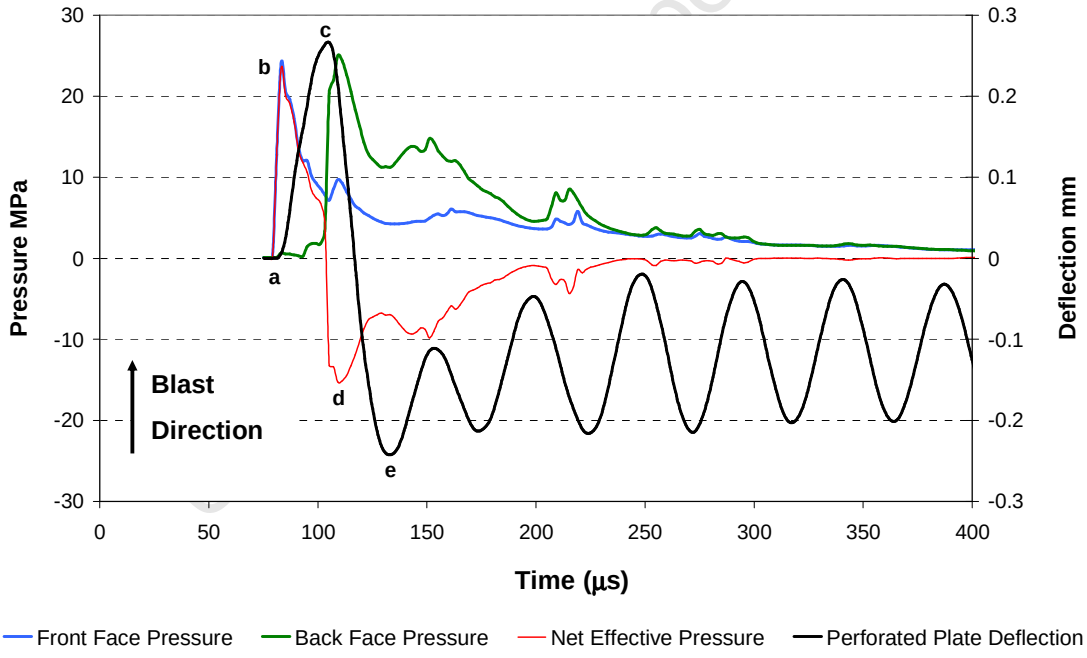

Figure 86: Graph of the deflection-time and pressure-time histories measured at the edge of the perforation for a blockage ratio of 25% and a 9 gram charge mass

These pressure-time histories are typical of those measured across the entire plate surface from the edge of the perforation to the boundary.

Pressure contour plots simulated using AUTODYN are shown at several time intervals in Figure 87. The perforated plate default colour was red and is not representative of the stress in the plate. The simulation proceeds as follows:

- The blast wave comes into contact with the front face of the perforated plate at approximately 81μs labelled (a) in Figure 86, resulting in an accumulation of pressure. The net effective peak pressure on the front face at the edge of the perforation is approximately 23.5MPa labelled (b) in Figure 86.
- The pressure distribution over the plate surface shown in Figure 87A, is relatively uniform with pressures between 26.8MPa and 33.5MPa deforming the perforated plate to a maximum of 0.26mm in the same direction as the initial blast, labelled (c) in Figure 86.
- During this time the blast wave moves through the perforation coming into contact with the target plate, first contacting the centre of the plate as shown in Figure 87B, then moving toward the boundary.
- As the blast wave reaches the boundary it reflects back toward the perforated plate as shown in Figure 87C, resulting in an accumulation of pressure on the back face of the perforated plate. The pressure distribution shown in Figure 87D ranges from 16.5MPa to 28MPa.
- At 103μs the net pressure on the perforated plate becomes negative acting in the opposite direction to the initial blast, resulting in a decrease in the perforated plate velocity. The net effective peak pressure at the edge of the perforation is approximately 15.3MPa (in the opposite direction to blast wave), labelled (d) in Figure 86.
- At 113μs the perforated plate changes direction, deforming in the opposite direction to the initial blast, to a maximum of -0.24mm in that direction, labelled (e) in Figure 86, before reaching an equilibrium deflection of -0.12mm.

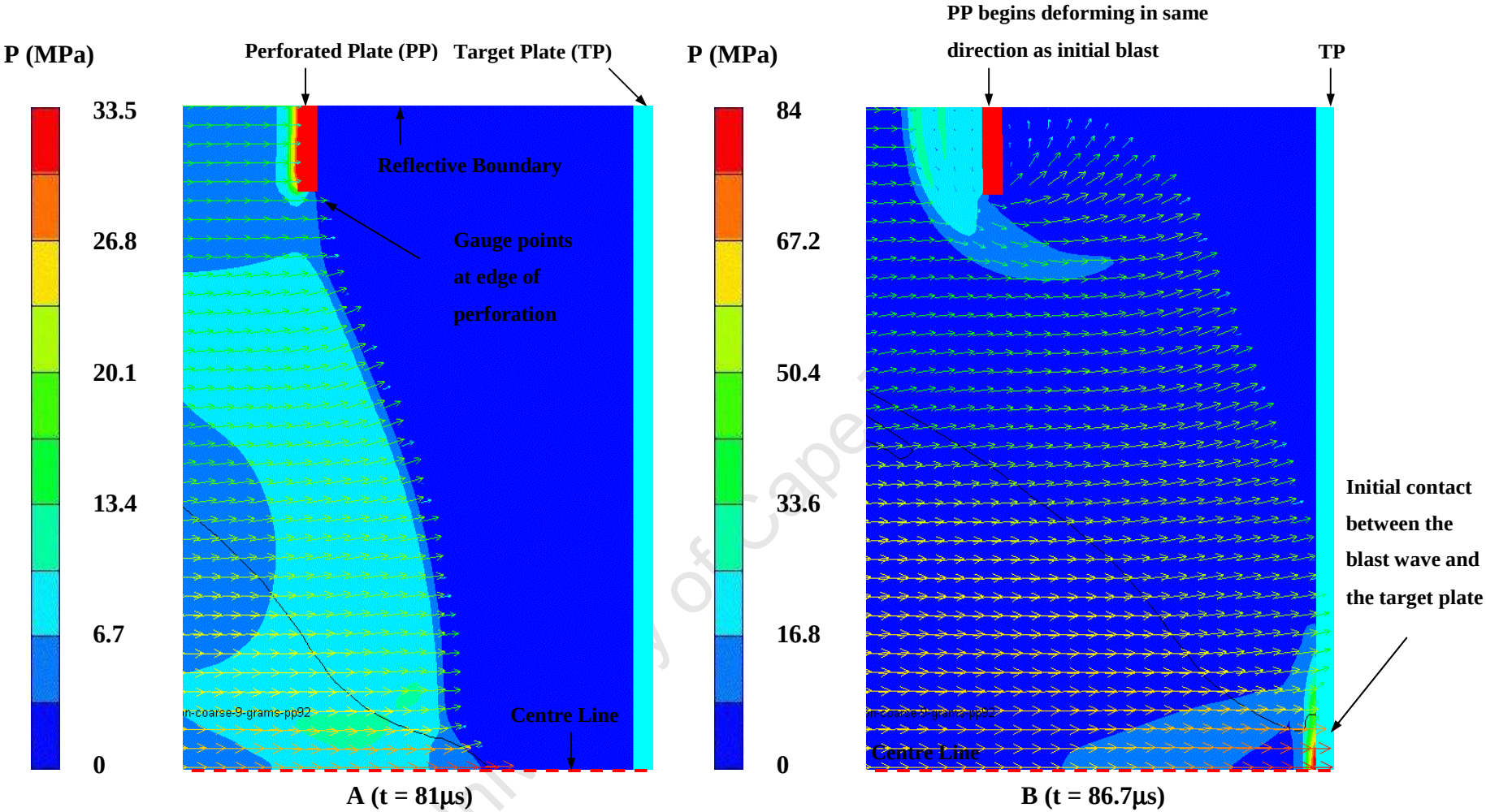

Figure 87: Pressure contour plots showing the distribution on the perforated plate with a blockage ratio of 25% at different time frames, from AUTODYN simulations

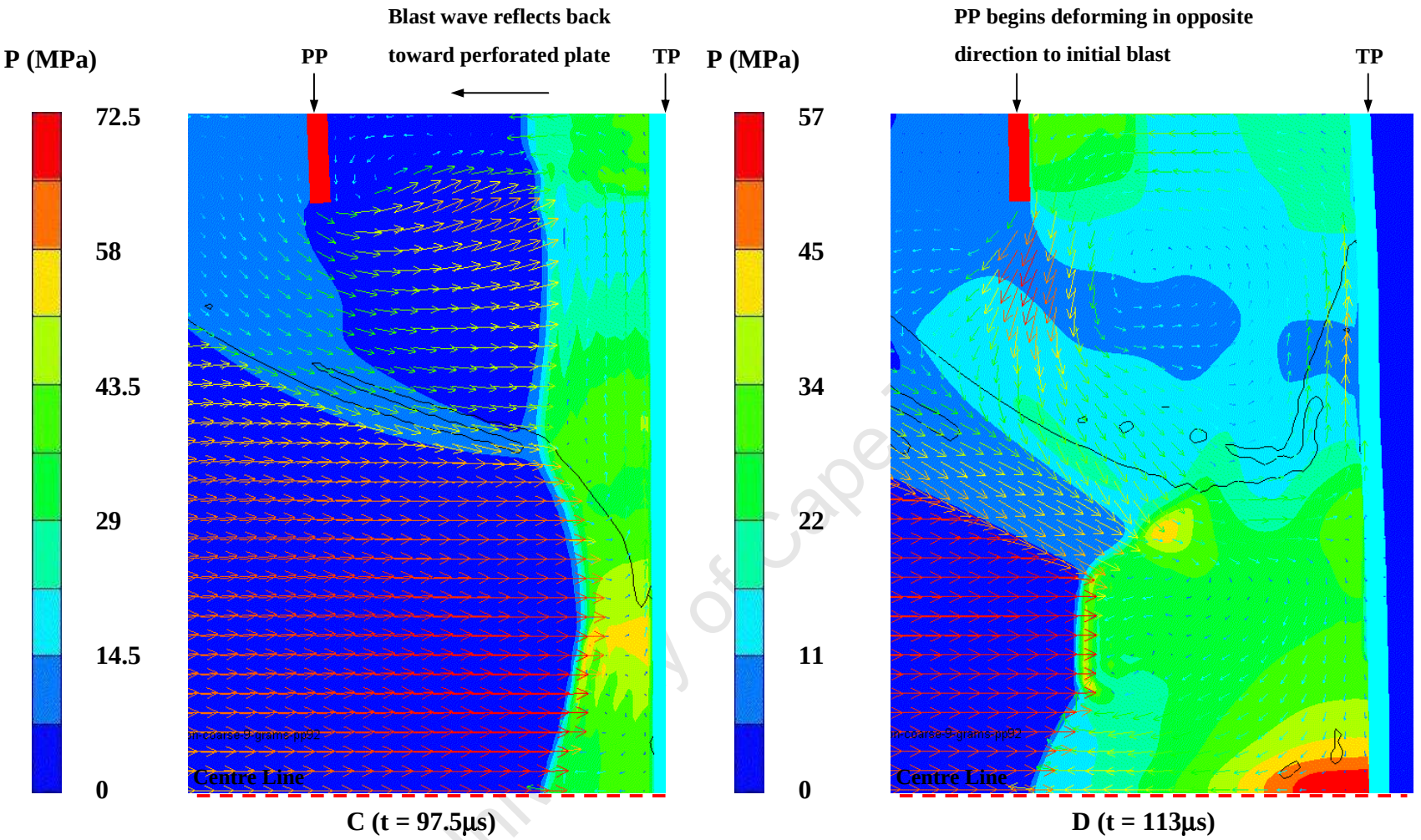

Figure 87 (Continued): Pressure contour plots showing the distribution on the perforated plate with a blockage ratio of 25% at different time frames, from AUTODYN simulations

Once the plate stops deforming any additional impulse acting on the plate has no effect on the plate deformation. Thus the impulses acting on the perforated plate over the response time were calculated and compared. The impulse acting on the front and back face of the perforated plate amounted to 1.39Ns and 2.32Ns respectively. The net impulse amounts to 0.93Ns, acting on the back face of the perforated plate in the direction opposite to the initial blast.

The specific impulse distribution over the front and back face of the perforated plate is shown in Figure 88, where:

- $I_{o\ PF}$ is the specific impulse distribution over the front face of the perforated plate, calculated over the response time.
- $I_{o\ PB}$ is the specific impulse distribution over the back face of the perforated plate, calculated over the response time.

Each bar represents the specific impulse measured by the relative gauge point along the arm length. The specific impulse on the front face is relatively uniform whilst the specific impulse acting on the back face increases toward the boundary, approximately 1.7 times larger at the boundary than at the edge of the perforation. The net distribution on the back face is shown in red.

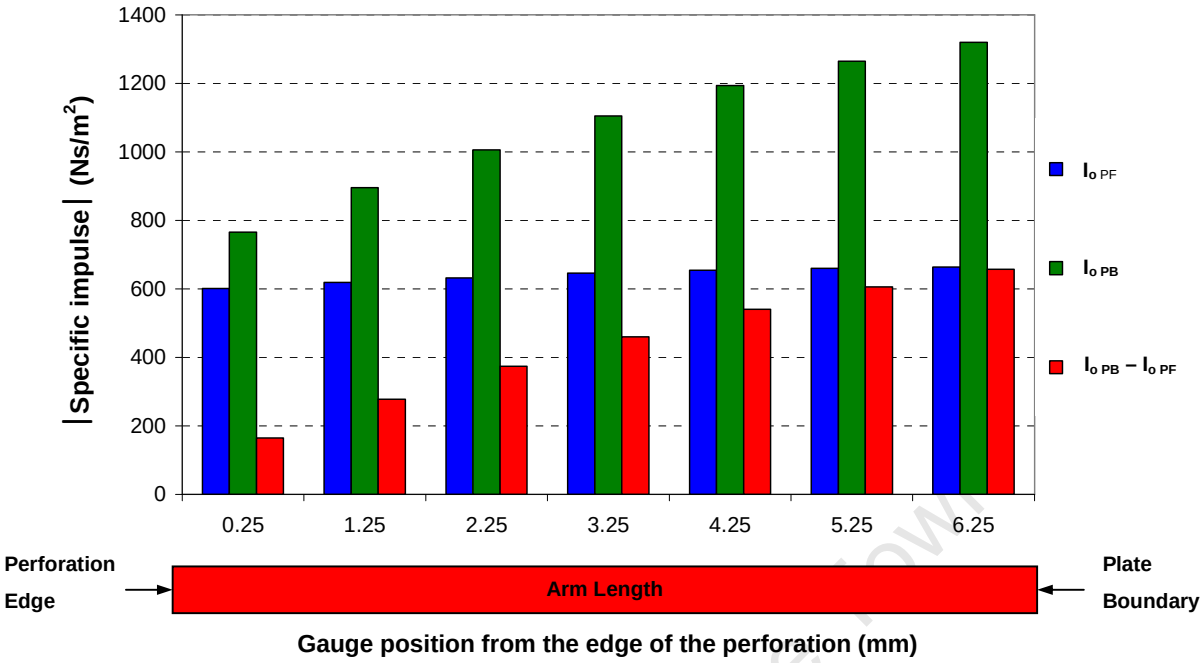

Figure 88: Graph of the specific impulse distribution over the front and back face of the perforated plate for a blockage ratio of 25%

8.1.2 Simulated Plate Response: Blockage Ratios in the Transition Region

The resultant experimental deflections of the perforated plates with a blockage ratio of 65% were less than 1mm in magnitude, deforming in the same direction as the initial blast. A graph of perforated plate deflection versus time is shown in Figure 89 for a blockage ratio of 65%. The pressure-time histories at the edge of the perforation for both the front and back faces of the perforated plate and the net effective pressure are also shown in Figure 89. The positive region of the net effective pressure represents the net pressure acting on the front face of the perforated plate in the same direction as the initial blast. The negative region represents the net pressure acting on the back face of the perforated plate in the opposite direction as the initial blast. The time is measured relative to detonation.

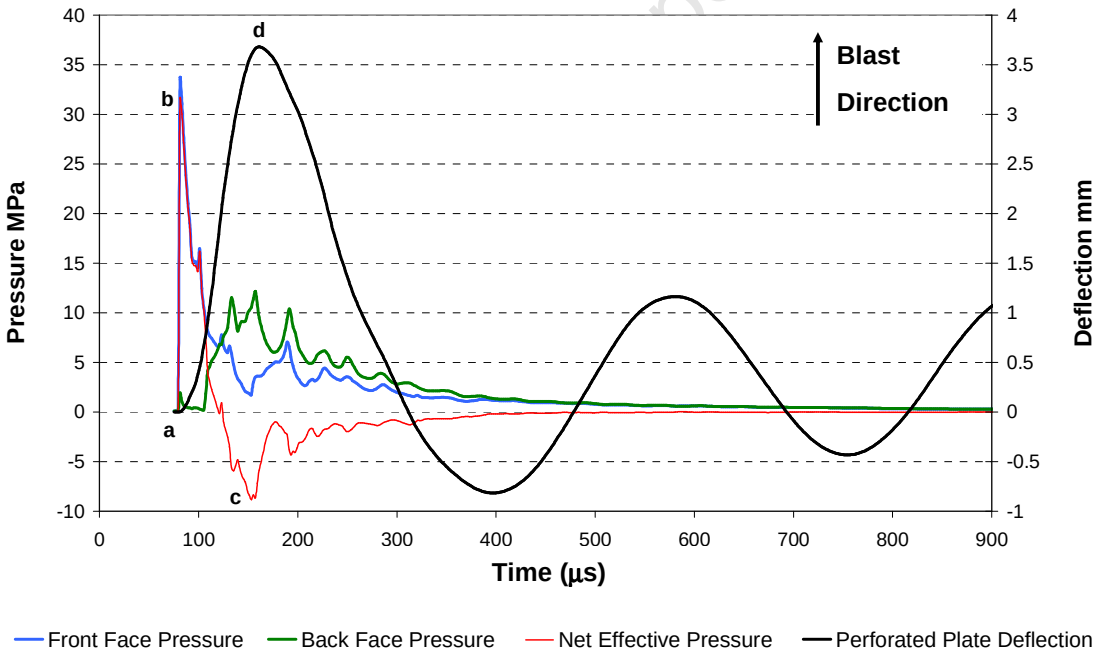

Figure 89: Graph of the deflection-time and pressure-time histories measured at the edge of the perforation for a blockage ratio of 65% and a 9 gram charge mass

Once again, these pressure-time histories are typical of those measured across the plate surface from the edge of the perforation to the boundary.

Pressure contour plots simulated using AUTODYN are shown at several time intervals in Figure 90.The simulation proceeds as follows:

- At 80.5μs, labelled (a) in Figure 89, the blast wave comes into contact with the front face of the perforated plate resulting in an accumulation of pressure. The net effective peak pressure on the front face at the edge of the perforation is approximately 31.5MPa labelled (b) in Figure 89.
- The pressure distribution shown in Figure 90A ranges from 26.4MPa to 52.8MPa, deforming the perforated plate to a maximum of 3.6mm in the same direction as the initial blast, as shown in Figure 90B.
- At approximately 120μs the net pressure acts in the opposite direction to that of the initial blast, following the accumulation of pressure on the back face of the perforated plate. The net effective peak pressure on the back face at the edge of the perforation is approximately 8.8MPa labelled (c) in Figure 89.
- The pressure distribution on the back face at 161.5μs shown in Figure 90B, ranges from 7.95MPa to 21.2MPa.
- Unlike the relatively uniform pressure distribution observed for a blockage ratio of 25%, high pressures are localized toward the boundary.
- This accumulation of pressure results in a decrease in the perforated plate velocity to zero at maximum deflection in the direction of the initial blast, at approximately 161.5μs labelled (d) in Figure 89.
- The plate deflection then changes direction, deforming to a maximum of -0.8mm in the opposite direction to the initial blast, before reaching an equilibrium deflection of 0.37mm in the same direction as the initial blast.

Although both of the test plates reach their equilibrium deflections by 500μs there is still a low pressure build-up between the plates, shown in Figure 90C, which has no further effect on the plate deformations however still contributes to the impulse measured on the front face of the target plate and back face of the perforated plate.

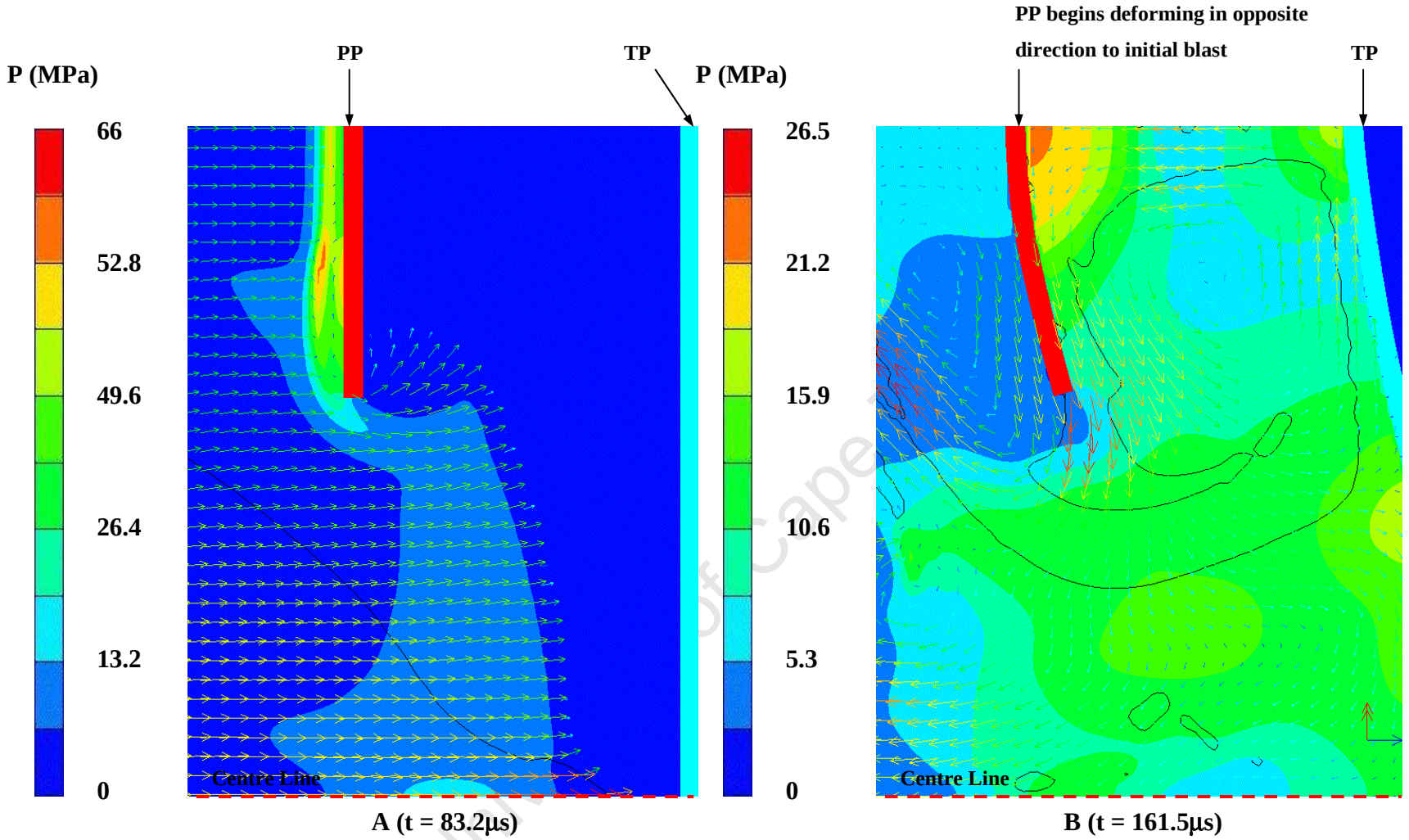

Figure 90: Pressure contour plots showing the distribution on the perforated plate with a blockage ratio of 65% at different time frames, from AUTODYN simulations

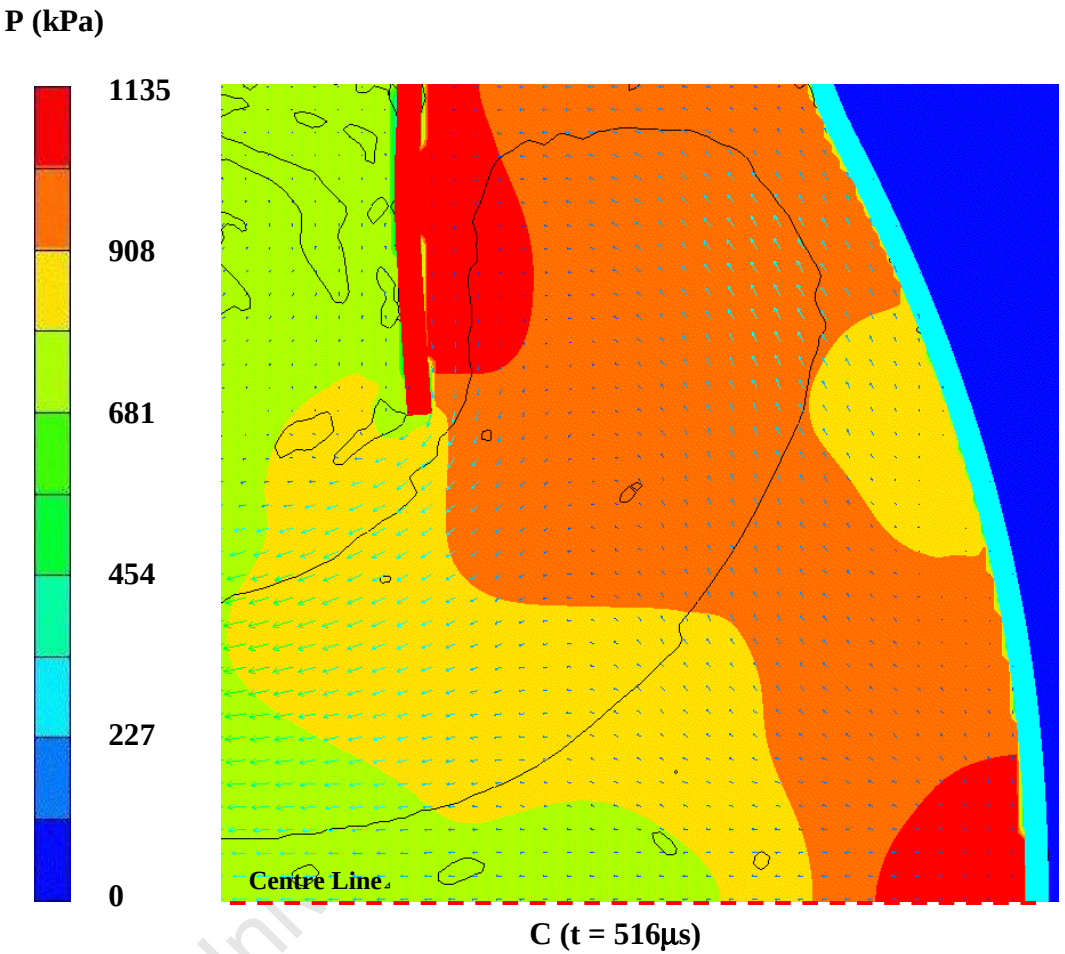

Figure 77 (Continued): Pressure contour plots showing the distribution on the perforated plate with a blockage ratio of 65% at different time frames, from AUTODYN simulations

The specific impulse distribution over the front and back face of the perforated plate is shown in Figure 91. Although the impulse acting on the back face is higher than that acting on the front face, the majority of this increase in impulse on the back face is distributed toward the boundary. The net distribution on the back face is shown in red.

The impulse acting on the front and back face of the perforated plate, calculated over the response time, amounted to 8.99Ns and 12.06Ns respectively. The perforated plate experiences a net impulse of 3.07Ns in the direction opposite to the initial blast. However the equilibrium deflection is the same direction as the initial blast. The interaction of the perforated plate deformation, spatial and temporal pressure distributions and the net applied impulse are clearly complicated phenomena.

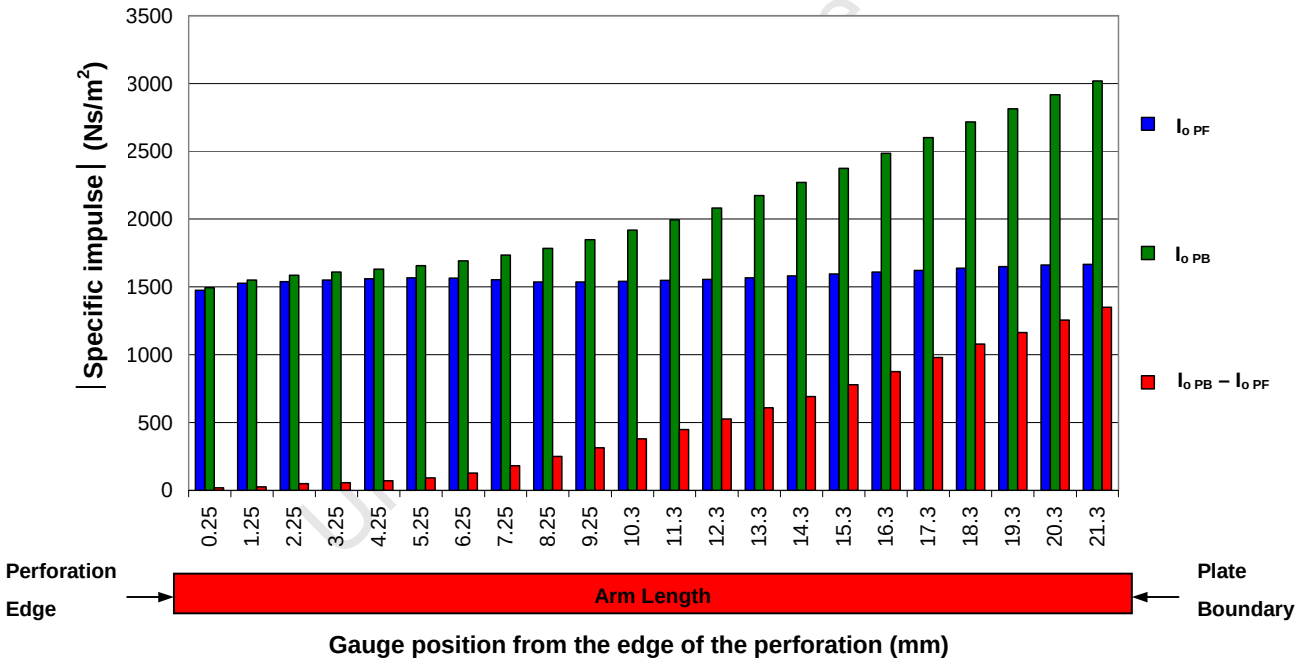

Figure 91: Graph of the specific impulse distribution over the front and back face of the perforated plate for a blockage ratio of 65%

8.1.3 Simulated Plate Response: In the Direction of the Blast Wave

The resultant deflections of the perforated plates with blockage ratios of 89% and 96% were in the direction of the initial blast with the deflections ranging from 5mm to 16mm. A graph of perforated plate deflection versus time is shown in Figure 92 for a blockage ratio of 89% and a 9 gram charge mass. The pressure-time histories at the edge of the perforation for both the front and back faces of the perforated plate and the net effective pressure are also shown in Figure 92. The positive region of the net effective pressure represents the net pressure acting on the front face of the perforated plate in the same direction as the initial blast. The negative region represents the net pressure acting on the back face of the perforated plate in the opposite direction to the initial blast. The time is measured relative to detonation.

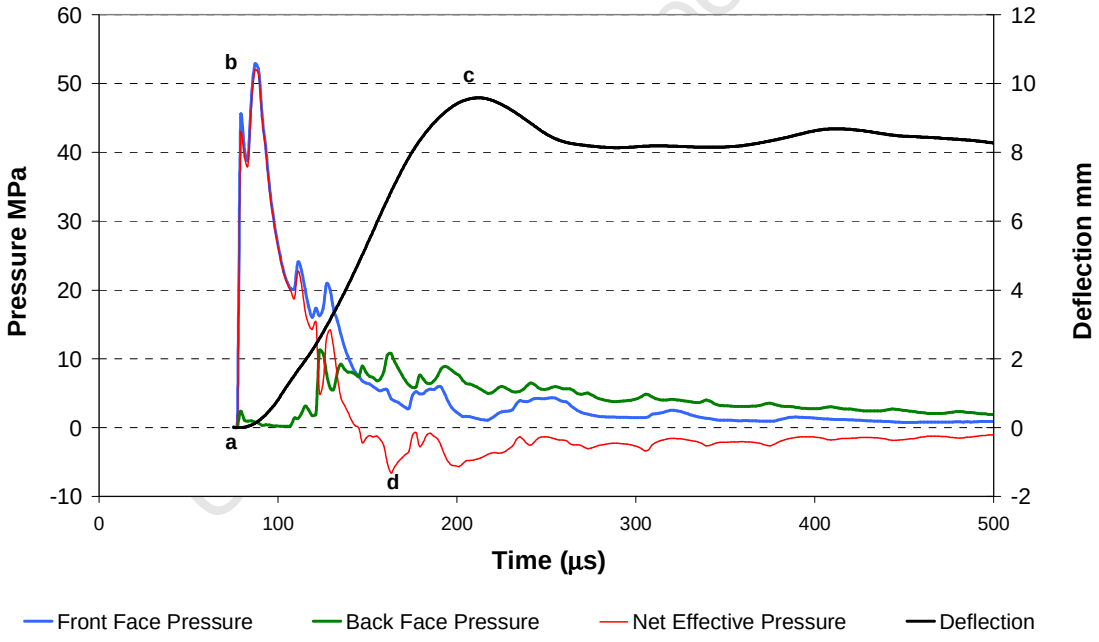

Figure 92: Graph of the deflection-time and pressure-time histories measured at the edge of the perforation for a blockage ratio of 89% and a 9 gram charge mass

As for the previous blockage ratios, the pressure-time histories shown in Figure 92 are typical of those measured over the surface of the perforated plate.

Pressure contour plots simulated using AUTODYN, are shown at several time intervals in Figure 93. The simulation proceeds as follows:

- At approximately 87μs, labelled (a) in Figure 92, the blast wave comes into contact with the front face of the perforated plate resulting in an accumulation of pressure. The net effective peak pressure on the front face at the edge of the perforation is approximately 31.5MPa labelled (b) in Figure 92.
- The pressure distribution over the plate surface shown in Figure 93A, ranges from 30MPa to 40MPa, deforming the perforated plate to a maximum of 9.5mm in the direction of the blast at approximately 210μs labelled (c) in Figure 92.
- The accumulation of pressure across the back face of the perforated plate shown in Figure 93B is relatively low due to the restriction of gas flow into the region between the plates, as the hole size is relatively small with a diameter of 35mm.
- The pressures on the back face range from 6.4MPa to 12.8MPa, as shown in the contour plot in Figure 93B.
- Although this pressure does result in a small negative net pressure reducing the velocity of the plate, it is insufficient to cause any significant reduction in the final deflection of the plate. The net effective peak pressure on the back face at the edge of the perforation is approximately 6.6MPa labelled (d) in Figure 92.
- By 254μs both the target plate and perforated plate have reached their equilibrium deflections with the remainder of the pressure adding to the impulse until the pressure returns to atmospheric.

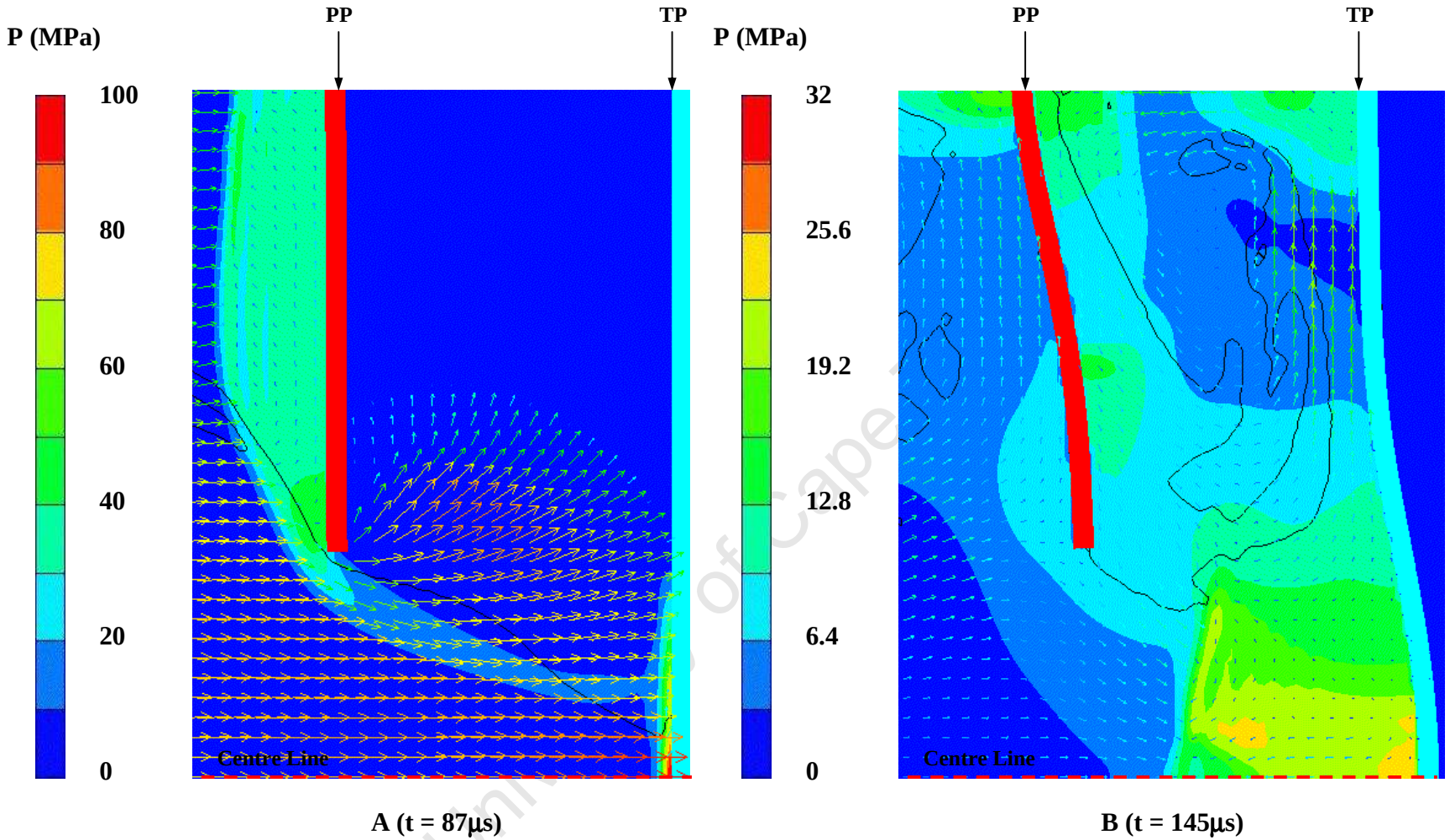

Figure 93: Pressure contour plots showing the distribution on the perforated plate with a blockage ratio of 89% at different time frames, from AUTODYN simulations

The impulse acting on the front and back face of the perforated plate calculated over the response time, amounted to 12.42Ns and 7.91Ns respectively. The specific impulse distribution over the front and back face of the perforated plate is given below in Figure 94. The specific impulse on the front face shows a larger distribution toward the edge of the perforation. This increases the effect of the impulse on the perforated plate deformation, due to the increase in the length of the moment arm. The specific impulse acting on the back face of the perforated plate is relatively uniform across the majority of the plate surface, increasing in magnitude toward the boundary.

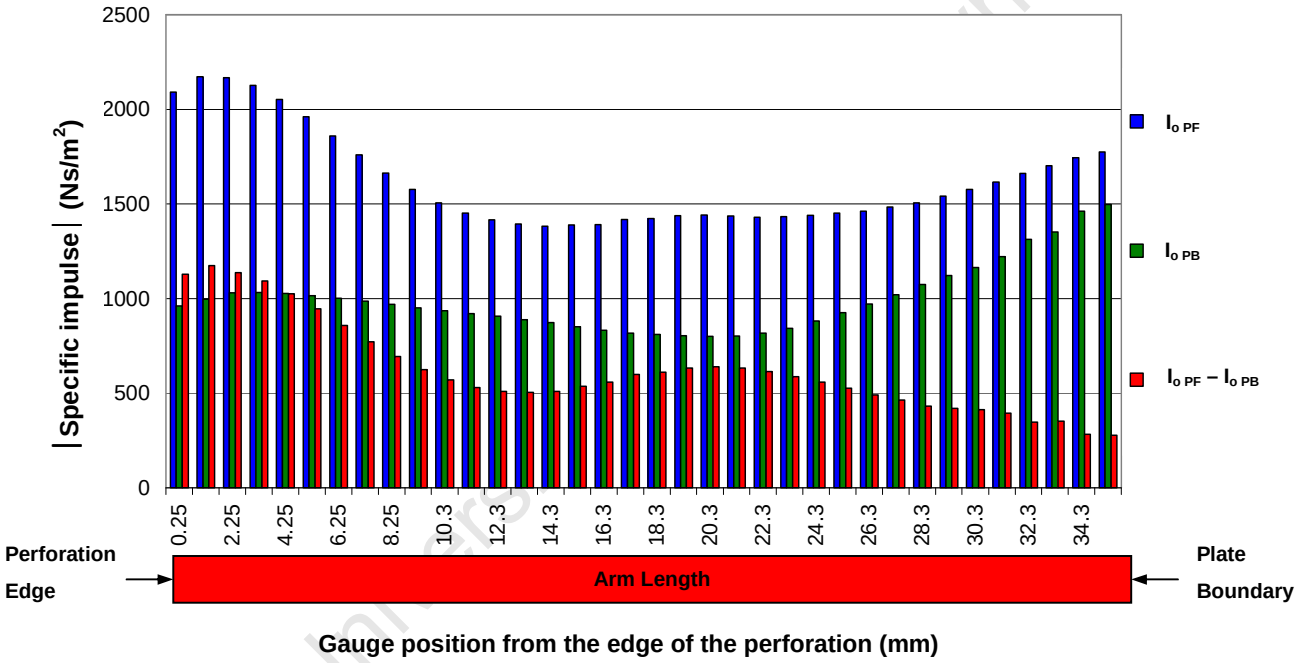

Figure 94: Graph of the specific impulse distribution over the front and back face of the perforated plate for a blockage ratio of 89%

8.2 Effect of Blockage Ratio on the Impulse Imparted to the Target Plate

A graph of impulse versus blockage ratio is shown in Figure 95, for a 9 gram charge mass. The following impulse values are shown for all blockage ratios:

- Impulse measured by the pendulum over the full load duration (I_{PEND})

$$I_{PEND} = I_{TF} + I_{PF} - I_{PB} \qquad \text{(Recall 6.7)}$$

- Impulse imparted to the front face of the target plate over the full load duration (I_{TF})
- Impulse imparted to the front face of the target plate over the response time (I_{TR})

The impulse values were estimated using AUTODYN. All impulses were calculated from the time the blast wave arrives at the target plate surface. For the response time the impulse was calculated up until equilibrium of the target plate deflection; typical values are between 160 µs and 367µs. For the full load duration the impulse was calculated up until the pressure reached atmospheric; typical values are between 1.18ms and 2.1ms. The natural period of the pendulum (T) is 3.4s, approximately 1600 times longer than the longest full load duration. The magnitude of the impulse is discerned using the amplitude of the pendulum movement (x_1, defined in Appendix B) after 850ms (1/4 swing), which is approximately 400 times longer than the highest load duration predicted by AUTODYN. The loading of the pendulum is therefore classified as impulsive, even though the structure subjected to the blast (target plate) is experiencing dynamic loading.

The ratio of the impulse imparted to the target plate over the response time, to the impulse imparted to the target plate over the full load duration is given as a percentage in Figure 95. This value represents the percentage of impulse imparted to the target plate that causes deflection.

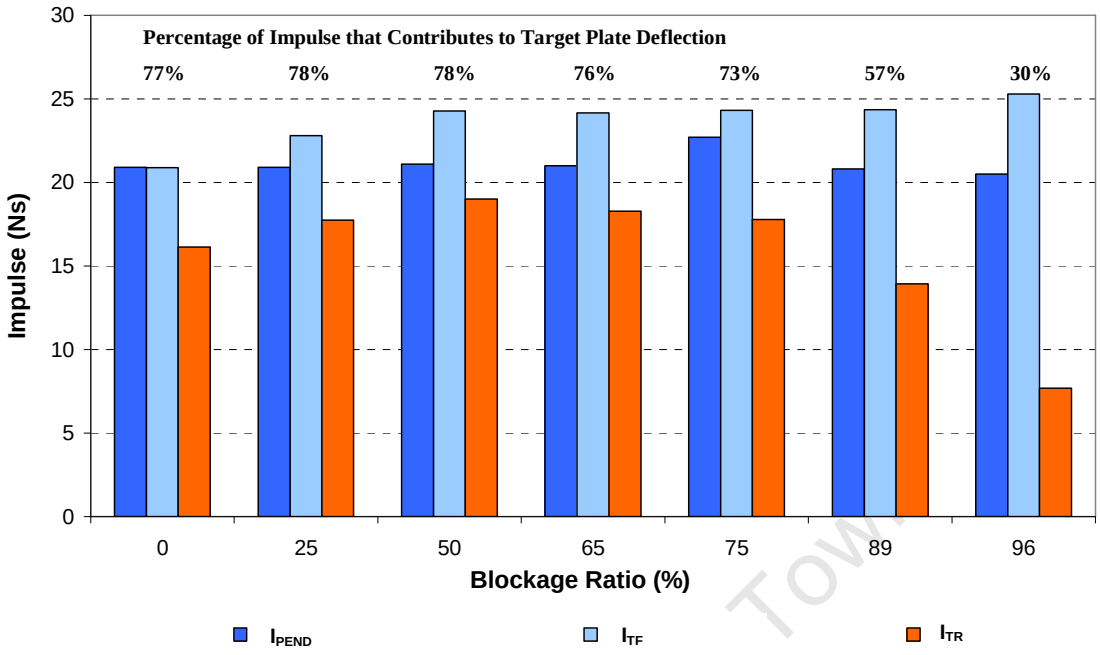

Figure 95: Graph of impulse versus blockage ratio obtained from AUTODYN simulations

The following observations were made, from Figure 95:

- For blockage ratios of 0% to 75% the percentages are fairly constant ranging from 73% to 78%.
- At higher blockage ratios namely 89% and 96% the percentages decreased to 57% and 30% respectively.
- A possible reason for the decrease at higher blockage ratios was the increase in the restriction of gas flow through the perforation. This throttling effect would cause the impulse to accumulate at a slower rate.
- The AUTODYN estimate of the impulses measured by the pendulum over the full load duration (I_{PEND}) ranged from 20.5Ns to 22.7Ns. The estimated impulse values were between 5.1% and 11.4% higher than the experimental results with impulse values ranging from 18.9Ns to 20.2Ns.

- The AUTODYN estimate of the impulse imparted to the target plate over the full load duration (I_{TF}) increased with an increase in blockage ratio. The impulse appeared to asymptote between blockage ratios of 50% and 96%, at an impulse of approximately 24.5Ns, for a 9 gram charge mass.
- The AUTODYN estimate of the impulse imparted to the target plate over the response time (I_{TR}) for blockage ratios between 25% and 75% are higher than that of the baseline blockage ratio of 0% where no perforated plate was inserted.
- The impulse increased with an increase in blockage ratio to a maximum of 19Ns at a blockage ratio of 50%, followed by a decrease in the impulse below that of the baseline ratio for blockage ratios of 89% and 96%. A possible reason for this trend is the combined effects of the restriction of the gas flow, both in and out of the region between the plates.
- The restriction of gas flow becomes more dominant for blockage ratios larger than 75% (53mm diameter), significantly decreasing the impulse imparted to the target plates over the response time for blockage ratios of 89% (35mm diameter) and 96% (21mm diameter).

8.2.1 Effect of Blockage Ratio on the Impulse at Tearing

The experimental results shown in Figure 49 on page 63, show that the impulse measured by the pendulum at tearing has a parabolic relationship to blockage ratio. Increasing the blockage ratio resulted in a decrease in the impulse at tearing with a best-fit trend line predicting a minimum at a blockage ratio of approximately 51%. The blockage ratio of 96% was the only ratio with an impulse at tearing higher than that of the baseline blockage ratio. A graph of normalised impulse (impulse imparted to the target plate over the response time) versus blockage ratio for a 9 gram charge mass, is shown in Figure 96. All the impulse values were normalised with respect to the baseline value represented by the dashed red line in Figure 96.

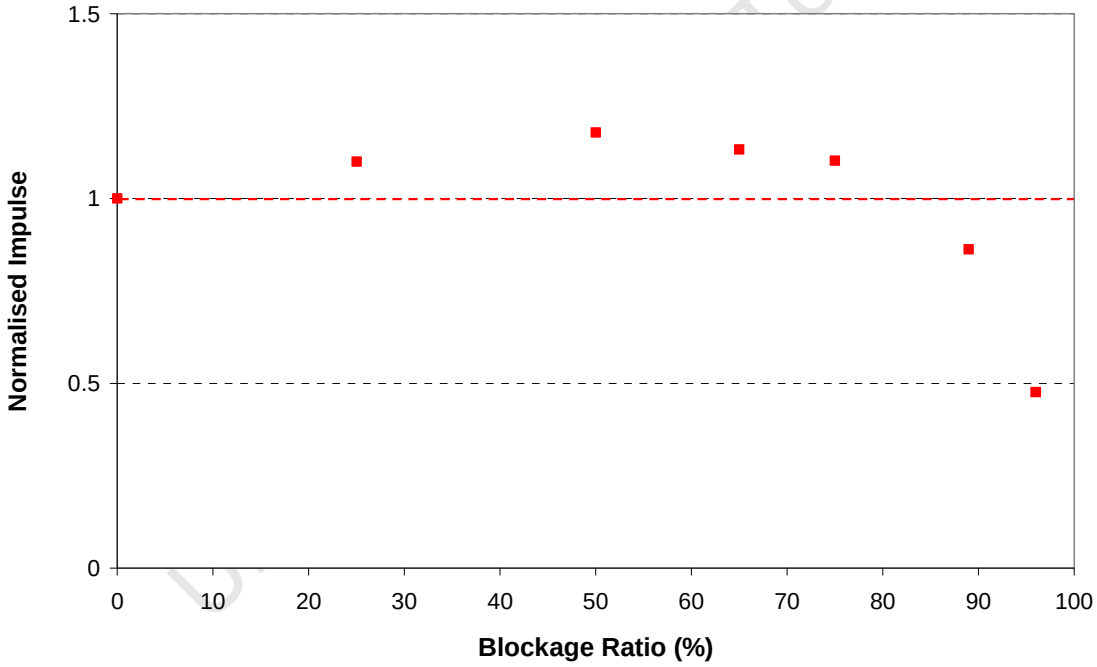

Figure 96: Graph of normalised impulse imparted to the target plate over the response time for blockage ratios of 0% to 89%

The increase in the impulse imparted to the target plate for blockage ratios between 25% and 75% relative to the baseline ratio, could result in the target plate reaching its threshold impulse at a lower total impulse, thus reducing the impulse measured by the pendulum at tearing.

8.3 Effect of Blockage Ratio on the Impulse Distribution across the Target Plate

The specific impulse distribution across the target plate is given in Figure 97 for blockage ratios from 25% to 75% and in Figure 98 for blockage ratios from 89% and 96%. The distributions for blockage ratios of 89% and 96% are shown separately for the purposes of clarity. The impulse distribution was calculated over the response time of the target plate with a charge mass of 9 grams for each blockage ratio. The baseline blockage ratio is represented by the dark blue dashed line in each figure. The distribution can be divided up into 3 regions for each blockage ratio as indicated for a blockage ratio of 75% in Figure 97 and for the baseline blockage ratio in Figure 98.

In Region 1:

- The distribution decreased almost linearly from the centre of the plate toward the boundary.
- Increasing the blockage ratio increased the magnitude of the specific impulse relative to the baseline ratio, for all except a blockage ratio of 96% which decreased in magnitude.
- The magnitude of the specific impulse increased to a maximum for a blockage ratio of 75%.
- Increasing the blockage ratio decreased the area over which the specific impulse acts.

In Region 2:

- The specific impulse decreased exponentially to a minimum, between 36.25mm and 42.25mm from the centre of the plate.
- Increasing the blockage ratio increased the area over which the specific impulse acts, shifting the minimum toward the boundary.
- The magnitude of the specific impulse for blockage ratios between 25% and 89% is higher than that of the baseline blockage ratio of 0% for the majority of the region, dropping below baseline at the minimum value for all plates except a blockage ratio of 25%.

In Region 3:

- The specific impulse for each blockage ratio increased almost linearly from the minimum toward the boundary, to a value between 1.4 and 2.3 times higher than that of the minimum.
- The magnitude of the specific impulse at the boundary for blockage ratios of 25% to 75% is between 1.2 and 1.3 times larger than that of the baseline ratio.
- The magnitude of the specific impulse at the boundary for blockage ratios of 89% and 96% is lower than that of the baseline ratio.

Despite the large variation of specific impulse across the surface of the target plates, the plates exhibited deformation typical of uniform loading. The unusual distributions however, may be the reason for the decrease in maximum mid-point deflection of the target plate before tearing with an increase in blockage ratio, as shown in Figure 50 on page 65.

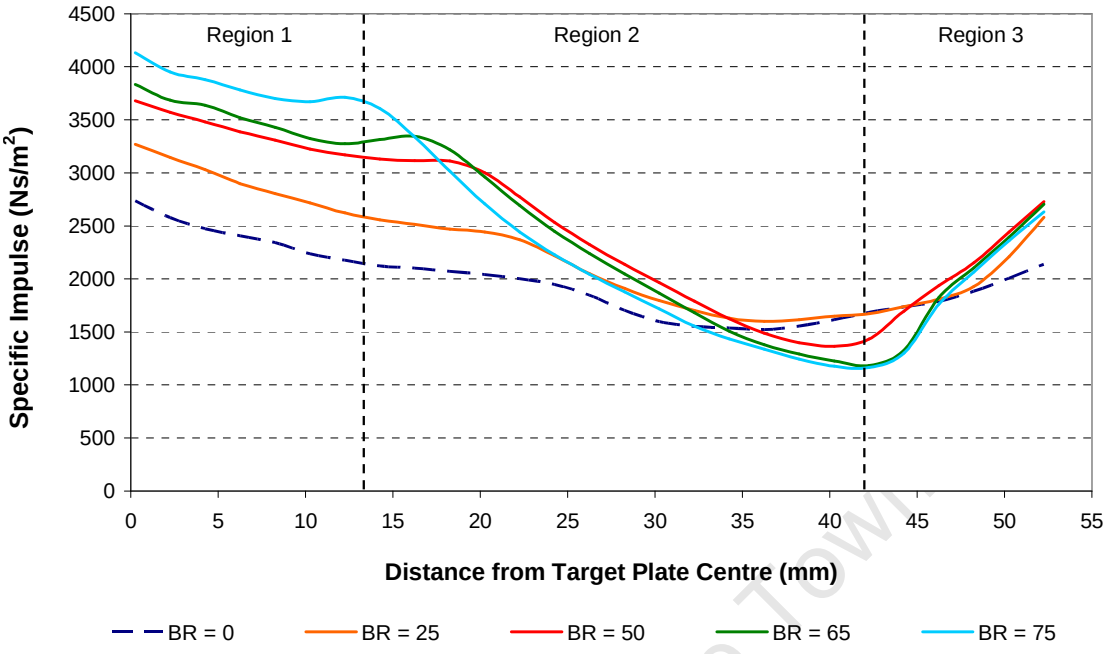

Figure 97: Graph of specific impulse versus distance from the target plate centre for blockage ratios from 25% to 75%

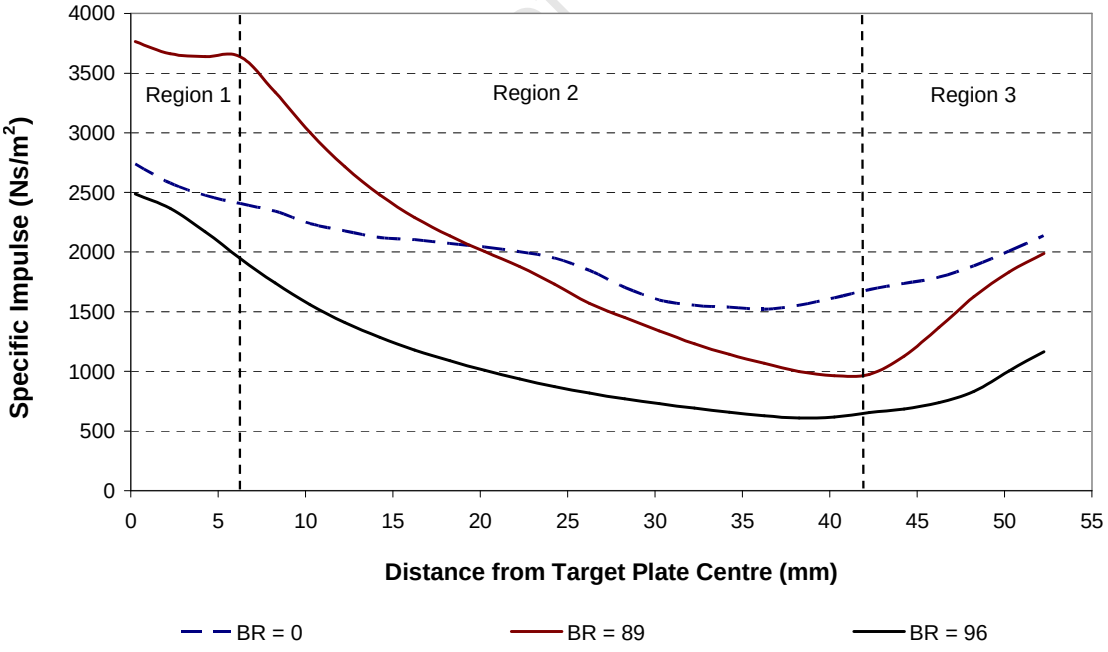

Figure 98: Graph of specific impulse versus distance from the target plate centre for blockage ratios from 89% and 96%

8.4 Modified Nurick and Martin Dimensionless Impulse

Nurick and Martin [2, 3] proposed a dimensionless impulse parameter (Φ_c), given by equation 2.9 and an empirical equation 2.10 for predicting large plastic deformation of fully clamped circular plates subjected to blast loads.

$$\phi_c = \frac{I\left(1+\ln\frac{R}{R_o}\right)}{\pi R t^2 (\rho\sigma_o)^{\frac{1}{2}}} \qquad \text{(Recall 2.9)}$$

$$\frac{\delta}{t} = 0.425\phi_c \qquad \text{(Recall 2.10)}$$

Jacob [16] modified this number by introducing a stand-off distance parameter (ζ_s) to account for the effect of the stand-off distance on the plate response. The modified dimensionless impulse is written as follows:

$$\phi_{cs} = \frac{I}{\pi R t^2 (\rho\sigma_o)^{\frac{1}{2}}} \times \frac{1+\ln\frac{R}{R_0}}{1+\ln\frac{S}{R_0}} \qquad \text{(Recall 2.12)}$$

8.4.1 Modified Dimensionless Impulse for a Blockage Ratio of 0%

The graph of mid-point deflection-thickness ratio versus modified dimensionless impulse (Φ_{cs}) is shown in Figure 99 for the experimental results with a baseline blockage ratio of 0%, where there was no perforated plate in between the explosive and the target plate. The empirical relationship proposed by Nurick and Martin [2, 3] is represented by the solid line.

Nurick [40] compared all available experimental results (up until 1989) of plates subjected to impulse loading by means of sheet explosive using equation 2.9. Nurick [40] showed by means of a statistical analysis of the results that for circular plates loaded impulsively, a 90% confidence limit is represented by ±1 mid-point deflection-thickness ratio confidence lines (there is a 90% probability that the deflection-thickness ratio will be within ±1 mid-point deflection-thickness ratio of the least squares fit).

The results in Figure 99 fall within the ±1 mid-point deflection-thickness ratio confidence lines showing good correlation with those reported by Jacob [16], for the same stand-off distance.

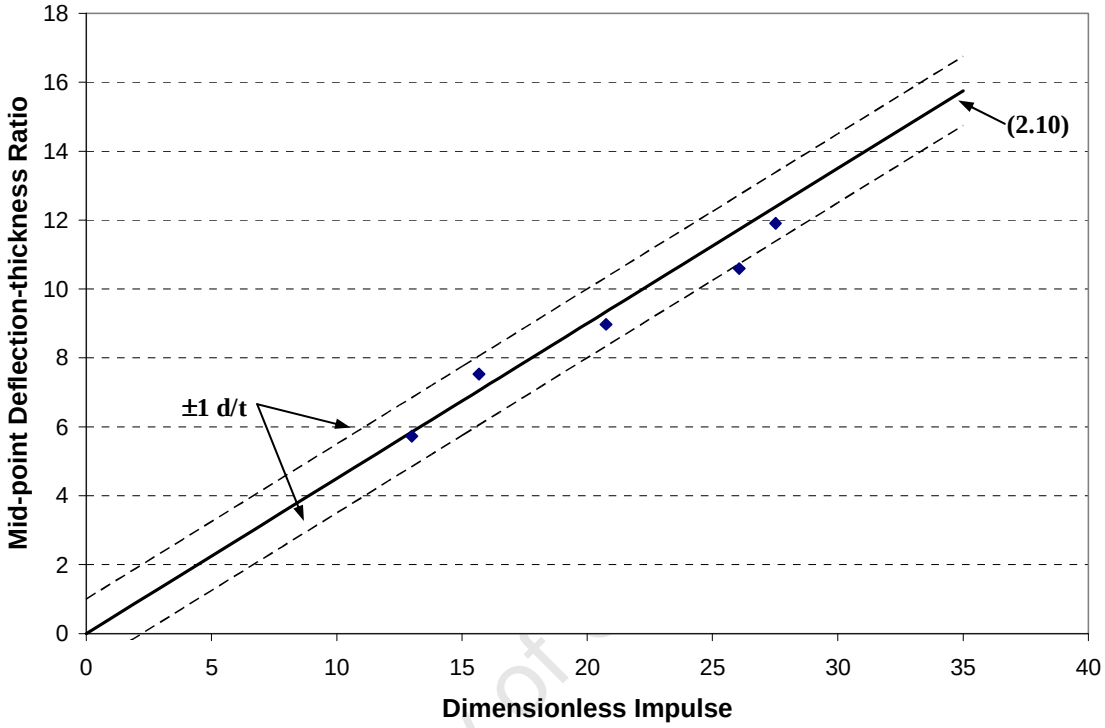

Figure 99: Graph of mid-point deflection-thickness ratio versus modified dimensionless impulse Φ_{cs} for the baseline blockage ratio of 0%

8.4.2 Modified Dimensionless Impulse for Blockage Ratios of 25% to 96%

A graph of mid-point deflection-thickness ratio versus modified dimensionless impulse (Φ_{cs}) is shown in Figure 100 for blockage ratios of 25% to 96%. The baseline blockage ratio results are also included on the graph. The experimental results are indicated by the closed markers and the computational results the open markers. The empirical relationship proposed by Nurick and Martin [2, 3] is represented by the solid line.

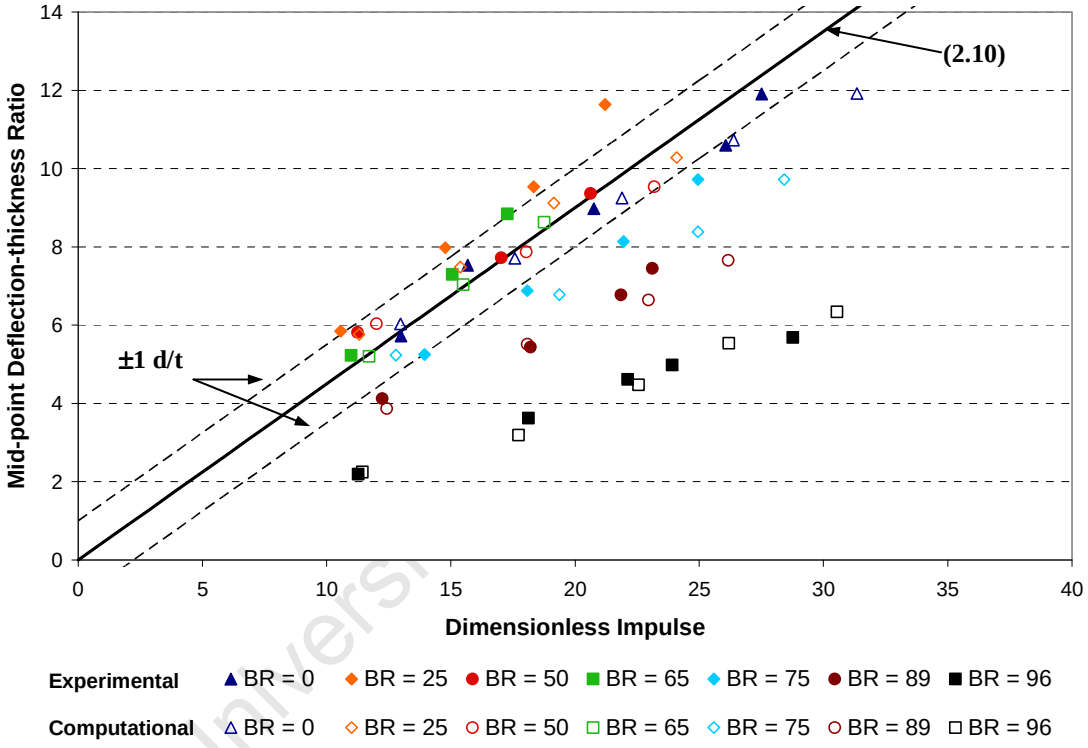

Figure 100: Graph of mid-point deflection-thickness ratio versus modified dimensionless impulse Φ_{cs} for blockage ratios of 25% to 96%

For a blockage ratio of 25%:

- The experimental data points are above the empirical line, whilst the computational results fall within the ±1 mid-point deflection-thickness ratio confidence lines.

For blockage ratios of 75% to 96%:

- Both the experimental and computational mid-point deflections are larger than the trend line.

For blockage ratios of 0%, 50% and 65%:

- Both the experimental and computational data falls within the ±1 mid-point deflection-thickness ratio confidence lines.

8.5 Target Plate Profiles

The failure of circular plates subjected to a uniformly distributed impulse was investigated by Teeling-Smith and Nurick [13]. The plate profiles were compared to several deformation shape functions proposed by Duffey [41], used for describing the final deformation profile of clamped circular plates loaded impulsively. Teeling-Smith and Nurick [13] reported good correlation between the plate profiles and the following shape function:

$$\delta = \delta_o \cos\frac{\pi r}{2R} \tag{8.1}$$

Where δ is the deflection at a radius r, δ_o is the maximum deflection and R is the outer radius of the plate. The experimental target plate profiles for a 9 gram charge mass are shown in Figure 101, for blockage ratios of 0%, 50%, 89% and 96%, along with the shape functions. A variation in deflection of less than one plate thickness is observed for all blockage ratios. The profile comparisons for blockage ratios of 25%, 65% and 75% are shown Appendix C.

Target plate profiles for charge masses of 5, 9 and 11 grams are shown in Figure 102 for a blockage of 89%, along with the shape functions. A variation in charge mass has little effect on the correlation between the shape function and the experimental plate profile, with the shape function under predicting the plate deformation for all charge masses.

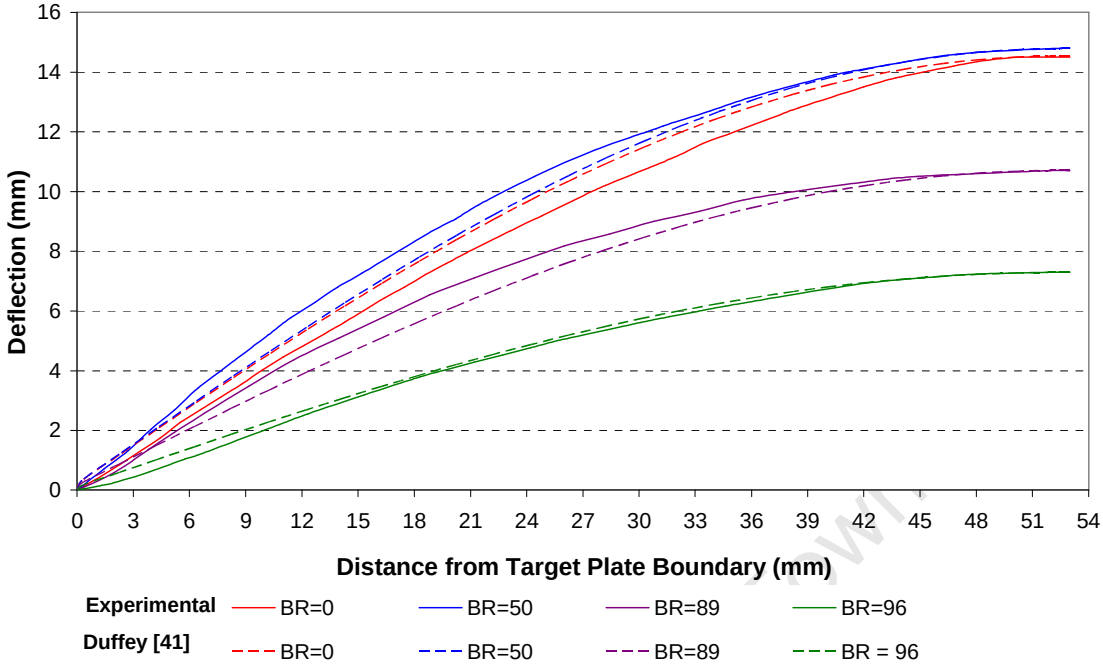

Figure 101: Graph of the experimental target plate profiles and Duffey [41] shape functions for a 9 gram charge mass and blockage ratios of 0%, 50%, 89% and 96%

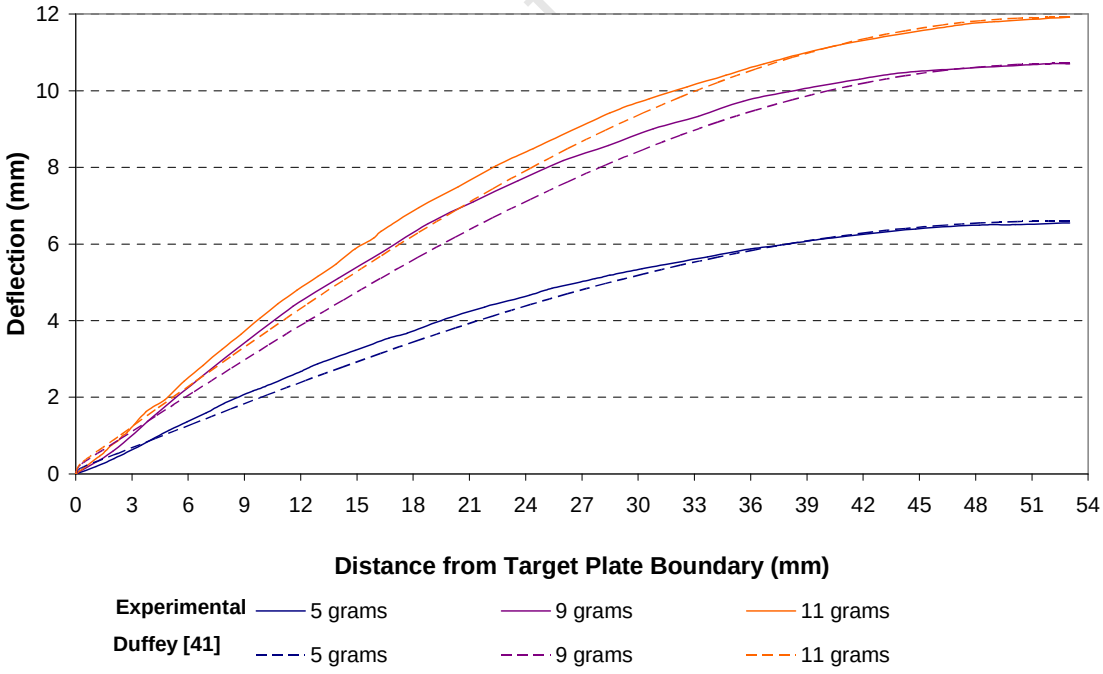

Figure 102: Graph of the experimental target plate profiles and Duffey [41] shape functions for a blockage ratio of 89% and charge masses of 5, 9 and 11 grams

9. Conclusions

The effect of using perforated plates as a blast wave mitigation technique was investigated both experimentally and numerically, focusing on the effects of the perforated plate blockage ratio (defined by the perforated plate hole size) and the perforated plate thickness. Based on the findings of this investigation, the following conclusions are drawn:

Effect of Blockage Ratio on the Target Plate Mid-point Deflection

For a given impulse increasing the blockage ratio to 25% resulted in an increase in the target plate mid-point deflection. A blockage ratio of 50% had little or no influence on the mid-point deflection whilst all other blockage ratios resulted in a decrease in the mid-point deflection.

Effect of Blockage Ratio on the Tearing Threshold of the Target Plate

The relationship between the impulse at tearing of the target plates and the blockage ratio was parabolic in nature, with all blockage ratios reducing the impulse threshold of the target plates. The exceptions to this were target plate systems with a blockage ratio of 96%. The best-fit trend line through the data-points predicted a minimum impulse tearing threshold at a blockage ratio of approximately 51%.

Effect of Blockage Ratio on the Perforated Plate Average Deflection

The experimental results revealed three distinct deflection regions. For blockage ratios of 25% and 50% the perforated plate deflection was in the opposite direction to that of the initial blast. For blockage ratios of 89% and 96%, the deflection of the perforated plates was in the same direction as the initial blast. Perforated plates with blockage ratios of 65% and 75% buckled, with each plate deforming in both directions.

Effect of Perforated Plate Thickness on the Target Plate Mid-point Deflection and Tearing Threshold

Increasing the perforated plate thickness had little effect on the target plate deflection with variations of less than one deflection-thickness ratio. The results showed an increase in the impulse at tearing of approximately 7.7% for a blockage ratio of 75%. The target plates with a blockage ratio of 89% reached an impulse of 34.4Ns without tearing, which was 19.4% higher than the impulse at tearing of 26.7Ns in the case where a deformable perforated plate was used.

Correlation between Computational and Experimental Results

The numerical modelling of the perforated plates using AUTODYN has proved to be successful showing good correlation between the computational and experimental impulse and deflection magnitudes.

The computational estimates of impulse were within -1.7% to 13.8% of the experimental values, with the majority of the computational values being larger than the corresponding experimental values. It was expected that the computational impulse values would be higher, as AUTODYN is an ideal model not taking into account factors such as the effective mass of explosive.

The target plate experimental mid-point deflections showed good correlation with the computational predictions with variations ranging from -0.53 and +0.74 plate thicknesses (1.6mm) with only one pair of data points (in the higher impulse region) falling outside this range, with a difference in mid-point deflection of -1.22 plate thicknesses. A comparison of the experimental and computational target plate profiles for a 9 gram charge mass showed good correlation for all blockage ratios, with variations in the deflection of less than one plate thickness.

The computational predictions for the perforated plate deflection were promising, with the accurate prediction of the deformation direction. Although AUTODYN did not predict buckling in the transition region, it did predict deflection in the direction of the blast wave within the experimental variation for each plate. The variation in the average deflection values was larger than that of the target plates. The computational results fell within -1.33 and +1.38 plate thicknesses. A comparison of the experimental and computational profiles of perforated plates for a 9 gram charge mass, showed variations in deflection of less than one plate thickness across the profile from the edge of the perforation to the boundary.

Effect of Blockage Ratio on the Plate Profile

The experimental target plate profile was compared with the shape function proposed by Duffey [41], for describing the final deformation profile of clamped circular plates loaded impulsively. Good correlation with variations in deflection of less than one plate thickness for all blockage ratios was obtained.

10. Recommendations

As a result of the findings and conclusions of this investigation, the following recommendations are made:

- Further testing across all blockage ratios using rigid perforated plates in order to obtain a better understanding of the relationship between the elimination of the plastic deformation mechanism and the impulse at tearing of the target plates.

- The effect of the separation distance between the plates should be investigated in order to ascertain possible influence of this distance on the three deflection regions of the deformable perforated plates.

- Further testing, with the possible application of pressure transducers on the plate surfaces, in order to determine the pressure distribution across both the perforated and target plate and hence the distribution of impulse. These results would also make for good comparison with the computational results.

- Further numerical modelling with emphasis on predicting tearing of the target plates.

- Further parametric studies and investigation into the effects of detonation mesh density on achieving the CJ pressure.

11. References

1. Washington Post, www.washingtonpost.com/wp-dyn/content/article/2006/04/28/AR2006042802181_pf.html (Last accessed 20 April 2008)
2. GN Nurick and JB Martin, Deformation of thin plates subjected to impulsive loading – a review, Part I: Theoretical considerations and experimental studies. Int J of Imp Eng, Vol. 8 (2), pp. 159 – 170, 1989.
3. GN Nurick and JB Martin, Deformation of thin plates subjected to impulsive loading – a review, Part II: Theoretical considerations and experimental studies. Int J of Imp Eng, Vol. 8 (2), pp. 170 – 186, 1989.
4. F Zhu and G Lu, A Review of blast and impact of metallic and sandwich structures, EJSE Special issue: Loading on structures, pp. 92-101, 2007.
5. WE Baker, Explosions in Air, University of Texas, Austin, 1973.
6. KF Kinney, Explosive shocks in air, The Macmillan Company, 1962.
7. JS Rinehart and P Pearson , Explosive working of metals, Pergamon Press, 1963.
8. PW Cooper and SR Kurowski, Introduction to the technology of explosives, Wiley – VCH, Inc, 1996.
9. The Steel Construct Inst, The effects of simplification of the explosion pressure-time history, British Gas Research and Technology, OTI-92599(BRI), 1992.
10. N Jacob, S Chung Kim Yuen, D Bonorchis, GN Nurick, SA Desai and D Tait, Quadrangular plates subjected to localized blast loads – an insight into scaling. Int J of Imp Eng, Vol. 30 (8 – 9), pp. 1179 – 1208, 2004.
11. S Chung Kim Yuen and GN Nurick, The significance of the thickness of a plate when subjected to localized blast loads. Proc of 16th Int Symp military aspects of blast and shock (MABS16) Oxford, UK, pp. 491 – 499, 2000.
12. GN Nurick and JB Martin, The measurement or the response of clamped circular plates to impulsive loading, 3rd Institute of physics conference on mechanical properties at high rates of strain, Oxford, Ser. No.70, pp. 495-501, 1984.

13. RG Teeling – Smith and GN Nurick, The deformation and tearing of circular plates subjected to impulsive loads, Int J of Imp Eng, Vol. 11 (1), pp. 77 – 91, 1991.
14. GN Nurick and GC Shave, Deformation and tearing of thin square plates subjected to impulsive loads, Int J of Imp Eng, Vol. 18 (1), pp. 99 – 116, 1996.
15. GS Langdon, GN Nurick and WJ Cantwell, The response of fibre metal laminate panels subjected to uniformly distributed blast loading, European J. of Mechanics A/Solids, Vol. 27, pp. 107 – 115, 2008.
16. N Jacob, The effect of stand-off distance on the failure of thin plates subjected to blast loads, MSc dissertation, University of Cape Town, 2005.
17. BM Thomas and GN Nurick, The effects of boundary conditions on thin plates subjected to impulsive loads, Plasticity 1995 – The 5th Int Symp on plasticity and its current application. Osaka, Japan, pp. 85 – 88, 1995.
18. SB Menkes and HJ Opat, Tearing and shear failures in explosively loaded clamped beams. Exp. Mech. 13, pp. 480 – 486, 1973.
19. TJ Cloete, GN Nurick and RN Palmer, The deformation and shear failure of peripherally clamped centrally supported blast loaded circular plates, Int J of Imp Eng, Vol. 32, pp. 32 92 – 177, 2005.
20. VH Balden, GS Langdon and N Jacob, Literature research report: Blast type landmine damping/suppressing methods and review report, CSIR/Defencetek, 2005.
21. H Kolsky, Stress waves in solids, Brown University, 2003.
22. JF Douglas, JM Gasiorek and JA Swaffield, Fluid mechanics, Fourth edition, 2001.
23. EJ Hearn, Mechanics of materials, University of Warwick, Third Edition, 1997.
24. DD Radford, GJ McShane, VS Deshpande and NA Fleck, The response of clamped sandwich plates with metallic foam cores to simulate blast loading, Int J Solids and Struc, Vol. 44, pp. 6101-6123, 2006.
25. Thunder in the valley air show,
    www.thunderinthevalleyairshow.com/mil_vehicles.htm
    (Last accessed 20 April 2008)

26. Force Protection, www.forceprotection.net/news/news_article.html?id=56 (Last accessed 20 April 2008)
27. SA Bushwar, www.geocities.com/sa_bushwar2/bufrond1.jpg (Last accessed 20 April 2008)
28. SP Medvedev, SV Khomik, and H Olivier, Experimental Set-up, Measurement technique and test condition for explosions with active/passive additives, EXPO Deliverable report D5 Contract EVG1-CT-2001-00042, March 2003.
29. A Britan, G Ben-Dor, O Igra, H Shapiro, Shock wave attenuation by granular filters, Int J of Multiphase Flow, pp. 617-634, 2001.
30. GS Langdon, GN Nurick, VH Balden and R Timmis, The use of perforated plates as passive mitigation systems, Defence Science J, India 2008 (in press).
31. RK Wharton, SA Formby and R Merrifield, Airblast TNT equivalence for a range of commercial blasting explosives, J of Hazard Mat, A79, pp. 31-39, 2000.
32. GR Cowper and PS Symonds, Strain-hardening and strain-rate effects in the impact loading of cantilever beams, Technical Report No.28, Office of Naval Research, NR-064-406, Division of Applied Mathematics, Brown University Providence, 1957.
33. ST Marais, RB Tait, TJ Cloete and GN Nurick, Material testing at high strain using the split hopkinson pressure bar, Latin AM J Solids Struct, Vol. 1, pp. 319-339, 2004.
34. JE Kennedy, Behaviour and utilisation of explosives in engineering design 12th Annual Symp, ASME UNM Albuquerque, NM; 1972.
35. Century Dynamics Inc. AUTODYN-2D and 3D v6.5 User Documentation, 2004.
36. EL Lee, HC Horning and JW Kury, Adiabatic expansion of high explosive detonation products, Technical Report UCRL – 50422, Lawrence Radiation Laboratory, University of California, 1968.
37. Z Liu, S Kubuto, S. Nagano and S. Itoh, High-speed photographic study on overdriven detonation of high explosive, 24th International Congress on High-Speed Photography and Photonics, Proc. SPIE Vol. 4183, pp. 731-738, 2001.
38. VH Balden, Private Communication (2007).

39. WC Young and RG Budynas, Roark's Formulas for stress and strain, Seventh Edition, 2007.
40. GN Nurick, An empirical solution for predicting maximum central deflections of impulsively loaded plates, Int Conf Mech Prop Materials at high strain rates, Oxford, 1989.
41. TA Duffey, The large deflection dynamic response of clamped circular plates subjected to explosive loading, Sandia Laboratories Research Report, SC-RR-67-532, 1967.

12. Bibliography

1. PS Bulson, Explosive loading of engineering structures, E & FN Spon, First Edition, 1997.
2. MA Meyers, Dynamic behaviour of materials, John Wiley & Sons Inc, 1994.
3. PW Cooper, Explosives engineering, Wiley-VCH,1996.
4. KA Marchand and F Alfawakhiri, Blast and progressive collapse – facts for steel buildings, No. 2, American Institute of steel construction, Inc, 2004
5. VH Balden and GN Nurick, Numerical simulation of the post-failure motion of steel plates subjected to blast loading, Int J of Imp Eng, Vol. 32, pp.14 – 34, 2005.
6. MD Theobald and GN Nurick, Numerical investigation of the response of sandwich-type panels using thin walled tubes subjected to blast loading, Int J of Imp Eng, Vol. 34, pp. 134 – 156, 2007.

Appendix A – Results of Uni-axial Tensile Tests

The material properties of the mild steel test plates where obtained from uni-axial tensile tests performed on the tensile testing unit in the materials laboratory at the University of Cape Town. The British Standard BS18: 1987 Methods for Tensile Testing of Metals was used for the sizing of the mild steel tensile test specimens shown in Figure 103.

Figure 103: Photograph of a typical tensile test specimen

The specimen geometry is listed in Table 30.

Nominal Width	12.5	mm
Total Length	200	mm
Gauge Length	78.3	mm
Fillet Radius	25	mm

Table 30: Tensile test specimen geometry

The force and displacement values obtained from the test machine were converted to engineering stress and strain. The data was plotted on an engineering stress versus engineering strain curve from which the dynamic yield stresses were obtained. The static yield stresses were then calculated using the Cowper-Symonds [32] equation. A typical engineering stress-strain curve is shown in Figure 104. The test plates were cut from several sheets of mild steel labelled A to F, the properties of which are listed in Table 31. Each test plate was labelled according to the sheet from which it was cut.

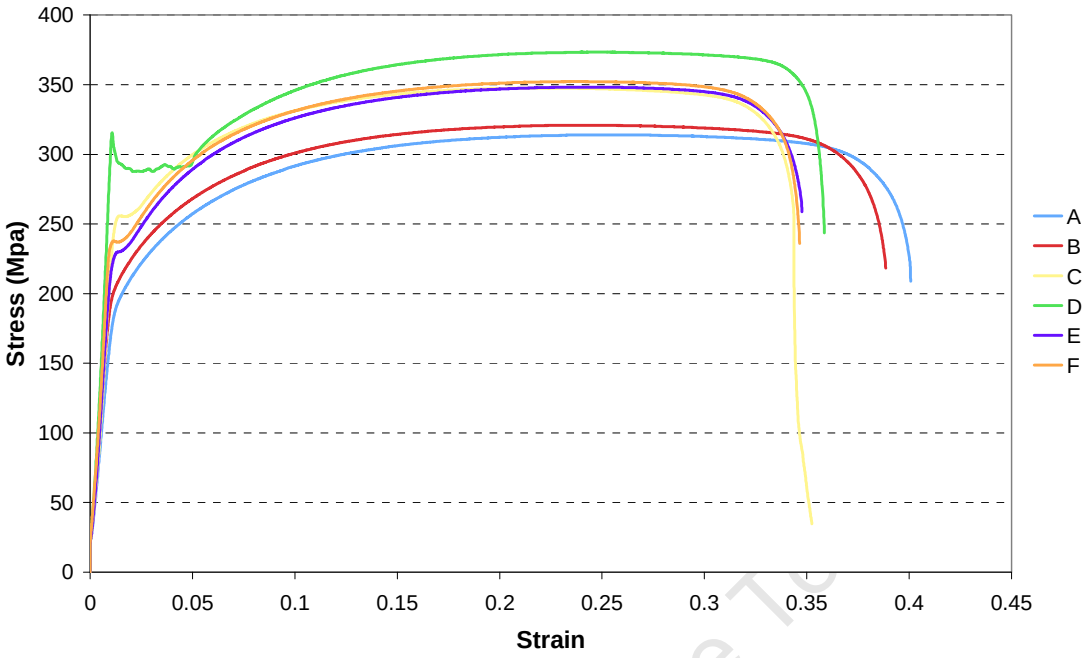

Figure 104: Graph of typical engineering stress-strain curves for mild steel sheets A to F

Sheet	Density kg/m^3	Static Yield Stress
A	7921	179
B	7903	192
C	7869	251
D	8102	311
E	7686	234
F	7808	237

Table 31: Mild steel material properties

The power law hardening equation was used in the AUTODYN simulations to model the stress in the deforming material; the values of A, B and n were obtained from a best fit between the true stress-strain curve and the power law hardening equation shown in Figure 105 . The true stress-strain curve is used as it gives a more accurate indication of deformation characteristics of metal in the plastic region taking into account the reduction in cross-sectional area and necking.

The following equations were used to calculate the true stress and strain values from the engineering stress and strain values:

$$\sigma_T = \sigma_E \cdot (\varepsilon_E + 1) \tag{A1}$$

$$\varepsilon_T = \ln(\varepsilon_E + 1) \tag{A2}$$

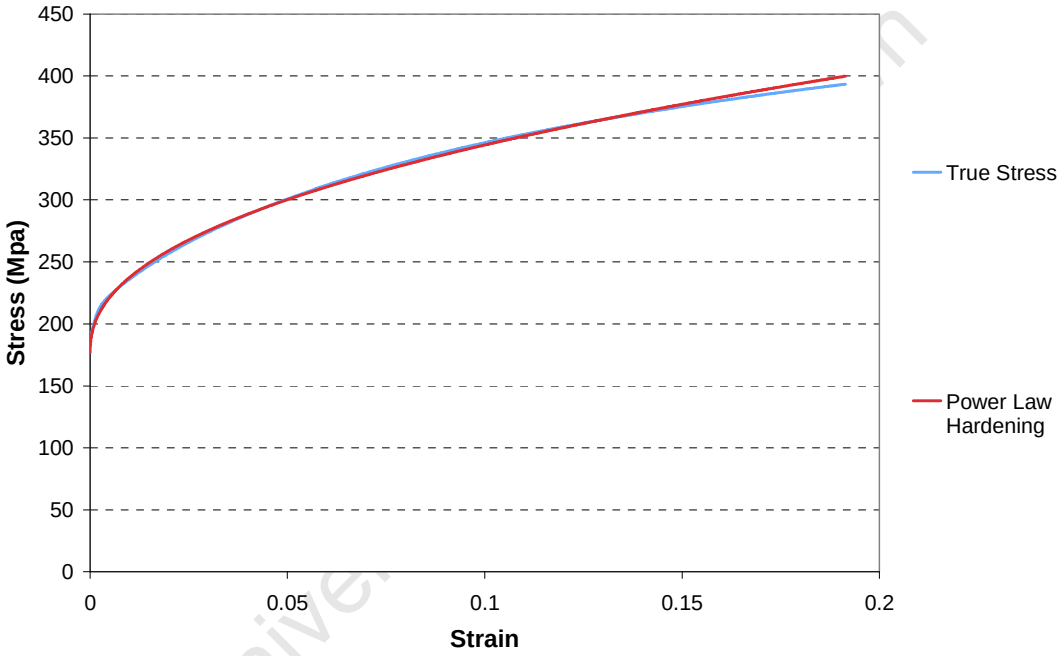

Figure 105: Graph of best fit between the true stress-strain and power law hardening curves for sheet A

The values of A, B and n for each mild steel sheet are listed in Table 32.

Sheet	A	B	n
A	176.8	462.5	0.464
B	178.4	467.5	0.472
C	199.1	450.1	0.408
D	228.0	496.2	0.446
E	181.4	491.6	0.409
F	181.9	495.1	0.415

Table 32: Power law hardening constants for mild steel sheets A to F

Appendix B – Ballistic Pendulum

The ballistic pendulum geometry is shown in Figure 106. The linearised equation of motion of the ballistic pendulum, assuming viscous damping is

$$\ddot{X} + 2\beta\dot{X} + \omega_n^2 X = 0 \tag{B1}$$

Where $\beta = \frac{C}{2M}$ and $\omega_n = \frac{2\pi}{T}$.

C is the damping coefficient, M is the total mass of the pendulum including the test rig, I-beam and balancing mass, T is the natural period of the pendulum.

The solution of equation B1 is given by

$$X = \frac{e^{-\beta t}\dot{x}_0 \sin(\omega_d t)}{\omega_d} \tag{B2}$$

Where $\omega_d = \sqrt{\omega_n^2 \beta^2}$ and $\dot{x}_0$ is the initial velocity of the pendulum.

Let x_1 be the horizontal displacement at $t = \frac{T}{4}$ and x_2 be the horizontal displacement at $t = \frac{3T}{4}$. Substituting into equation B2 gives

$$x_1 = \frac{\dot{x}_0 T}{2\pi} e^{-0.25\beta t} \tag{B3}$$

$$x_2 = \frac{\dot{x}_0 T}{2\pi} e^{-0.75\beta t} \tag{B4}$$

Hence

$$\frac{x_1}{x_2} = e^{0.5\beta t} \tag{B5}$$

Giving

$$\beta = \frac{2}{T}\ln\left(\frac{x_1}{x_2}\right) \tag{B6}$$

And

$$\dot{x}_o = \frac{2\pi}{T} x_1 e^{0.25\beta t} \tag{B7}$$

The impulse can then be calculated from

$$I = M\dot{x}_o \tag{B8}$$

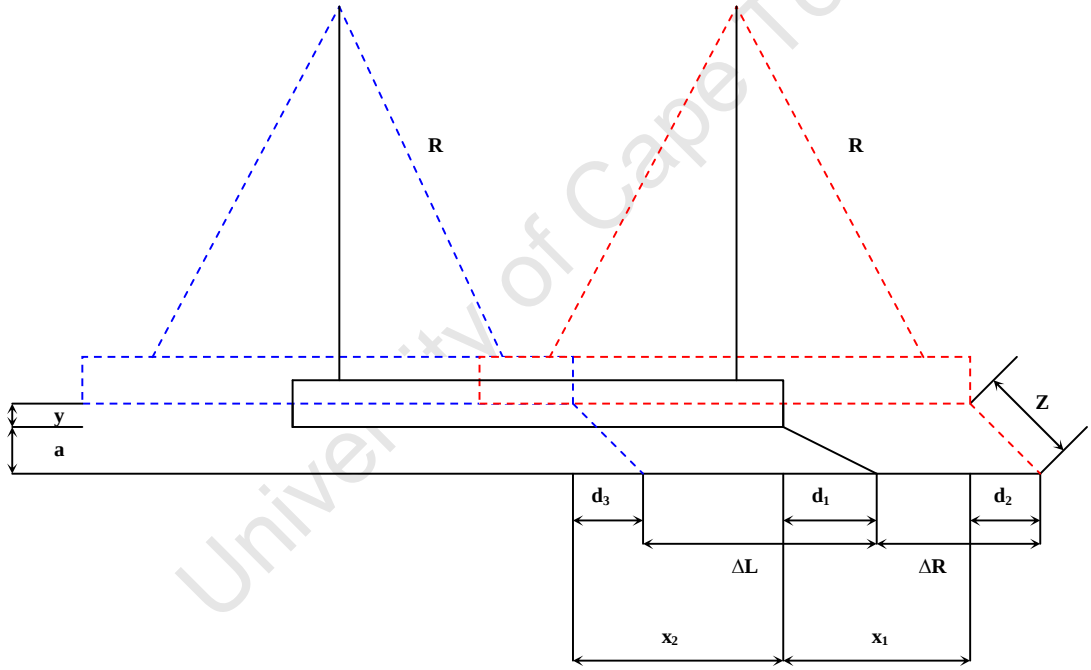

Figure 106: Ballistic pendulum geometry

The value of T is calculated by averaging any number of pendulum oscillations. During testing the values of ΔL and ΔR are recorded for each and every test as well as the values for a, Z and R. The ballistic pendulum data is given in Table 33.

The horizontal distance from the end of the I-beam to the tip of the pen when the pendulum is stationery is given by

$$d_1 = \sqrt{Z^2 - a^2)} \tag{B9}$$

At the maximum amplitude of the oscillation the horizontal distance between the end of the I-beam and the pen decreases, this distance is d_2 and is calculated by

$$d_2 = \sqrt{Z^2 - (a+y)^2} \tag{B10}$$

For small angles

$x_1 = R\theta$ and $y = \frac{R\theta^2}{2}$

Therefore

$$y = \frac{x_1^{\,2}}{2R} \tag{B11}$$

Substituting equation B11 into equation B10 gives

$$d_2 = \left[Z^2 - \left(a + \left(\frac{x_1^{\,2}}{2R} \right) \right)^2 \right]^{1/2} \tag{B12}$$

From Figure 106

$$x_1 = \Delta R + d_1 - d_2 \tag{B13}$$

and

$$x_2 = \Delta L - d_1 + d_2 \tag{B14}$$

Substituting equations B9 and C12 into equations B13 and B14 the values for (x_1) and (x_2) can be calculated by

$$x_1 = \Delta R + (Z^2 - a^2)^{1/2} - \left[Z^2 - \left(a + \left(\frac{x_1^2}{2R} \right) \right)^2 \right]^{1/2} \tag{B15}$$

$$x_2 = \Delta R - (Z^2 - a^2)^{1/2} + \left[Z^2 - \left(a + \left(\frac{x_1^2}{2R} \right) \right)^2 \right]^{1/2} \tag{B16}$$

Time Period (s)	3.4		
R (m)	2.96 – 2.99		
Z (m)	0.2		
A (m)	0.149 – 0.158		
	I Beam	Test Rig (without plates)	Counter Balance
Pendulum Mass (kg)	25.2	57.5	67.0

Table 33: Ballistic pendulum data

Appendix C – Test Plate Deflection Profiles

C.1 Experimental and Computational Test Plate Profiles

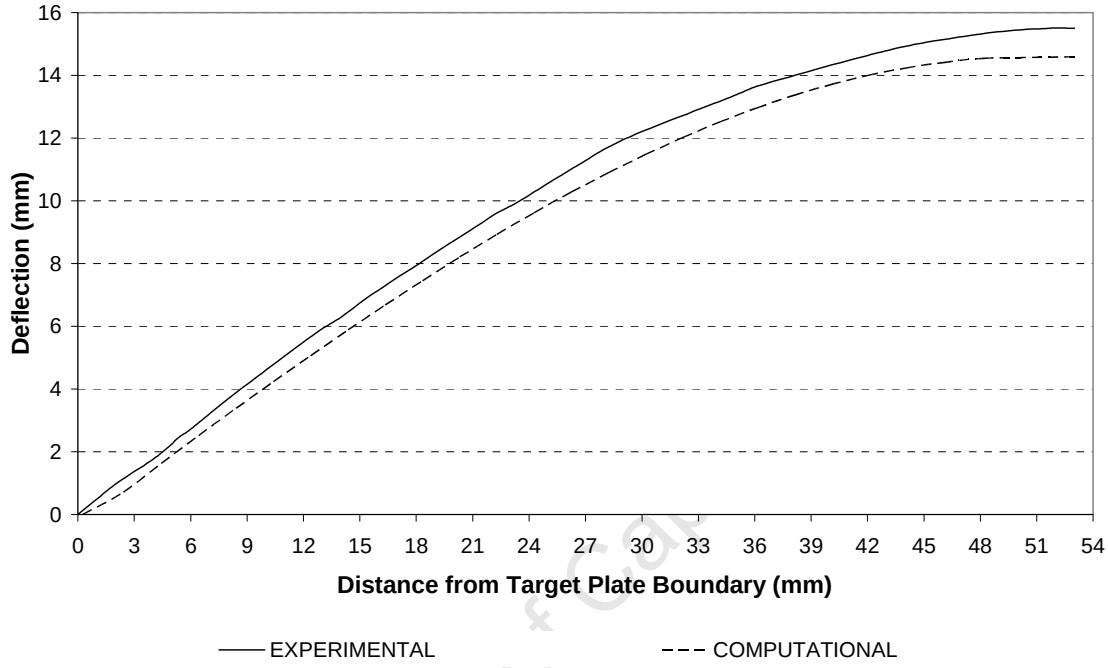

Figure 107: Graph of the experimental and computational target plate profiles for a 9 gram charge mass and a blockage ratio of 25%

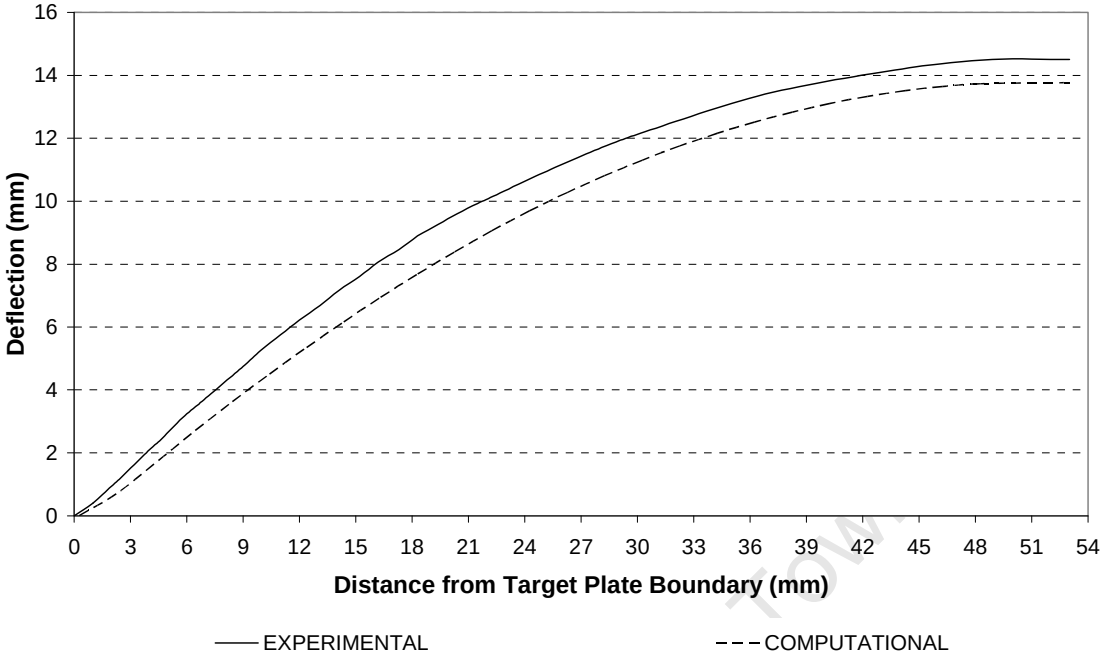

Figure 108: Graph of the experimental and computational target plate profiles for a 9 gram charge mass and a blockage ratio of 65%

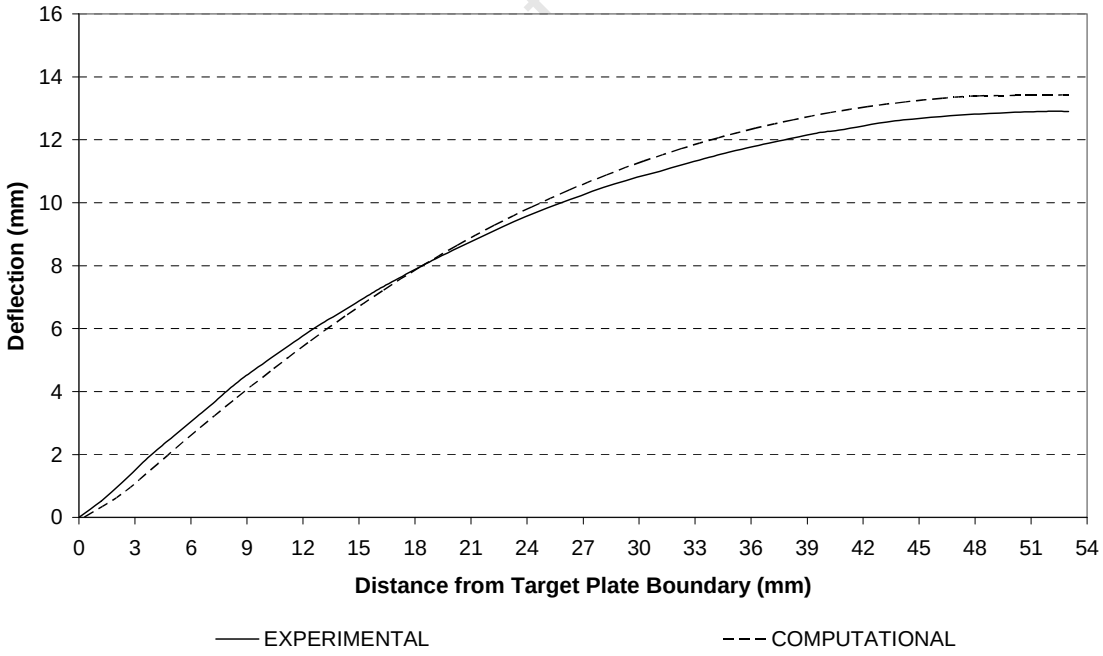

Figure 109: Graph of the experimental and computational target plate profiles for a 9 gram charge mass and a blockage ratio of 75%

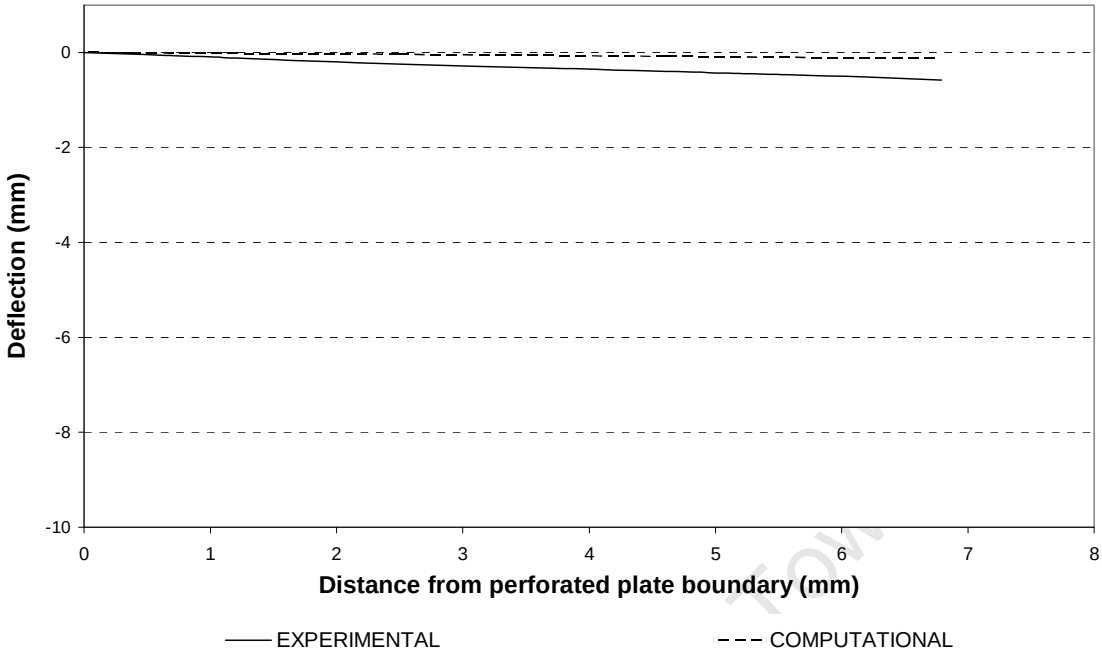

Figure 110: Graph of the experimental and computational perforated plate profiles for a 9 gram charge mass and a blockage ratio of 25%

C2. Experimental Target Plate Profiles and Duffey Shape Functions

Figure 111: Graph of the experimental target plate profile and Duffey [41] shape function for a 9 gram charge mass and a blockage ratio of 25%

Figure 112: Graph of the experimental target plate profile and Duffey [41] shape function for a 9 gram charge mass and a blockage ratio of 65%

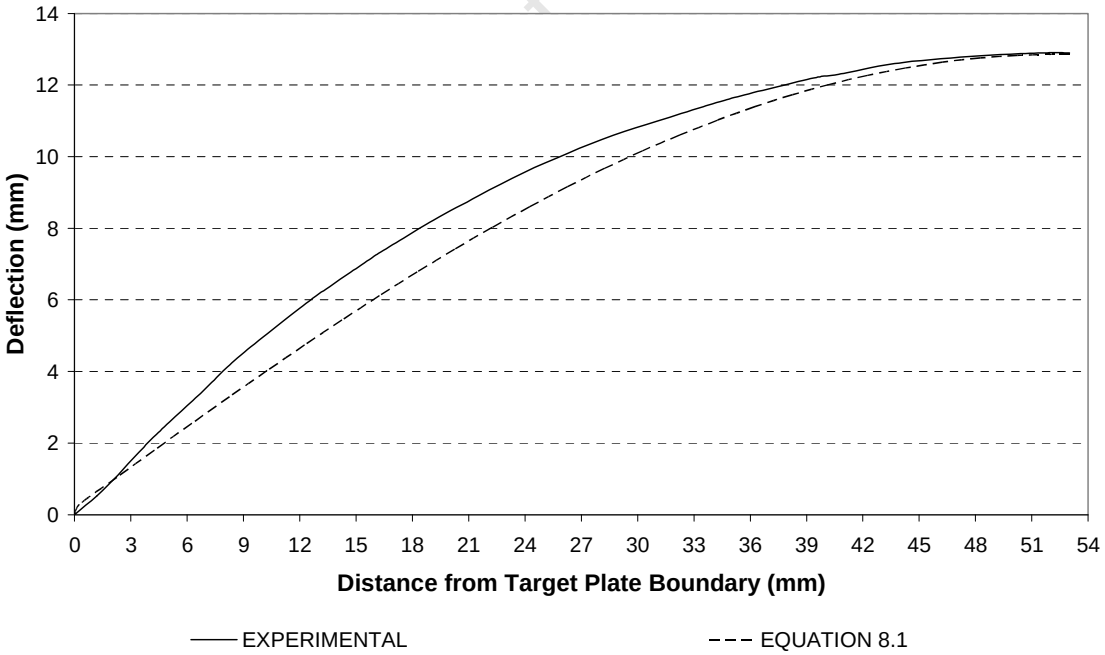

Figure 113: Graph of the experimental target plate profile and Duffey [41] shape function for a 9 gram charge mass and a blockage ratio of 75%

Appendix D – Drawings

D.1 Target Plate

D.2 Deformable Perforated Plate

D.3 Rigid Perforated Plate